DEVELOPMENT OF A BIOMIMETIC DOUBLE NETWORK HYDROGEL WITH A DUAL MECHANISM FOR INCREASED TOUGHNESS AND SUSTAINED TOBRAMYCIN ELUTION INSPIRED BY THE UNDERWATER CADDISFLY SILK

by

Dwight Douglas Lane

A dissertation submitted to the faculty of
The University of Utah
in partial fulfillment of the requirements for the degree of

Doctor of Philosophy

Department of Bioengineering

The University of Utah

December 2017

T h e U n i v e r s i t y o f U t a h G r a d u a t e S c h o o l

STATEMENT OF DISSERTATION APPROVAL

The dissertation of **Dwight Douglas Lane**

has been approved by the following supervisory committee members:

Russell J Stewart	, Chair	**6/16/2017** Date Approved
Jindrich Kopecek	, Member	**4/26/2017** Date Approved
Theodore G. Liou	, Member	**4/26/2017** Date Approved
Dustin Lee Williams	, Member	**4/26/2017** Date Approved
Vladimir Hlady	, Member	**6/16/2017** Date Approved

and by **David W. Grainger** , Chair/Dean of

the Department/College/School of **Bioengineering**

and by David B. Kieda, Dean of The Graduate School.

ABSTRACT

Phosphate-metal complex formation is a naturally occurring toughening mechanism in underwater materials and has been incorporated into the synthetic hydrogel material discussed in this dissertation. Polyphosphate hydrogels were loaded with Ca^{2+} which crosslinks OPO3 groups in the hydrogel which increase the initial modulus from 0.04 to 10.3 MPa and rupture at a critical force to dissipate strain energy and act as a sacrificial network to preserve the integrity of the hydrogel. Phosphate metal crosslinks are electrostatic domains that are easily recoverable, which adds to the durability and usefulness of the hydrogels. This toughening mechanism was borrowed from the underwater caddisfly larvae, which spin a tough, adhesive silk fiber to manufacture protective mobile cases from sticks, rocks and other advantageously gathered materials. The caddisfly silk also uses serial domains of phosphates crosslinked with Ca^{2+} to increase modulus and produce strain induced yield, energy dissipation, and recoverability.

In addition to metal ions, positively charged aminoglycoside antibiotics such as tobramycin can also be used as crosslinking agents. Due to electrostatically delayed diffusion, tobramycin is gradually released and exchanged with metal ions in biologically relevant Ca^{2+} and Mg^{2+} containing solutions. In the polyphosphate hydrogel system, tobramycin was included with and without the presence of Ca^{2+} to form a hydrogel with the capability to sustain tobramycin release for up to 70 days and totally eradicate pseudomonas aeruginosa biofilms within 48 *h*. In the case of hydrogels loaded with Ca^{2+} and tobramycin, the hydrogels retained their toughness, and durability and thus may be used as structural materials in total joint

replacement to reduce incidence of infection.

Complex coacervation is an alternative to the polyphosphate-tobramycin hydrogel system and occurs as a phase separation where a dense coacervate of polyphosphate and tobramycin is formed. The formation of clear, fluid coacervate phase is dependent on salt concentration and is maximized at ~1M NaCl. Polyphosphate-tobramycin coacervates have a sustained release assay for up to 60 days. Additionally, the coacervate can be resuspended into micro droplets by vortex and subsequently aerosolized for pulmonary delivery of tobramycin. Aerosolized coacervate is ideal for treating chronic pulmonary infection in cystic fibrosis. It could not only improve rates of pseudomonas aeruginosa infection but also reduce the number of required doses and thus improve patient compliance.

TABLE OF CONTENTS

SYMBOLS

PCR	polymerase chain reaction
Glu	Glutamate
Asp	Aspartate
Arg	Arginine
Lys	Lysine
Ser	Serine
Val	Valine
Leu	Leucine
Ile	Isoleucine
pS	Phosphoserine
GA	Glycine Alanine
Pro	Proline
Gly	Glycine
Pa	Pascal (unit)
M	Mega
k	kilo
pH	Potential hydrogen
EDTA	Ethylenediaminetetraacetic Acid
J	Joule
m	meter
pHEMA	poly(2-hydroxyethyl methacrylate)
PVA	poly(vinyl alcohol)
PEG	poly(ethylene glycol)
pAAm	polyacrylamide
pNIPAAm	poly(N-isopropylacrlyamide) DN Double network
PAMPS	poly(2- acrylamido-2-methylpropanesulfonic acid)
PDGI	poly(dodecyl glyceryl itaconate)
PAN	Polyacrylonitrile
PMPC	poly(2-methacryloyloxyethyl phosphorylcholine)
NaSS	sodium p-styrenesulphonate
MPTC	3-(methacryloylamino)propyl-trimethylammonium chloride
P.aeruginosa	Pseudomonas aeruginosa
CDC	Center for disease control
MRSA	Methicillin resistant staphylococcus aureus
DNA	Deoxyribonucleic acid
CF	Cystic fibrosis
CFTR	Cystic fibrosis transmembrane conductance regulator
RNA	Ribonucleic acid

RPA	Random phase approximation
IPN	Interpenetrating network
SEM	Scanning electron microscopy
g	gram
mL	milliliter
Mm	Molecular mass
Mw	Molecular weight
MOEP	2-(Methacryloyloxy)ethyl phosphate
TEA	Triethylamine
DI	Deionized
THF	Tetrahydrofuran
NMR	Nuclear magnetic resonance
AIBN	Azo-bis- isobutyronitrile
MA	Methacrylate
MAA	Methacrylic Acid
PDI	Polydispersity index
SEC	Size exclusion chromatography
TEMED	tetramethylethylenediamine
Tris	tris(hydroxymethyl)aminomethane
ICP-OES	Inductively coupled plasma optical emission spectroscopy
ATR-FTIR	Attenuated total reflection – fourier transform infrared spectroscopy
HSAB	Hard soft acid base
MBC	Minimum bactericidal concentration
MIC	Minimum inhibitory concentration
pPEMA-pAAm	Poly(phosphoethyl-methacrylate) co-poly(acrylamide)
BHI	Brain heart infusion
CAMHB	Cation adjusted meuller-hinton broth
m	minute
h	hour
PRM	Pyrogallol red molybdate
CFU	Colony forming unit
CLSI	Clinical and laboratory standards institute
ZOI	Zone of inhibition
ANOVA	Analysis of variance
HEPES	4-(2-hydroxyethyl)-1-piperazineethanesulfonic acid
ROS	Reactive oxygen species

ACKNOWLEDGEMENTS

I want to first acknowledge the important role of my advisor, Dr. Russell Stewart, for bringing me into his lab and assigning me the privilege of working on the caddisfly project. I have enjoyed exploration of real-world applications for the investigations that Dr. Stewart and Dr. Nicholas Ashton performed with natural caddisfly silk. Dr. Stewart's skill in communicating the impact of our work to various funding agencies made the important work in our lab possible. I want to thank my supervisory committee, Dr. Vladimir Hlady, Dr. Dustin Williams, Dr. Jindrich Kopecek, and Dr. Ted Liou M.D. for their valuable advice and rigorous review of my work which has led to my improvement and growth as a scientist and engineer. I want to especially thank Dr. Vladimir Hlady for providing great mentorship and training for my first two years of my graduate studies. It is in part due to his efforts to bring me into his lab and help me secure funding that brought me and my family to the University of Utah.

I am grateful for collaborations I have been honored to work with. First, I want to express gratitude to the Bone Joint Research Lab and Dr. Dustin Williams for providing an environment where I could pursue efforts to eradicate chronic biofilm-based infection. Second, I thank the Adult Cycstic Fibrosis Center and Dr. Ted Liou for their enthusiasm to aid me in exploring applications for our technology that could potentially bless the lives of thousands of cystic fibrosis patients and their families across the world.

My fellow lab mates have been a vital support system to me. They have helped emotionally when the stresses of graduate student life and failed experiments act to discourage

and were important resources for scientific advice. I want to give thanks to Dr. Nicholas Ashton who spent countless hours discussing caddisfly silk and caddisfly mimetic materials. I also would like to thank previous lab members from the Hlady research group including Dr. Kathleen Job, Dr. Tony Hsiao, Dr. Vimal Swarup, and Dr. Colin Eichinger who were my first exposure to graduate work and did a phenomenal job of introducing me to the doctorate program. Additionally, I want to thank the rest of the Stewart Research group including: Monika Sima for her efforts in managing the lab and keeping everyone on task, Dr. Mahika Weerasekare and Dr. Sarbjit Kaur for instructing me in polymer and monomer synthesis, Dr. Ching-Sheuen Wang as well as Josh Jones and Leland Prather for being valuable lab mates.

Support from grants from the Army Research Office and National Institutes of Health have made this work possible. I want to acknowledge their generous support.

My family deserves special thanks; I had good parents who encouraged my interest in science from an early age. They provided important support early in my pursuit of higher education. I need to thank my children Drexel, Dyson, Conrad, and Christianna for their role as a constant source of inspiration and motivation to be successful and strive to make the world a better place. Finally and most importantly, I want to express my thanks for the support of my wife, Cherise, for her sacrifice and willingness to follow me to Utah and put up with countless, lonely nights and weekends as I toiled in the lab. I am grateful for her efforts as a mother to my children and a cheerleader when I was discouraged. I have relied constantly on her strength throughout my education.

CHAPTER 1

INTRODUCTION

1.1 Biomimetic materials: reverse engineering nature

Nature has excelled for millions of years at solving difficult problems using relatively few constituent materials, primarily comprising proteins and minerals.[1] Central to many of these solutions is the complex, hierarchical structuring of natural materials.[2] For example, the hierarchical arrangement of Nephila clavipes orb weaving spider silk, including a central core of parallel fibers encased in an outer skin layer, has been accredited with the silks remarkable strength.[3] These biological structures have often provided inspiration for engineering challenges in the areas of architecture,[4] aerodynamics,[5] mechanical engineering[5] and materials science.[6] Of particular interest is the innate ability for natural tissues to self-repair. This occurs not only on a molecular level with the inclusion of sacrificial reforming bonds, as observed in wood[7] and bone where bonds are broken and reformed, but also at a cellular level where cells such as osteoblasts or fibroblasts lay down new tissue during repair processes.[1]

Nature has adapted a simple arsenal of building materials into intricate solutions for complex problems. An underlying theme of the work presented here suggests that equally intricate answers to today's problems can originate from mimicking simple structural components or design themes found in nature.

1.2 Aquatic caddisfly silk

1.2.1 Caddisfly larva: the underwater architect

The inspiration, behind the works presented, is nature's underwater architect, the caddisfly.[8] Caddisflies, order trichoptera, inhabit numerous fresh water habitats and mountain rivers and streams worldwide. Caddisfly lay their eggs underwater where new larvae live most of their yearly lives before pupation and brief mating and egg laying, Figure 1.1. The caddisfly larvae draw silk fibers from glands filled with fluid precursors, similar to related moth and butterfly larvae. The caddisfly silk is an adhesive fiber, used to assemble mobile protective cases and weave webs to gather food, Figure 1.1. This inventive use of silk has given rise to the widespread success of the species which is the second most abundant aquatic insect comprising approximately 14,291 different species. Details concerning the molecular makeup of caddisfly silk and its connection to mechanics and function has only recently been brought to light, in great part due to the efforts of Nicholas Ashton and Russell Stewart et.al.[9–14]

1.2.2 Caddisfly silk: structure and function

Caddisfly silk is a sticky, pressure sensitive tape comprised of a viscoelastic core encased in an adhesive outer coating. Silk attributes are uniquely derived from either the fibrous core or the adhesive outer layer, Figure 1.2. The fiber core imparts mechanical strength from multiple sub-fibers which are axially aligned, similar to other natural silks from moths, butterflies or spiders. The adhesive component is vital to full functionality as a binding substance for caddisfly cases. Inspiration for a biomimetic material was mechanically based, and thus, obtained solely from the structural core portion of the silk and not the outer adhesive layers.

The primary component of the silk core as determined through quantitative PCR is the protein H-fibroin, Figure 1.3.[14] H-Fibroin is highly repetitive and has up to 35 mol% of the amino

acid residues charged including Glu, Asp, Arg, and Lys. Additionally, approximately 15.5 mol % of Ser are negatively charged via post-translational phosphorylation.[15] In fact, the phosphorylation of Ser residues has been identified across a wide range of suborders and appears to be conserved across the species. Of particular importance is the conservation and repetitive nature of a specific residue sequence termed the (pSX)n domain where n is 4-6, X is typically aliphatic Val, Leu or Ile and pS is phosphorylated Ser.[9] Comparable repetitive sequences, like the poly(GA) domains found in terrestrial moths or spider silks, have been directly linked to a structural role in forming antiparallel β-sheets.[16] The (pSX)n domain in caddisfly silk has likewise been attributed formation of antiparallel β sheets.[17,18] Stewart and Wang revealed the central role of Ca^{2+} crossbridging between dianioic-pSs in stabilizing an antiparallel structure in caddisfly silk. A model was proposed where 2 $(pSx)_n$ domains flanking a central Pro-Gly sequence leads to the peptide backbone folding back on itself with aliphatic residues stabilized due to hydrophobic effects and pS by Ca^{2+} crosslinking, Figure 1.4.[9] The presence of these parallel beta sheet structures throughout the silk fibers has been shown to play a vital mechanical role in preserving the integrity and durability of caddisfly silk.

Caddisfly silk exhibits various mechanical properties that are of interest for biomaterials. Principally, the silk displays striking toughness for a highly hydrated material, ~66% water by weight. Caddisfly silk has an initial modulus of 86.5 +/- 19.2 MPa and work of extension to failure of 17.3 +/- 6.2 MJ m^{-3}.[19] Additionally, the silk displays a pseudo yield point, large strain hysteresis and energy dissipation. Following strain, the silk self recovers 100% of the mechanics within 120 m. Stewart and Ashton et. al. presented a convincing case that directly links the Ca^{2+} and phosphate crosslinked (pSX)n domains with silk modulus, pseudo yielding behavior and spontaneous self-recovery following strain.[9,10,12] Through the use of a custom

novel micro- materials testing system, single silk fibers were strained in tension allowing for the connecting of caddisfly silk micro-structure with mechanics. By removing Ca^{2+} with EDTA the native silk showed a reduction of initial modulus and complete loss of yielding behavior, Figure 1.5. By the same token, the initial modulus and stress required for yield could be modulated by exchanging Ca^{2+} with other di or tri-valent metal ions.[9] A trend emerged linking increased modulus, yield stress, and peak stress with increasing electronegativity.[12] The yielding behavior and self-recovery was attributed to the reversible nature of the metal-phosphate bonds and a viscous unravelling of the $(pSX)_n$ domains that would reform as guided by an elastic recoiling force.

In nature, the caddisfly silk works to dissipate impact energy to maintain the structural integrity of the case while the complete recovery leads to long term durability. These mechanical properties are desirable for translation into hydrated but tough prosthetic biomaterials and served as an inspiration for the development of caddisfly mimetichydrogel.

1.3 Double network hydrogels

1.3.1 Evolution of hydrogels: from single to double networks

Hydrogels are three dimensional polymer networks capable of retaining large quantities of water. The field of modern hydrogels began in the 1960s with the publications of Wichterle and Lim on a poly(2-hydroxyethyl methacrylate) hydrogel and subsequent hydrogel based contact lenses.[20] These early hydrogels were synthesized from primarily hydrophilic monomers or polymers in the presence of multifunctional crosslinkers. The most commonly used hydrogels were poly(2-hydroxyethyl methacrylate) (pHEMA), poly(vinyl alcohol) (PVA), poly(ethylene glycol (PEG), and poly(acrylamide) (pAAm).[21] Hydrogels are generally considered to be biocompatible due to the high water content and similarities to natural tissues, a motivating

factor in the exponential growth of the field over the last few decades.[22]

Following the early pioneering work into simple, water swollen hydrogel networks, there was a shift in the 1970s toward more complicated, environmentally responsive hydrogels. These smart hydrogels undergo swelling changes facilitated by external stimuli including pH, temperature, ionic strength, solvent type, electric or magnetic fields, light, pressure, and presence of chelating agents.[23,24] A popular, widely studied responsive system has been the in situ forming systems of poly(N-isopropylacrlyamide) (pNIPAAm) which rely on hydrophobic interactions to set the gel with increased temperature.[21] Hybrid hydrogels consisting of synthetic materials and biological macromolecules or synthetic peptides have exploited the biocompatibility of the traditional hydrogel network and functionality from the bio-macromolecules for an overall synergistic effect.[24] For example, Gallot et. al. prepared di-block copolymers of polystyrene and poly(benzyloxycarbonyl-L-lysine) or poly(benzyl-L-glutamate) peptides which induced formation of lamellar structures which was subsequently linked to peptide secondary structures.[25] Environmentally responsive hydrogels have been applied to a variety of applications including tissue engineering, biosensors and microfluidics.[24] However, in many instances the weak mechanical nature of hydrogels has limited their use to drug delivery.

The current arsenal of hydrogel materials are collectively weak and brittle, which has led to attempts to strengthen hydrogel materials for use as implantable prosthetic biomaterials. In contrast, natural tissues such as tendons, ligaments, muscle, and cartilage are highly hydrated (30- 80% water), soft materials but are also tough and capable of load bearing or shock absorption.[26] The lack of strength in traditional hydrogels may be a result of the low density of polymer chains, limited friction between the chains and the inhomogeneous structure which concentrates stress around defects and promotes facture propagation.[26] Some efforts to make the hydrogel structure more homogeneous have included a tetra-PEG hydrogel made from

tetrahedron type monomers, which use a slide-ring structure with mobile crosslinking points.[27,28] Composite hydrogels of NIPAM and inorganic clay have also been shown to have improved toughness over single network systems.[29] An alternative and increasingly widespread approach for toughened hydrogels involves incorporation of multiple network structures, termed double network (DN) hydrogels.

Early DN hydrogels as reported by J.P. Gong et.al. were a tightly crosslinked rigid poly(2-acrylamido-2-methylpropanesulfonic acid) (PAMPS) network interpenetrating within a second loosely crosslinked pAAm network.[30] These hydrogels exhibited both a high modulus from the rigid network with the extensibility of the loosely crosslinked network. This combination of increased modulus (0.1 – 1 MPa) and extensibility (1000-2000%) resulted in significantly higher tearing fracture energy (100-1000 J m^{-2}), or toughness. During cyclical strain, energy is dissipated through chemical breakdown of polymer chains in the rigid or sacrificial network leading to accumulation of damage and a loss of toughness over time.[19] To counteract fatigue related failure in early DN hydrogels, a multitude of creative approaches replaced the covalent linkages in one network with reversible non covalent bonds. Jie Zheng et. al. polymerized Agar and pAAm to create a DN hydrogel with a covalently linked pAAm network and sacrificial agar network with physically entangled helix bundles.[31] Haque and Gong et. al. used a PDGI/pAAm hydrogel with stacked lipid-like bilayers as a sacrificial domain with excellent self-recovery.[32] Bai and Lu et. al. produced a similar effect in a PAN/PMPC hydrogel with CN dipole moieties which interact to form the sacrificial network.[33] Sun and Gong et. al. crosslinked cationic sodium p-styrenesulphonate (NaSS) and anionic 3-(methacryloylamino)propyl-trimethylammonium chloride (MPTC) monomers to form a hydrogel with both covalent linkages and ionic crosslinks of varying strength, leading to recoverable yield.[34] Other hydrogels have used charged moieties crosslinked with positively charged metal ions leading to increased modulus, toughness and

recoverability. Sue et. al. crosslinked carboxyl groups with divalent Ca^{2+} while Shull et. al. investigated a wider variety of divalent metals including Ca^{2+}, Zn^{2+}, Ni^{2+}, Co^{2+}, and Cu^{2+}.[35,36] Shull et. al. concluded that different metal ions resulted in bonds of varying strength with the transition metal ions creating stronger ionic bonds than Ca^{2+}, which was postulated to interact electrostatically.[36] While a more complex bonding method related to d-orbital configuration was expected for certain transition metals the authors stopped short of a discussion into coordination bonding, which will be discussed in Chapter 2.[36]

1.3.2 Intersection of caddisfly silk and double network hydrogel design

While there have been great strides in increasing the strength and durability of hydrogels by incorporating a reversible sacrificial domain into DN hydrogels the modulus, toughness and recoverability falls short of the mechanics of the natural underwater caddisfly silk, Table 1.1. It is noteworthy to state that while some of the DN hydrogels in Table 1.1 have impressive strength, this toughness is only academic and occurs as a result of 100s to 1000s of percent extension at failure, an event not experienced *in vivo*. The motivation behind Chapter 2 was to reproduce the mechanics observed in caddisfly silk, within a synthetic caddisfly mimetic hydrogel by the simple inclusion of phosphate side chains within a pAAm network.[19]

1.4 Impact of biofilms and infection

1.4.1 Expanding the functionality of caddisfly inspired hydrogels

Modern biofilm theory can be traced to the work of J.W. Costerton beginning in 1978.[37] His basic theory was a culmination of observations and works suggesting that bacteria will preferentially adhere to surfaces forming complex colonies. By 1982, this phenomena was shown to be true for medical device surfaces, as illustrated in a case study by T. Marrie M.D. and J.W.

Costerton involving a pace maker contaminated with Staphylococcus aureus biofilm.[38] Two years later, A Gristina M.D. and J.W. Costerton reported a similar incidence in several orthopedic implants.[39] In an effort to expand the function of a caddisfly inspired DN hydrogel, Chapter 3 will present the results of loading poly-cationic tobramycin antibiotic into a polyphosphate hydrogel. Antibiotic-loaded DN hydrogels have the potential to prevent initial infection as a component of implantable or invasive medical devices or as a prophylactic to combat difficult infections such as those involving biofilms.

1.4.2 Characterization of biofilms and antibiotic resistance

The biofilm is an exopolysaccharide matrix secreted by adhered cells which increases antibiotic resistance by up to 1000 fold.[40–42] Early observations by Lawerence et. al. used scanning confocal laser microscopy to reveal complex biofilm structure including large plumes and channels, hypothesized to transport nutrients throughout the biofilm and improve survivability.[43] These features can be clearly identified in SEM images of *P.aeruginosa* biofilms in Figure 1.6.

Some resistance may stem from frustrated penetration of antibiotic into the biofilm, in the case of positively charged aminoglycosides absorption to negatively charged biofilm components will reduce effectiveness.[44,45] Slowed diffusion of aminoglycosides would seem to be a short-term problem as eventually all binding sites would be occupied and lead to a restoration of diffusion, although some authors have argued that slowed diffusion may accentuate an enzymatic inactivation of the antibiotics.[40,41]

While the three-dimensional (3D) biofilm structure and potential reduction in diffusion are factors in antibiotic resistance they do not explain why even after eventual saturation of the biofilm with antibiotics there is ineffective eradication of bacterial cells. Multiple authors have

revealed a significant nutrient and oxygen gradient across the biofilm.[46,47] Oxygen levels and protein synthesis are directly linked to metabolic activity in the bacterial cells with only metabolically active cells having normal antibiotic susceptibility.[48,49] Near the biofilm surface, bacteria remain in an aerobic metabolic state and are readily killed with chemotherapy. In contrast, bacteria in the biofilm interior transition to an anaerobic metabolic state, with far less susceptibility to aminoglycoside antibiotics.[46,47]

Along with nutrient driven metabolic changes, it is known that some subset of the population (~1%) will experience a phenotypic change resulting in immunity to antibiotics. This phenomena was first observed by Joseph Bigger, an army doctor in World War 2.[50] After observing reoccurrence of infections following penicillin treatment, he isolated a staphylococcal subset in the lab resistant to penicillin. After culturing this subset and subsequent exposure to penicillin there was no increase in the percentage of surviving bacteria. He concluded that the resistance was not due to mutation and termed these survivors “persistors.” It is thought that these persister cells are used to reseed the colony following catastrophic events such as exposure to antibiotic treatment.[51]

Biofilm eradication becomes more complex when addressing long term infections, like those observed in cystic fibrosis-related chronic pulmonary infection. There has been observed genetic adaptation in chronic infections over several years which leads to a loss of virulence factors. While these factors are important for initial invasion it has been postulated that these factors are also ligands for the immune system and the subsequent loss may yield a more robust population.[52] In addition, these mutations may represent a symbiotic step in preserving the host organism as well as a decreased need to injure the host to generate nutrients. The culmination of these genetic changes is a more diverse and healthy population.

1.4.3 Impact on medical devices and orthopedics

Half of the 2 million cases of nosocomial infections in the United States are credited to indwelling devices.[53] The bulk of these infections occur in either cardiovascular or orthopedic devices with associated direct medical costs of $3 billion annually.[54] It has been predicted that device related infections will continue to rise; a result of increased biomedical implants (14% increase in knee and hip replacement from 1996 to 2001) and an aging population with increased life expectancy.[54] The occurrence of infection has been attributed to the presence of a host derived layer of adhesive proteins such as fibrinogen and collagen followed by adherence of planktonic bacterial cells and formation of biofilm in and around the implanted device.[53] The process of protein absorption has been well characterized by Andrade and Hlady et. al. and occurs immediately upon implantation.[55] A survey of nosocomial infection and data from the United States Center of Disease Control (CDC) estimate that 65% of infections in the developed world arise from biofilm formation.[56] It is important to note an alarming trend in device related infection with the emergence of resistant strains of bacteria and a reduction in the effectiveness of current antimicrobial strategy.

1.4.4 Emergence of resistivity: an ongoing concern

Following the widespread use of antibiotics in the 1940s each sequential decade brought the emergence of drug resistant strains, including strains with resistance to multiple drugs.[57] Drug resistance first appeared in hospitals where antibiotics were used frequently. Sulfonamide resistant Streptococcus emerged from military hospitals in the 1930s and penicillin-resistant Staphylococcus aureus arose from London hospitals shortly after penicillin's introduction in the 1940s.[58–60] Fueled by increases in antibiotic use, the rise of resistant strains became more and more frequent. The 1980s saw a re-emergence of tuberculosis in multidrug resistant strains.[61]

Currently in the United States 40-60% of *S. aureus* nosocomial infections are methicillin – resistant (MRSA).[58,62] There have even been a handful of isolated cases of MRSA with resistivity to vancomycin, that until the expansion of new drugs daptomycin and linezolid, was a last line of defense. *P.aeruginosa* strains have been found that are resistant to most anitbiotics and have resulted in deaths, especially in immune-compromised patients.[58,63,64] There are indications that biofilms may facilitate development of resistant strains. Bacterial strains can experience a gradual increase in resistance as the use of antibiotics suppresses susceptible strains while selecting for resistant cells. Additionally, drug resistant genes can be shared between bacterium through mechanisms including plasmids, bacteriophages, naked DNA or transpoons.[57,58] These mutations can directly lead to mechanisms of resistance such as antibiotic efflux pumps, and antibiotic degrading or altering enzymes. In bacteria dense communities like biofilms, the spread of resistant genes is promoted. In 1999, Hausner and Wuertz used fluorescent labeling and confocal laser scanning microscopy to quantitatively show that *P.aeruginosa* in biofilms could transfer plasmids between cells 1000 times faster than planktonic cells.[65] This ongoing concern over the spread of resistant organisms will be addressed in Chapters 3 and 4, where a localized sustained tobramycin release profile could maintain high local drug concentrations and speculatively reduce the risk of creating resistant strains.

1.5 Cystic fibrosis an impactful future for polyphosphate-tobramycin complex coacervates

1.5.1 Cystic fibrosis leads to chronic pulmonary infection with biofilm presence

Cystic fibrosis (CF) is a life shortening genetic disease, with a higher prevalence in Caucasian populations.[66] Mutation occurs in the cystic fibrosis transmembrane conductance regulator (CFTR) gene leading to abnormal CFTR protein. This abnormality results in ineffective ion

transport across epithelial mucosal cells leading to NaCl and water imbalance and consequently viscous, sticky mucus excretions.[67–70] Associated complications include: liver disease, pancreatic insufficiency, diabetes, and chronic lung infection, the leading cause of CF related death.[66,71,72]

The effect of CF on the lungs is profound and disrupts normal lung immune response. The primary factor reducing the pulmonary immune response is unclear but is speculated to multifaceted. Frustrated mucosal clearance from the airways provides an ideal niche for the invasion of opportunistic bacteria. Recent publications by Mike Welsh et. al. have revealed a link between the absence of CFTR protein with low secretion of HCO_3 which, in the presence of continued proton release, results in lower pH or acidification of the surface airway liquid.[73] This acidification has been proposed as an important factor for explaining reduced effectiveness of the host immune system.[73] The combination of reduced hydration in mucus, lack of mucosal clearance, surface airway acidification, and formation of biofilms illustrates the complex environment that has resulted in the presence of chronic airway infection in cystic fibrosis.

Most CF patients experience acute infection of gram-negative *Pseudomonas aeruginosa* which eventually progresses into chronic biofilm based infection in almost all cases.[52] Despite ongoing research and clinical efforts to eradicate chronic infection in CF patients, there is to date no successful solution for eradicating chronic *P.aeruginosa* infection.[52,74,75]

State of the art care guidelines for *P.aeruginosa* infection includes inhaled tobramycin (aminoglycoside) for 28 day cycles.[76] Accumulation of tobramycin on bacterial cell surface triggers energy dependent uptake into the cell, where subsequent binding to RNA prevents protein synthesis, resulting in cell death.[77] While this approach has shown success in early acute infection, it is ineffective in terms of total eradication of chronic infection. Additionally, the burden of taking multiple doses per day for 28 day cycles, including the time to nebulize the drug and sanitize the equipment after every dose, leads to decreased patient compliance. This

is further exacerbated by additional time intensive tangential therapies including physical therapy and pharmaceutical treatments for inflammation of airways, mucolytics, digestion, diabetes, and liver disease. While these metrics are difficult to measure, the compliance rates for some treatments is estimated to be as low as 16-20%.[78–81]

Chronic *P.aeruginosa* infection in CF airways presents an impactful opportunity for a sustained tobramycin releasing material. While Chapters 2-4 will focus on the application of bulk hydrogels, Chapter 5 will present the applicability of a micro-particle polyphosphate-tobramycin material for pulmonary delivery of aminoglycosides. This is significant not only as a means of eradicating chronic infection, but also as a means of decreasing patient care burdens and improving compliance by reducing the number of required daily doses of tobramycin.

1.5.2 The phenomena of complex coacervation

Coacervation is a liquid-liquid phase separation in a colloidal system. The more concentrated colloid component is termed the coacervate while the other more dilute phase is the equilibrium solution. The coacervation process is entropically driven and has been associated with delocalization of counter ions from poly-cationic and poly-anionic components to form a neutral "complex".[82] Coacervations derived from polyelectrolytes have thus been coined complex coacervations.

The phenomena was first identified by F.W. Tiebackx in 1911 but not thoroughly investigated until 1929 when Bungenberg de Jong et.al. reported on a gum Arabic-gelatin coacervate.[83,84,82] The first theoretical model for coacervation was proposed by J. Overbeek and M. Voorn in 1957.[85] This model described complex coacervation as a competition between electrical attraction and accumulation of charged particles, based on Debye-Huckel equations, and an entropic dispersing force, based on the Flory-Huggins theory for entropy. Since its

publication, extensions have been made to the Voorn-Overbeek theory to better fit unique circumstances such as aggregation of soluble complexes and excess polyions.[86–88] In a recent review of complex coacervation theory, Charles Sing compared Voorn-Overbeek and extensions with work by Borue and Erukhimovich involving random phase approximation (RPA) that describes a globular structure of coacervate droplets and subsequent aggregation.[89] RPA theory predicts aggregation due to a tradeoff between increased hydration area and entropic release of counter ions. Sing also extended a comparison to include modern theories including complexation theory, field theory and molecular dynamic simulation.[88] While Sing states that "a unified theory of complex coacervation is still missing," it is evident that all theories point to a entropic driven process from release of counter ions and electrostatic interactions between polyelectrolytes.[88] Work by Renko Vries et. al. described the physiochemical conditions for complexes to stay in solution.[82] It was predicted that strong polyelectrolytes may form precipitates rather than liquid coacervate, charge balancing leads to maximum coacervate yield, and salt will have a dissociating effect on complex formation at both high and low concentrations.[82]

1.5.3 Adapting coacervates for treatment of cystic fibrosis

Stewart and Wang et. al. derived inspiration for a synthetic complex coacervate from naturally occurring underwater glue of the Sandcastle worm (Phragmatopoma californica).[90] The sandcastle glue protein composition contains more than 50 mol % Ser and Gly residues, and thus has many negatively charged carboxyl groups (Gly) and over 90% of Ser residues phosphorylated. Elemental analysis revealed the presence of Mg^{2+} and Ca^{2+} at ratios of 0.6 to 1.0 metals per phosphate respectively. Although the authors discounted the role of complex coacervation in the formation of sandcastle glue, it directly led to the use of synthetic glue silk

analogs for complex coacervation.

The work with sandcastle glue analogs for underwater adhesives is similar to the exploration of caddisfly silk analogs for the purpose of designing a tobramycin releasing polyphosphate coacervate. Chapter 5 will illustrate the development of polyphosphate coacervates as a pulmonary drug delivery vehicle with sustained release of aminoglycosides. The application of which has great potential for addressing the problem of chronic pulmonary infection in CF patients.

1.6 Motivation and rationale for the study

Recent investigations into mechanochemical characterization of caddisfly silk as a unique underwater material is noteworthy. Caddisfly silk fibers are strong and dissipate large amounts of strain energy before completely recovery. The remarkable strength is particularly impressive for a highly hydrated material. Unfortunately, there is no current method for harvesting large quantities of natural caddisfly silk. Any impactful result of the caddisfly silk discoveries may necessarily arise from the development of a caddisfly silk analog that mimics the mechanochemical components of the natural silk.

The short term motivation for the study is to view the caddisfly silk as a naturally occurring underwater hydrogel. From this vantage point it is reasonable to incorporate caddisfly silk components, primarily dense regions of phosphates crosslinked by divalent metals into a double network hydrogel. While recent strides in hydrogel design have addressed the mechanical shortcoming of traditionally weak and brittle hydrogels they fall well short of replicating the stiffness, strength and toughness of caddisfly silk, Table 1.1. The work presented here aims to advance the field of tough hydrogels through caddisfly inspired design principles. Additionally, the inclusion of caddisfly like features into a synthetic material serves as proof on

concept and confirmation for the explanations and hypothesis presented in the works of Russel Stewart and Nicholas Ashton.

The study also aims to make new strides in controlled drug delivery. Incorporation of aminoglycoside antibiotics as electrostatic crosslinks and structural components of the hydrogels, pushes the boundaries of the current state of the art in drug delivery. Furthermore, there exists a gap in the literature in terms of hybrid hydrogels that combines toughening mechanisms with sustained drug elution. The motivation of this study is to fill that gap and provide a tough, highly hydrated material for use as structural biomaterials with the dual purpose of preventing and fighting infection.

Over the long term it is hoped that these materials will eventually be used in new orthopedic implants like knee or hip arthroplasty with the ability to decrease incidences of infection. These materials may possibly serve a role in revision surgeries, where it may be necessary to eradicate an established infection. Tough, drug eluting hydrogels could also be used as surface coatings or materials for invasive devices such as stents, heart valves, vascular access lines, and catheters.

Of particular importance is the potential use of this material in coacervate form as a pulmonary delivery system for tobramycin in CF patients. Almost all CF patients suffer from chronic and sometimes debilitating lung infection that leads to decreased lung function and ultimately death. To date, there is no known cure for CF or any successful method at eradicating chronic infection. It is the hope of this author that these new materials may provide a better platform for attacking chronic CF infection, while directly leading to better patient compliance and thus more promising clinical results.

Table 1.1: Mechanical properties of DN hydrogels

1st Network	2nd Network	Description	Modulus	Stress at Fail	Strain at Fail	Recovery % and (Time)	REF
PAMPS	pAAm	Interpenetrating Network (IPN)	--	21 MPa	98%	None	80
Cellulose	Gelatin	IPN	21 MPa	3.8 MPa	28%	None	91
Agarose	PEG	IPN	149 kPa	1.6 MPa	90%	None	92
PDGI	pAAm	Lamellar Bilayers	--	0.6 MPa	2200%	100% (30m)	82
MPC	PEGDA	Dipole-Dipole	2.8 MPa	3.5 MPa	255%	--	83
MPTC	NaSS	Ionic Crosslinks	8 MPa	1.8 MPa	750%	100% (2h)	84
PMMA	PMAA	Metal Crosslinks	21 MPa	0.86 MPa	420%	61% (12h)	86
Alginate	pAAm	Metal Crosslinks	29 kPa	0.16 MPa	2000%	74% (1d)	85
Gellam Gum	pAAm	Metal Crosslinks	121 kPa	0.216	77%	53% (80m)	93
PDMA	Silica	Silica Hybrid	175 kPa	0.45	260%	--	94
PVA	PEG	Controlled Structure	160 kPa	5.1	40000 %	None	95
PAMPS	pAAm	IPN with Controlled micro-structure	400 kPa	0.9	1100%	None	96
Agarose	PAM	Physical Entaglement	123 kPa	0.16	2250%	65% (10m)	81
TAPEG	TNPEG	Tetrahedran	40 kPa	4	90%	--	28
Caddisfy Silk		Natural Material	86.5 MPa	32.7	130%	100% (120m)	9
pPEMA	pAAm	Caddisfly Mimetic	34.2 MPa	3.8	90%	100% (30m)	19

A

B

C

Figure 1.1. Photographs of caddisfly insects A) Photograph of caddisfly larvae with rock case, collected from Red Butte Creek, Salt Lake City. B) Photograph of caddisfly larvae with case partially composed of glass beads. C) Photograph of adult caddisfly.

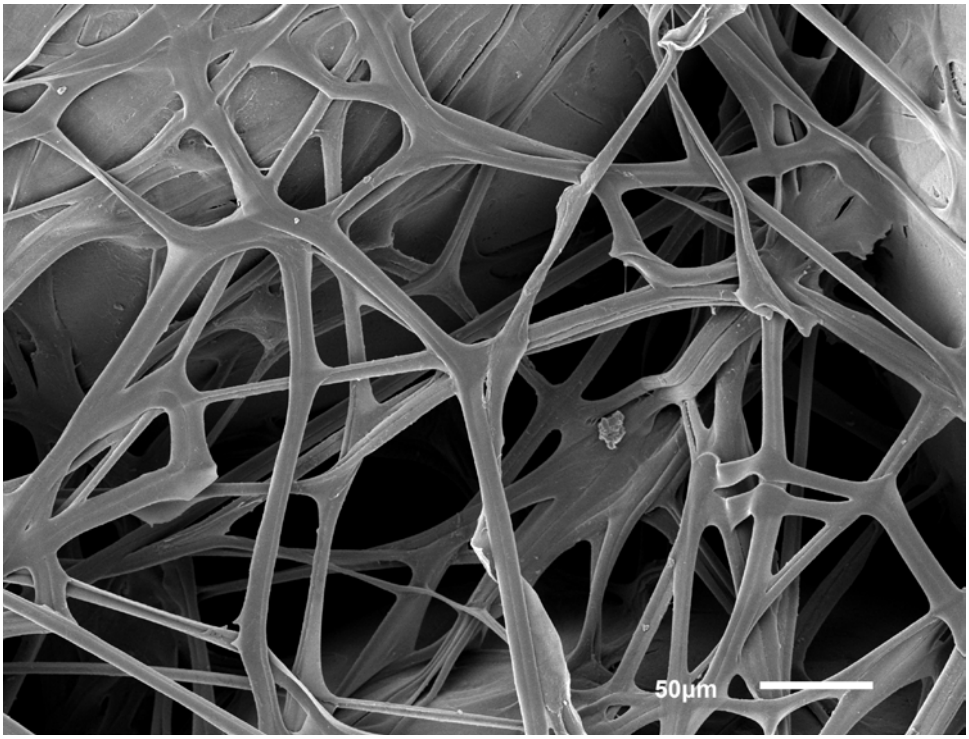

Figure 1.2. SEM image of caddisfly silk. Showing stitching pattern of caddisfly silk between pieces of the case with adhesions apparent between silk and substrate and silk-silk adhesions.

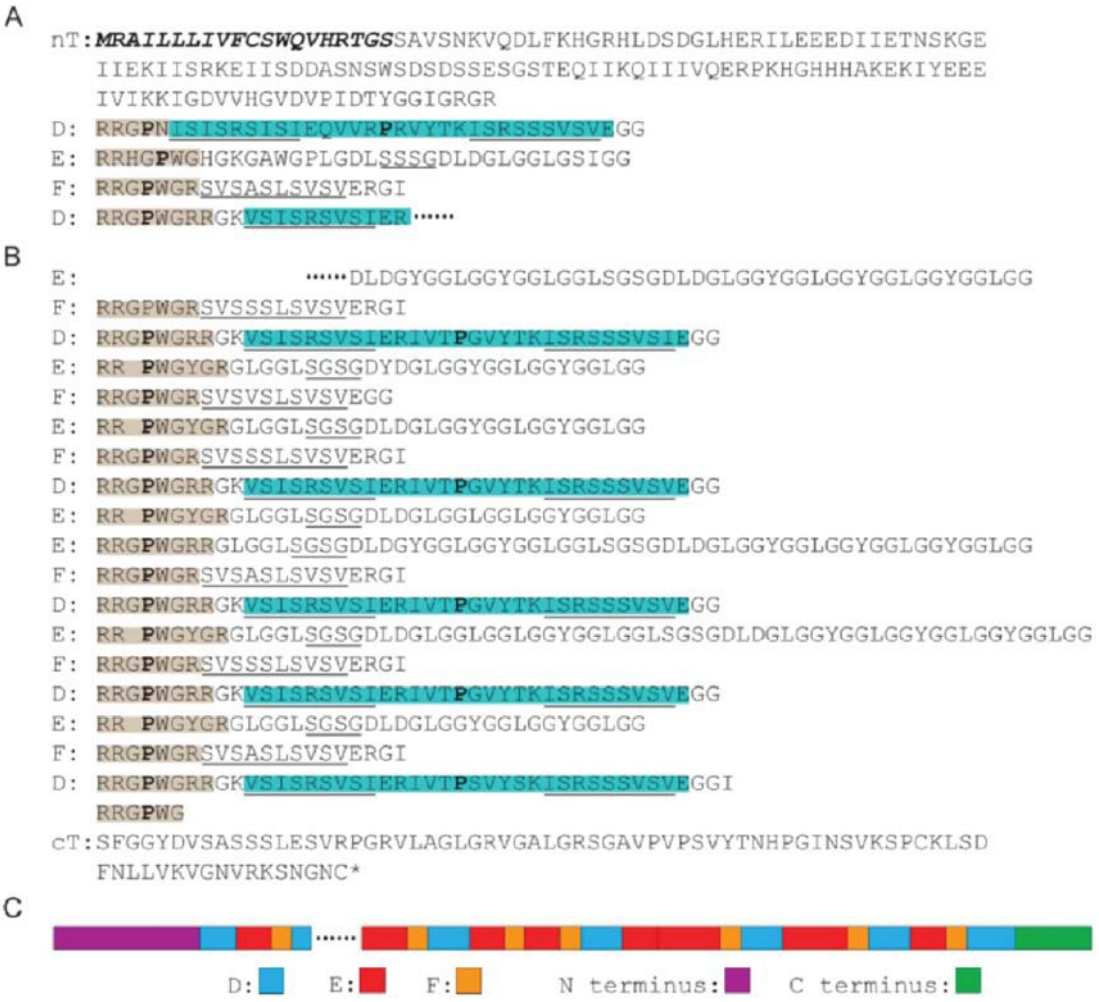

Figure 1.3. Partial *Hesperophylax sp.* H-fibroin sequence. The continuous sequences are arranged to highlight the pattern of conserved D, E, and F subrepeats. The shared arginine-rich motif with a central proline is highlighted in gray. (pSX)n motifs are underlined. The hypothetical [(pSX)4]2 β- hairpin sequence is highlighted in turquoise. (A) N-terminus. Bold italics indicates the secretion signal peptide. (B) C-terminus; * = stop codon. (C) Schematic representation of the irregularly repeating pattern of conserved subrepeats. This figure was published by Stewart et. al. and used with permission.[10]

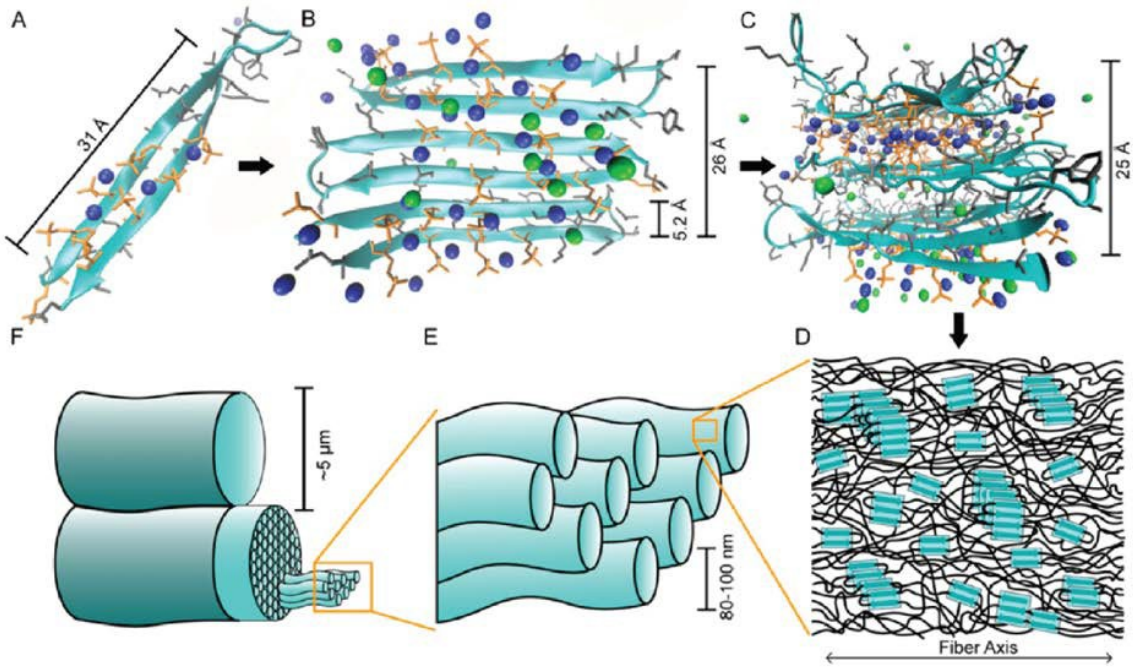

Figure 1.4. Hypothetical molecular structure of caddisflyH-fibroin β-domains and silk fibers. (A) Representative structure the D subrepeat $[Ca^{2+}(pSX)_4]_2$ β-hairpin from cluster analysis of a 40 ns MD simulation. Ca^{2+} = blue spheres, Cl^- = green spheres. (B) Representative structure after 10 ns of MD simulation of an extended β-sheet modeled with three antiparallel $[Ca^{2+}(pSX)_4]_2$ β-hairpins. (C) Representative structure of a three- sheet β-domain stabilized through alternating pS-Ca^{2+} bridged interfaces and hydrophobic interfaces. Calculated dimensions of the domains are indicated. (D) Macroscale nanocomposite fiber model: semicrystalline Ca^{2+}-stabilized, pS-rich β-domains (turquoise) form interfiber cross-links connected by amorphous regions (black). (E) The core of the silk fiber consists of 100−80 nm nanofibrils (turquoise) running parallel with the macrofiber axis. (F) The paired subfibers (turquoise) are fused together and have a thin, poorly characterized peripheral layer (blue). This figure was published by Stewart et. al. and used with permission.[10]

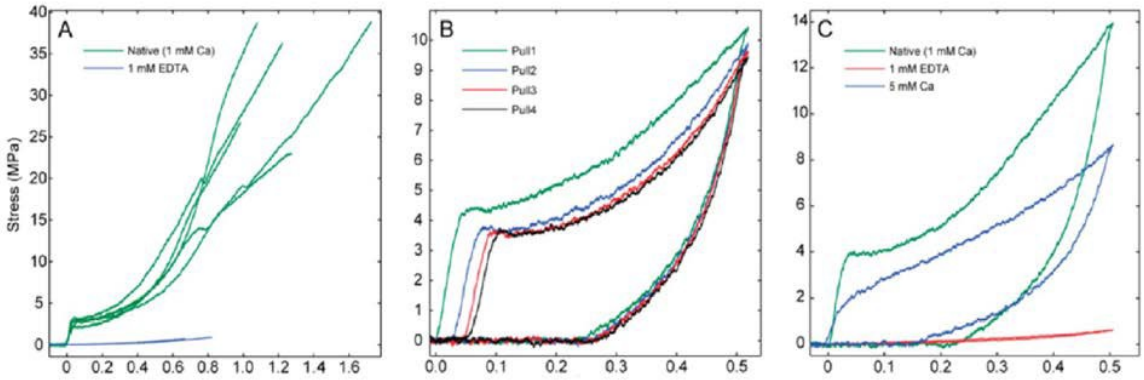

Figure 1.5: Single caddisfly fiber mechanics. (A) Five fibers were stained to failure in 1 mM Ca^{2+} (green) or in 1 mM EDTA (blue). (B) Force−extension profiles of a single native fiber cyclically loaded 4 times to 0.5 in 1 mM Ca^{2+}. The fiber was relaxed for 15 m between each strain cycle. (C) Green: force−extension profile from the third cycle of a single fiber cyclically loaded three times to 0.5 in 1 mMCa^{2+}. Red: force−extension profile of a fiber cycled to 0.5 after 30 m in 1 mM EDTA. Blue: force−extension profile 24 h after replacing EDTA with 5 mM Ca^{2+} and cycling to 0.5 strain. This figure was published by Stewart et. al. and used with permission.[10]

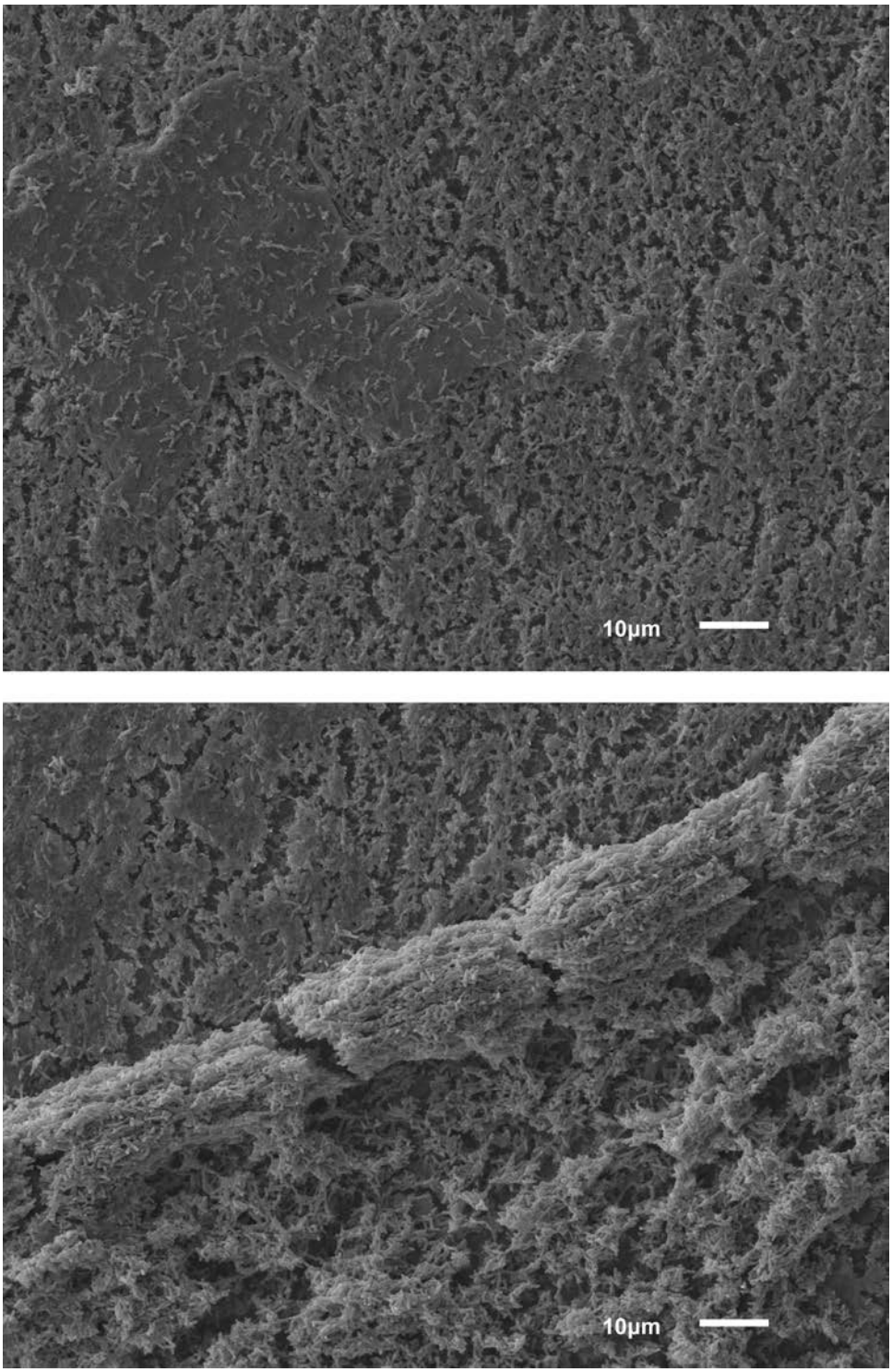

Figure 1.6 SEM images of pseudomonas aeruginosa biofilms. Biofilms were grown with a modified CDC biofilm reactor onto stainless steel coupon surfaces.

1.7 References

(1) Fratzl, P. Biomimetic Materials Research: What Can We Really Learn from Nature's Structural Materials? *J. R. Soc. Interface* **2007**, *4* (15), 637–642 DOI: 10.1098/rsif.2007.0218.

(2) Lakes, R. Materials with Structural Hierarchy. *Nature* **1993**, *361*, 511–515.

(3) Sponner, A.; Vater, W.; Monajembashi, S.; Unger, E.; Grosse, F.; Weisshart, K. Composition and Hierarchical Organisation of a Spider Silk. *PLoS One* **2007**, *2* (10), e998 DOI: 10.1371/journal.pone.0000998.

(4) Aldersey-Williams, H. Towards Biomimetic Architecture. *Nat. Mater.* **2004**, *3*, 277–279.

(5) Gebeshuber, I. C.; Drack, M. An Attempt to Reveal Synergies between Biology and Mechanical Engineering. *Proc. Inst. Mech. Eng. Part C J. Mech. Eng. Sci.* **2008**, *222*, 1281–1287 DOI: 10.1243/09544062JMES890.

(6) Jeronimidis, G.; Chimica, D.; Atkins, A. G. Mechanics of Biological Materials and Structures : Nature' S Lessons for the Engineer. *Proc. Inst. Mech. Eng. Part C J. Mech. Eng. Sci.* **1995**, *209*, 221–235.

(7) Keckes, J.; Burgert, I.; Frühmann, K.; Müller, M.; Kölln, K.; Hamilton, M.; Burghammer, M.; Roth, S. V; Stanzl-tschegg, S.; Fratzl, P. Cell-Wall Recovery after Irreversible Deformation of Wood. *Nat. Mater.* **2003**, *2* (December), 810–814 DOI: 10.1038/nmat1019.

(8) Wiggins, G. B. *Caddisflies: The Underwater Architects*; University of Toronto Press: Toronto, 2004.

(9) Ashton, N. N.; Roe, D. R.; Weiss, R. B.; Cheatham, T. E.; Stewart, R. J. Self-Tensioning Aquatic Caddisfly Silk: Ca2+-Dependent Structure, Strength, and Load Cycle Hysteresis. *Biomacromolecules* **2013**, *14* (10), 3668–3681 DOI: 10.1021/bm401036z.

(10) Ashton, N. N.; Stewart, R. J. Self-Recovering Caddisfly Silk: Energy Dissipating, Ca(2+)-Dependent, Double Dynamic Network Fibers. *Soft Matter* **2014** DOI: 10.1039/c4sm02435d.

(11) Wang, C.-S.; Ashton, N. N.; Weiss, R. B.; Stewart, R. J. Peroxinectin Catalyzed Dityrosine Crosslinking in the Adhesive Underwater Silk of a Casemaker Caddisfly Larvae, Hysperophylax Occidentalis. *Insect Biochem. Mol. Biol.* **2014**, *54*, 69–79 DOI: 10.1016/j.ibmb.2014.08.009.

(12) Ashton, N. N.; Pan, H.; Stewart, R. J.; Stewart, R. J. Connecting Caddisworm Silk Structure and Mechanical Properties : Combined Infrared Spectroscopy and Mechanical Analysis. *Open Biol.* **2016**, *6*.

(13) Addison, J. B.; Ashton, N. N.; Weber, W. S.; Stewart, R. J.; Holland, G. P.; Yarger, J. L. β-Sheet Nanocrystalline Domains Formed from Phosphorylated Serine-Rich Motifs in Caddisfly Larval Silk: A Solid State NMR and XRD Study. *Biomacromolecules* **2013**, *14* (4),

1140–1148 DOI: 10.1021/bm400019d.

(14) Wang, C.; Pan, H.; Weerasekare, G. M.; Stewart, R. J.; Stewart, R. J. Peroxidase-Catalysed Interfacial Adhesion of Aquatic Caddisworm Silk. *Interface* **2015**, *12*, 1–11.

(15) Stewart, R. J.; Wang, C. S. Adaptation of Caddisfly Larval Silks to Aquatic Habitats by Phosphorylation of H-Fibroin Serines. *Biomacromolecules* **2010**, *11* (4), 969–974 DOI: 10.1021/bm901426d.

(16) Warwicker, J. O. Comparative Studies of Fibroins. *J. Mol. Biol.* **1960**, *2* (6), 350–IN1 DOI: 10.1016/S0022-2836(60)80046-0.

(17) Sehnal, F.; Sutherland, T. Silks Produced by Insect Labial Glands. *Prion* **2008**, *2*, 145–153 DOI: 10.4161/pri.2.4.7489.

(18) Yonemura, N.; Mita, K.; Tamura, T.; Sehnal, F. Conservation of Silk Genes in Trichoptera and Lepidoptera. *J. Mol. Evol.* **2009**, *68*, 641–653 DOI: 10.1007/s00239-009-9234-5.

(19) Lane, D. D.; Kaur, S.; Weerasakare, G. M.; Stewart, R. J. Toughened Hydrogels Inspired by Aquatic Caddisworm Silk. *Soft Matter* **2015**, *11*, 6981–6990 DOI: 10.1039/C5SM01297J.

(20) Wichterle, O.; Lím, D. Hydrophilic Gels for Biological Use. *Nature* **1960**, *185* (4706), 117–118 DOI: 10.1038/185117a0.

(21) Buwalda, S. J.; Boere, K. W. M.; Dijkstra, P. J.; Feijen, J.; Vermonden, T.; Hennink, W. E. Hydrogels in a Historical Perspective: From Simple Networks to Smart Materials. *J. Control. Release* **2014**, *190*, 254–273 DOI: 10.1016/j.jconrel.2014.03.052.

(22) Van Vlierberghe, S.; Dubruel, P.; Schacht, E. Biopolymer-Based Hydrogels as Scaffolds for Tissue Engineering Applications: A Review. *Biomacromolecules* **2011**, *12* (5), 1387–1408 DOI: 10.1021/bm200083n.

(23) Qiu, Y.; Park, K. Environment-Sensitive Hydrogels for Drug Delivery. *Adv. Drug Deliv. Rev.* **2012**, *64* (SUPPL.), 49–60 DOI: 10.1016/j.addr.2012.09.024.

(24) Kopeček, J. Hydrogel Biomaterials: A Smart Future? *Biomaterials* **2007**, *28* (34), 5185–5192 DOI: 10.1016/j.biomaterials.2007.07.044.

(25) Vandermeulen, G. W. M.; Klok, H. A. Peptide/protein Hybrid Materials: Enhanced Control of Structure and Improved Performance through Conjugation of Biological and Synthetic Polymers. *Macromol. Biosci.* **2004**, *4* (4), 383–398 DOI: 10.1002/mabi.200300079.

(26) Gong, J. P. Why Are Double Network Hydrogels so Tough ? *Soft Matter* **2010**, *6*, 2583–2590 DOI: 10.1039/b924290b.

(27) Okumura, Y.; Ito, K. The Polyrotaxane Gel: A Topological Gel by Figure-of-Eight Cross-Links. *Adv. Mater.* **2001**, *13* (7), 485–487 DOI: 10.1002/1521-4095(200104)13:7<485::AID-ADMA485>3.0.CO;2-T.

(28) Sakai, T.; Matsunaga, T.; Yamamoto, Y.; Ito, C.; Yoshida, R.; Suzuki, S.; Sasaki, N.; Shibayama, M.; Chung, U. Design and Fabrication of a High-Strength Hydrogel with Ideally Homogeneous Network Structure from Tetrahedron-like Macromonomers. *Macromolecules* **2008**, *41* (14), 5379–5384 DOI: 10.1021/ma800476x.

(29) Li, H. J.; Haraguchi, K. Mechanical Properties and Structure of Polymer-Clay Nanocomposite Gels with High Clay Content. *Macromolecules* **2006**, *39*, 1898–1905 DOI: 10.1021/ma052468y.

(30) Gong, J. P.; Katsuyama, Y.; Kurokawa, T.; Osada, Y. Double-Network Hydrogels with Extremely High Mechanical Strength. *Adv. Mater.* **2003**, *15* (14), 1155–1158 DOI: 10.1002/adma.200304907.

(31) Chen, Q.; Zhu, L.; Zhao, C.; Wang, Q.; Zheng, J. A Robust, One-Pot Synthesis of Highly Mechanical and Recoverable Double Network Hydrogels Using Thermoreversible Sol-Gel Polysaccharide. *Adv. Mater.* **2013**, *25* (30), 4171–4176 DOI: 10.1002/adma.201300817.

(32) Haque, M. A.; Kurokawa, T.; Kamita, G.; Gong, J. P. Lamellar Bilayers as Reversible Sacrificial Bonds To Toughen Hydrogel: Hysteresis, Self-Recovery, Fatigue Resistance, and Crack Blunting. *Macromolecules* **2011**, *44* (22), 8916–8924 DOI: 10.1021/ma201653t.

(33) Bai, T.; Zhang, P.; Han, Y.; Liu, Y.; Liu, W.; Zhao, X.; Lu, W. Construction of an Ultrahigh Strength Hydrogel with Excellent Fatigue Resistance Based on Strong Dipole–dipole Interaction. *Soft Matter* **2011**, *7* (6), 2825 DOI: 10.1039/c0sm01108h.

(34) Sun, T. L.; Kurokawa, T.; Kuroda, S.; Ihsan, A. Bin; Akasaki, T.; Sato, K.; Haque, M. A.; Nakajima, T.; Gong, J. P. Physical Hydrogels Composed of Polyampholytes Demonstrate High Toughness and Viscoelasticity. *Nat. Mater.* **2013**, *12* (10), 932–937 DOI: 10.1038/nmat3713.

(35) Sun, J.-Y.; Zhao, X.; Illeperuma, W. R. K.; Chaudhuri, O.; Oh, K. H.; Mooney, D. J.; Vlassak, J. J.; Suo, Z. Highly Stretchable and Tough Hydrogels. *Nature* **2012**, *489* (7414), 133–136 DOI: 10.1038/nature11409.

(36) Henderson, K. J.; Zhou, T. C.; Otim, K. J.; Shull, K. R. Ionically Cross-Linked Triblock Copolymer Hydrogels with High Strength. *Macromolecules* **2010**, *43* (14), 6193–6201 DOI: 10.1021/ma100963m.

(37) Costerton, J. W. How Bacteria Stick. *Sci. Am.* **1978**, *238*, 86–95.

(38) Marrie, T. J.; Nelligan, J.; Costerton, J. W. A Scanning and Transmission Electron Microscopic Study of an Infected Endocardial Pacemaker Lead. *Circulation* **1982**, *66* (6), 1339–1341 DOI: 10.1161/01.CIR.66.6.1339.

(39) Gristina, A. G.; Costerton, J. W. Bacteria-Laden Biofilms: A Hazard of Orthopedic Prostheses. *Infect. Surg.* **1984**, *3*, 655–662.

(40) Stewart, P. S.; Costerton, J. W. Antibiotic Resistance of Bacteria in Biofilms. *Lancet* **2001**, *358*, 135–138.

(41) Stewart, P. S. Mechanisms of Antibiotic Resistance in Bacterial Biofilms. *Int. J. Med. Microbiol.* **2002**, *113*, 107–113.

(42) Drenkard, E. Antimicrobial Resistance of Pseudomonas Aeruginosa Biofilms. *Microbes Infect.* **2003**, *5*, 1213–1219 DOI: 10.1016/j.micinf.2003.08.009.

(43) Lawrence, J. R.; Korber, D. R.; Hoyle, B. D.; Costerton, J. W.; Caldwell, D. E. Optical Sectioning of Microbial Biofilms. *J. Bac* **1991**, *173* (20), 6558–6567.

(44) Dorrington, S. M.; Slack, M. P. E.; Walmsley, H. L. Inhibition of Tobramycin Diffusion by Binding to Alginate. *Antimicrob. Agents Chemother.* **1988**, *32* (4), 518–523.

(45) Whitchurch, C. B.; Tolker-nielsen, T.; Ragas, P. C.; Mattick, J. S. Extracellular DNA Required for Bacterial Biofilm Formation. *Science (80-.).* **2002**, *295* (22), 1487.

(46) III, M. C. W.; Roe, F.; Bugnicourt, A.; Franklin, M. J.; Stewart, P. S.; Iii, M. C. W.; Roe, F.; Bugnicourt, A.; Franklin, M. J.; Stewart, P. S. Contributions of Antibiotic Penetration , Oxygen Limitation , and Low Metabolic Activity to Tolerance of Pseudomonas Aeruginosa Biofilms to Ciprofloxacin and Tobramycin Contributions of Antibiotic Penetration , Oxygen Limitation , and Low Metabolic Activi. *Antimicrob. Agents Chemother.* **2003**, *47*, 317–323 DOI: 10.1128/AAC.47.1.317.

(47) Borriello, G.; Werner, E.; Roe, F.; Kim, A. M.; Ehrlich, G. D.; Stewart, P. S. Oxygen Limitation Contributes to Antibiotic Tolerance of Pseudomonas Aeruginosa in Biofilms Oxygen Limitation Contributes to Antibiotic Tolerance of Pseudomonas Aeruginosa in Biofilms. *Antimicrob. Agents Chemother.* **2004**, *48* (7), 2659–2664 DOI: 10.1128/AAC.48.7.2659.

(48) Allison, K. R.; Brynildsen, M. P.; Collins, J. J. Metabolite-Enabled Eradication of Bacterial Persisters by Aminoglycosides. *Nature* **2011**, *473* (7346), 216–220 DOI: 10.1038/nature10069.

(49) Gilbert, P.; Collier, P. J.; Brown, M. R. Influence of Growth Rate on Susceptibility to Antimicrobial Agents: Biofilms, Cell Cycle, Dormancy, and Stringent Response. *Antimicrob. Agents Chemother.* **1990**, *34* (10), 1865–1868 DOI: 10.1128/AAC.34.10.1865.

(50) Balaban, N. Q. Persistence: Mechanisms for Triggering and Enhancing Phenotypic Variability. *Curr. Opin. Genet. Dev.* **2011**, *21*, 768–775 DOI: 10.1016/j.gde.2011.10.001.

(51) Davies, D. G.; Parsek, M. R.; Pearson, J. P.; Iglewski, B. H.; Costerton, J. W.; Greenberg, E. P. The Involvement of Cell-to-Cell Signals in the Development of a Bacterial Biofilm. *Science (80-.).* **1998**, *280* (April), 295–298.

(52) Singh, P. K. Evolving Stealth: Genetic Adaptation of Pseudomonas Aeruginosa during Cystic Fibrosis Infections. *Proc. Natl. Acad. Sci. U. S. A.* **2009**, *103* (22), 1–5.

(53) Darouiche, R. Treatment of Infections Associated with Surgical Implants. *N. Engl. J. Med.* **2004**, *350*, 1422–1429.

(54) Hetrick, E. M.; Schoenfisch, M. H. Reducing Implant-Related Infections: Active Release Strategies. *Chem. Soc. Rev.* **2006**, *35*, 780–789 DOI: 10.1039/b515219b.

(55) Andrade, J. D.; Hlady, V. Plasma Protein Adsorption: The Big Twelve. *Ann. N. Y. Acad. Sci.* **1987**, *516* (1), 158–172 DOI: 10.1111/j.1749-6632.1987.tb33038.x.

(56) Costerton, J. W. Cystic Fibrosis Pathogenesis and the Role of Biofilms in Persistent Infection. *Trends Microbiol.* **2001**, *9* (2), 50–52 DOI: 10.1016/S0966-842X(00)01918-1.

(57) Levy, S. B. The Challenge of Antibiotic Resistance. *Sci. Am.* **1998**, No. March, 46–53.

(58) Levy, S. B.; Marshall, B. Antibacterial Resistance Worldwide: Causes, Challenges and Responses. *Nat.Med.* **2004**, *10* (1078–8956 (Print)), S122–S129 DOI: 10.1038/nm1145.

(59) Levy, S. Microbial Resitance To Antibiotics An Evolving and Persistent Problem. *Lancet* **1982**, *320* (8289), 83–88 DOI: 10.1016/S0140-6736(82)91701-9.

(60) Barber, M.; Rozwadowska-Dowzenko, M. Infection by Penicillin-Resistant Staphylococci. *Lancet* **1948**, *252* (6530), 641–644 DOI: 10.1016/S0140-6736(48)92166-7.

(61) Bloom, B. R.; Murray, C. J. L. Tuberculosis : Commentary on a Reemergent Killer. *Science (80-.).* **1992**, *257* (5073), 1055–1064.

(62) Weinstein, R. a. Controlling Antimicrobial Resistance in Hospitals: Infection Control and Use of Antibiotics. *Emerg. Infect. Dis.* **2001**, *7* (2), 188–192 DOI: 10.3201/eid0702.700188.

(63) Tenover, F. C.; Weigel, L. M.; Appelbaum, P. C.; McDougal, L. K.; Chaitram, J.; McAllister, S.; Clark, N.; Killgore, G.; O'Hara, C. M.; Jevitt, L.; Patel, J. B.; Bozdogan, B. Vancomycin-Resistant Staphylococcus Aureus Isolate from a Patient in Pennsylvania. *Antimicrob. Agents Chemother.* **2004**, *48* (1), 275–280 DOI: 10.1128/AAC.48.1.275-280.2004.

(64) Weigel, L. M. Genetic Analysis of a High-Level Vancomycin-Resistant Isolate of Staphylococcus Aureus. *Science (80-.).* **2003**, *302* (5650), 1569–1571 DOI: 10.1126/science.1090956.

(65) Hausner, M.; Wuertz, S. High Rates of Conjugation in Bacterial Biofilms as Determined by Quantitative In Situ Analysis. *Appl. Environ. Microbiol.* **1999**, *65* (8), 3710–3713.

(66) Rosenstein, B. J.; Cutting, G. R. The Diagnosis of Cystic Fibrosis: A Consensus Statement. *J. Pediatr.* **1998**, *132* (4), 589–595 DOI: 10.1016/S0022-3476(98)70344-0.

(67) Cheng, S. H.; Gregory, R. J.; Marshall, J.; Paul, S.; Souza, D. W.; White, G. a; O'Riordan, C. R.; Smith, a E. Defective Intracellular Transport and Processing of CFTR Is the Molecular Basis of Most Cystic Fibrosis. *Cell* **1990**, *63* (4), 827–834 DOI: 10.1016/0092-8674(90)90148-8.

(68) Sheppard, D. N.; Ostedgaard, L. S. Understanding How Cystic Fibrosis Mutations Cause a Loss of Cl- Channel Function. *Mol.Med.Today.* **1996**, *2* (7), 290–297 DOI: 10.1016/1357-4310(96)10028-9.

(69) Quinton, P. M. Chloride Impermeability in Cystic Fibrosis. *Nature* **1983**, *301*, 421–422.

(70) Welsh, M. J.; Smith, a. E. Molecular Mechanisms of CFTR Chloride Channel Dysfunction in Cystic Fibrosis. *Cell* **1993**, *73* (7), 1251–1254 DOI: 10.1016/0092-8674(93)90353-R.

(71) FitzSimmons, S. C. The Changing Epidemiology of Cystic Fibrosis. *J. Pediatr.* **1993**, *122* (1), 1–9 DOI: 10.1128/CMR.00068-09.

(72) Singh, P. K.; Schaefer, a L.; Parsek, M. R.; Moninger, T. O.; Welsh, M. J.; Greenberg, E. P. Quorum-Sensing Signals Indicate That Cystic Fibrosis Lungs Are Infected with Bacterial Biofilms. *Nature* **2000**, *407* (6805), 762–764 DOI: 10.1038/35037627.

(73) Shah, V. S.; Meyerholz, D. K.; Tang, X. X.; Reznikov, L.; Alaiwa, M. A.; Ernst, S. E.; Karp, P. H.; Wohlford-lenane, C. L.; Heilmann, K. P.; Leidinger, M. R.; Allen, P. D.; Zabner, J.; Jr, P. B. M.; Ostedgaard, L. S.; Stoltz, D. A.; Randak, C. O.; Welsh, M. J. Airway Acidification Initiates Host Defense Abnormalities in Cystic Fibrosis Mice. *Science (80-.).* **2016**, *351* (6272), 503–507.

(74) Nguyen, D.; Emond, M. J.; Mayer-Hamblett, N.; Saiman, L.; Marshall, B. C.; Burns, J. L. Clinical Response to Azithromycin in Cystic Fibrosis Correlates with in Vitro Effects on Pseudomonas Aeruginosa Phenotypes. *Pediatr. Pulmonol.* **2007**, *42* (6), 533–541 DOI: 10.1002/ppul.20620.

(75) D'Argenio, D. a.; Wu, M.; Hoffman, L. R.; Kulasekara, H. D.; Déziel, E.; Smith, E. E.; Nguyen, H.; Ernst, R. K.; Larson Freeman, T. J.; Spencer, D. H.; Brittnacher, M.; Hayden, H. S.; Selgrade, S.; Klausen, M.; Goodlett, D. R.; Burns, J. L.; Ramsey, B. W.; Miller, S. I. Growth Phenotypes of Pseudomonas Aeruginosa lasR Mutants Adapted to the Airways of Cystic Fibrosis Patients. *Mol. Microbiol.* **2007**, *64* (2), 512–533 DOI: 10.1111/j.1365-2958.2007.05678.x.

(76) Mogayzel, P. J.; Naureckas, E. T.; Robinson, K. a; Brady, C.; Guill, M.; Lahiri, T.; Lubsch, L.; Matsui, J.; Oermann, C. M.; Ratjen, F.; Rosenfeld, M.; Simon, R. H.; Hazle, L.; Sabadosa, K.; Marshall, B. C. Cystic Fibrosis Foundation Pulmonary Guideline. Pharmacologic Approaches to Prevention and Eradication of Initial Pseudomonas Aeruginosa Infection. *Ann. Am. Thorac. Soc.* **2014**, *11* (10), 1640–1650 DOI: 10.1513/AnnalsATS.201404-166OC.

(77) Taber, H. W.; Mueller, J. P.; Miller, P. F.; Arrow, a S. Bacterial Uptake of Aminoglycoside Antibiotics. *Microbiol. Rev.* **1987**, *51* (4), 439–457.

(78) Zindani, G. N.; H, M. P.; Streetman, D. D.; Pharm, D.; Streetman, D. S.; Pharm, D.; Nasr, S. Z.; D, M. Adherence to Treatment in Children and Adolescent Patients with Cystic Fibrosis. *J. Adolesc. Heal.* **2006**, *38*, 13–17 DOI: 10.1016/j.jadohealth.2004.09.013.

(79) Patricia, R.; Llorente, A.; Bousoño, C.; José, J.; Martín, D. Treatment Compliance in Children and Adults with Cystic Fibrosis. *J. Cyst. Fibros.* **2008**, *7*, 359–367 DOI: 10.1016/j.jcf.2008.01.003.

(80) Ziaian, T.; Sawyer, M. G.; Reynolds, K. E.; Carbone, J. A.; Clark, J. J.; Peter, A.; Couper, J. J.; Kennedy, D.; Martin, A. J.; Staugas, R. E.; French, D. J. Treatment Burden and Health-

Related Quality of Life of Children with Diabetes , Cystic Fibrosis and Asthma. *J. Paediatr. Child Health* **2006**, *42*, 596–600 DOI: 10.1111/j.1440-1754.2006.00943.x.

(81) Sawicki, G. S.; Sellers, D. E.; Robinson, W. M. High Treatment Burden in Adults with Cystic Fibrosis : Challenges to Disease Self-Management. *J. Cyst. Fibros.* **2009**, *8* (2), 91–96 DOI: 10.1016/j.jcf.2008.09.007.

(82) De Kruif, C. G.; Weinbreck, F.; De Vries, R. Complex Coacervation of Proteins and Anionic Polysaccharides. *Curr. Opin. Colloid Interface Sci.* **2004**, *9* (5), 340–349 DOI: 10.1016/j.cocis.2004.09.006.

(83) Tiebackx, F. W. Gleichzeitige Ausflockung Zweier Kolloide. *Colloid Polym. Sci.* **1911**, *8* (4), 198–201.

(84) Bungenberg de Jong, H. G.; Kruyt, H. R. Coacervation (Partial Miscibility in Colloid Systems). *Proc K. Ned. Akad. Wet.* **1929**, *32*, 849–856.

(85) Overbeek, J. T. G.; Voorn, M. J. Phase Separation in Polyelectrolyte Solutions. Theory of Complex Coacervation. *J. Cell. Physiol.* **1957**, *49*, 7–26.

(86) Tainaka, K.-I. Effect of Counterions on Complex Coacervation. *Biopolymers* **1980**, *19* (7), 1289–1298 DOI: 10.1002/bip.1980.360190705.

(87) Veis, A.; Aranyi, C. Phase Separation in Polyelectrolyte Systems. I. Complex Coacervates of Gelatin. *J. Phys. Chem.* **1960**, *64*, 1203–1210.

(88) Sing, C. E. Development of the Modern Theory of Polymeric Complex Coacervation. *Adv. Colloid Interface Sci.* **2016** DOI: 10.1016/j.cis.2016.04.004.

(89) Borue, Y.; Erukhimovich, I. A Statistical-Theory of Globular Polyelectrolyte Complexes. *Macromolecules* **1990**, *23* (15), 3625–3632.

(90) Stewart, R. J.; Wang, C. S.; Shao, H. Complex Coacervates as a Foundation for Synthetic Underwater Adhesives. *Adv. Colloid Interface Sci.* **2011**, *167* (1–2), 85–93 DOI: 10.1016/j.cis.2010.10.009.

(91) Nakayama, a.; Kakugo, a.; Gong, J. P.; Osada, Y.; Takai, M.; Erata, T.; Kawano, S. High Mechanical Strength Double-Network Hydrogel with Bacterial Cellulose. *Adv. Funct. Mater.* **2004**, *14* (11), 1124–1128 DOI: 10.1002/adfm.200305197.

(92) DeKosky, B. J.; Dormer, N. H.; Ingavle, G. C.; Roatch, C. H.; Lomakin, J.; Detamore, M. S.; Gehrke, S. H. Hierarchically Designed Agarose and Poly(ethylene Glycol) Interpenetrating Network Hydrogels for Cartilage Tissue Engineering. *Tissue Eng. Part C. Methods* **2010**, *16* (6), 1533–1542 DOI: 10.1089/ten.tec.2009.0761.

(93) Bakarich, S. E.; Pidcock, G. C.; Balding, P.; Stevens, L.; Calvert, P.; in het Panhuis, M. Recovery from Applied Strain in Interpenetrating Polymer Network Hydrogels with Ionic and Covalent Cross-Links. *Soft Matter* **2012**, *8* (39), 9985 DOI: 10.1039/c2sm26745d.

(94) Lin, W.-C.; Fan, W.; Marcellan, A.; Hourdet, D.; Creton, C. Large Strain and Fracture Properties of Poly(dimethylacrylamide)/Silica Hybrid Hydrogels. *Macromolecules* **2010**, *43*, 2554–2563 DOI: 10.1021/ma901937r.

(95) Zhang, X.; Guo, X.; Yang, S.; Tan, S. Double Network Hydrogel with High Mechanical Strength Prepared from Two Biocompatible Polymers. *… Appl. Polym. …* **2009** DOI: 10.1002/app.

(96) Nakajima, T.; Furukawa, H.; Tanaka, Y.; Kurokawa, T.; Gong, J. P. Effect of Void Structure on the Toughness of Double Network Hydrogels. *J. Polym. Sci. Part B Polym. Phys.* **2011**, *49* (17), 1246–1254 DOI: 10.1002/polb.22293.

CHAPTER 2

TOUGHENED HYDROGELS INSPIRED BY AQUATIC CADDISWORM SILK

Authors Contributions: D.D.L, S.K. and M.W. prepared and synthesized the monomers and polymers. D.D.L. preformed hydrogel synthesis, metal ion equilibration, mechanical characterizations, and spectroscopy. The design of experiments and interpretation of results was done by D.D.L. and R.J.S. D.D.L. and R.J.S. prepared the manuscript with proofreading from M.W.

Soft Matter

PAPER

View Article Online
View Journal | View Issue

Toughened hydrogels inspired by aquatic caddisworm silk

Dwight D. Lane, Sarbjit Kaur, G. Mahika Weerasakare and Russell J. Stewart*

Cite this: *Soft Matter*, 2015, **11**, 6981

Received 26th May 2015,
Accepted 27th July 2015

DOI: 10.1039/c5sm01297j

www.rsc.org/softmatter

Aquatic caddisworm silk is a tough adhesive fiber. Part of the toughening mechanism resides in serial, Ca^{2+}–phosphate crosslinked nano-domains that comprise H-fibroin, the major structural protein. To mimic the toughening mechanism, a synthetic phosphate-*graft*-methacrylate prepolymer, as a simple H-fibroin analog, was copolymerized within a covalent elastic network of polyacrylamide. Above a critical phosphate sidechain density, hydrogels equilibrated with Ca^{2+} or Zn^{2+} ions displayed greatly increased initial stiffness, strain-rate dependent yield behavior, and required 100 times more work to fracture than hydrogels equilibrated with Mg^{2+} or Na^{+} ions. Conceptually, the enhanced toughness is attributed to energy-dissipating, viscous unfolding of clustered phosphate–metal ion crosslinks at a critical stress. The toughness of the bioinspired hydrogels exceeds the toughness of cartilage and meniscus suggesting potential application as prosthetic biomaterials. The tough hydrogels also provide a simplified model to test hypotheses about caddisworm silk architecture, phosphate metal ion interactions, and mechanochemical toughening mechanisms.

Introduction

Despite considerable progress in tissue engineering approaches to regenerate damaged or worn-out soft structural tissues, there likely will always be a need for inert, biocompatible, synthetic replacement materials.[1] Hydrogels of crosslinked water-soluble synthetic polymers have long been candidate materials for soft tissue prosthetics, partly because of their high water content and biocompatibility. Progress has been limited, though, because the structure and mechanical properties of conventional hydrogels have little resemblance to the exquisite hierarchical organization, strength, toughness, and graded mechanics of natural tissues. While the strength and stiffness of conventional hydrogels can be increased toward that of natural connective tissues by increasing the crosslink density, the resulting hydrogels are brittle and fracture at low strains. The usefulness of traditional synthetic hydrogels is also limited by their propensity to swell in watery environments, which further degrades their mechanical attributes.

New and creative approaches to synthesizing hydrogels have led to much tougher and fracture resistant materials more closely suited for soft structural tissue replacement.[2] Hydrogel toughness, as reflected in the work of extension to fracture, is a function of both stiffness and extensibility. A common architectural feature of the new generation of toughened hydrogels are two or more quasi-independent but interspersed networks, a stiffer network of energy-dissipating sacrificial linkages within a softer network of highly extensible linkages.[3–5] Early double-network (DN) hydrogels comprised a densely crosslinked polymer network of 2-acrylamide-2-methylpropanesulfonic acid within a loosely crosslinked elastic polymer network of acrylamide.[6] The DN hydrogel possessed compressive strengths 20–40 times higher than either hydrogel network alone. Because strain energy is dissipated by sacrificial chemical scission of polymer chains in the stiff network, permanent damage accumulates in the double covalent network hydrogels during strain cycles, resulting in poor fatigue resistance. Subsequent toughened DN hydrogel designs replaced the covalent sacrificial network with a network of reversible non-covalent sacrificial crosslinks. A multitude of non-covalent network linkages have been reported, including physical crosslinks,[7,8] hydrophobic bilayers,[9] dipole–dipole coupling,[10] electrostatic bonding between oppositely charged functional groups,[11] metal ion complexes,[12–14] and reversible polymer absorption to solid particles.[15,16] This latter group of DN hydrogels show, to varying extents, self-recovery of their initial dimensions and toughness during cyclical strains. Distinct from DN hydrogels, other reported approaches to toughening hydrogels include the use of multifunctional crosslinkers,[17] and hydrogels with uniform networks synthesized with symmetrical tetrahedral macromers.[18]

The adhesive silk of aquatic caddisworms is a tough natural multi-network fiber.[19,20] The silk is used by the larvae like a pressure-sensitive adhesive tape to bond gathered stones, sticks, or leaves into composite protective structures under water. Like natural tissues, the biphasic fibers contain around 70% water by mass. The initial modulus ranges from 80–140 MPa. The fibers

Department of Bioengineering, University of Utah, Salt Lake City, UT 84112, USA. E-mail: russell.stewart@utah.edu; Tel: +1-801-581-8581

yield at 2–5% strain, after which the stress plateaus, then gradually increases until the fibers fracture at an average stress over 30 MPa and strains of 100–150%. The yield stress shows a logarithmic strain-rate dependence, doubling over a two decade range of strain rates. The work of extension to fracture, around 17 MJ m^{-3}, is higher than the 7 MJ m^{-3} work of extension to fracture of the best reported synthetic DN hydrogels.[11] Caddisworm silk deformation is reversible; when strained to 20% then unloaded, the silk fibers recover 99% of their initial dimensions, stiffness, and strength within 120 min. High strain cycle hysteresis and nearly full recovery allow the fibers to repeatedly dissipate energy to protect interfacial adhesive bonds, and thereby the structural integrity of the composite case. The tough, fatigue resistant, adhesive silk is highly adapted to the caddisworm's construction activities in an energetic aquatic niche. As such, it is an excellent natural source of design principles for development of tough synthetic materials for use in wet environments, including soft tissue prosthetics.

The viscoelasticity, toughness, and self-recovery of caddisworm silk has been attributed to a dynamic multi-network fiber structure.[20] We proposed a working model in which two independent metal ion-crosslinked protein networks each reversibly yield at different critical stress for a given strain rate.[20] Exchange of divalent metal ions in native fibers with monovalent Na^+ ions destroyed fiber stiffness, strength, yield behavior, and toughness.[19] In native fibers, Ca^{2+} is the predominant metal ion.[19,21] In our model, the first and stiffer metal ion-dependent network is crosslinked through Ca^{2+}-phosphoserine (pS) coordination complexes, the second softer network through Ca^{2+}–carboxylate complexes.[20] Our model includes a third, covalently crosslinked network, comprising in part a peripheral ring of peroxidase-catalyzed covalent dityrosine crosslinks,[22] which provides a passive elastic restoring force and memory of the permanent fiber structure to guide recovery of the metal ion-crosslinked yield domains when the fibers are unloaded. Although aquatic caddisworms (Trichoptera) are closely related phylogenetically to terrestrial silkworms (Lepidoptera), with numerous similarities apparent in their silk gland physiology and silk fiber molecular structure,[23,24] the silk toughening mechanisms of caddisworm silk, based on multivalent metal ion coordination complexes, is more akin to other aquatic structural materials,[25] especially the byssal threads of mussels.[26–28]

The Ca^{2+}–phosphate crosslinks reside within and between H-fibroin proteins, by mass the major structural component of the silk fibers. H-fibroin is a large protein, M_m greater than 350 000 g mol^{-1}, with short and unique N- and C-termini flanking the central region, which comprises an imperfectly alternating pattern of three types of sequences blocks. Each type of repeating sequence contains at least one $(pSX)_n$ motif, wherein pS is phosphoserine, X is an aliphatic amino acid or arginine, and n = 2–6.[21,29,30] In total, about 15 mol% of H-fibroin residues are pS, and on the order of 100 $(pSX)_n$ domains occur in each H-fibroin molecule.[20] The $(pSX)_n$ motifs have been predicted to form a serial arrangement of inter- and intrachain Ca^{2+}-stabilized β-domains,[19] on the order of 10 per H-fibroin, which are responsible for the initial stiffness and strength of the fibers, and the unfolding of which under strain is responsible for the distinct pseudo-yield point.[20] The Ca^{2+}–carboxylate crosslinks of the second dynamic network may occur within and between abundant PEVK-like structural proteins that have more than 20 mol% amino acids with carboxylate sidechains.[22]

The multi-network caddisworm silk model[20] relating silk molecular structure to fiber mechanics, and the natural toughening mechanism based on Ca^{2+}–phosphate coordination complexes, provided an initial framework for creating tough biomimetic hydrogels. Here, we report the synthesis of first generation multi-network hydrogels modeled after caddisworm silk with a first network crosslinked by reversible divalent metal ion–phosphate coordination complexes to provide strength, within a second covalently crosslinked elastic network of polyacrylamide to provide extensibility and recovery from deformation. Mechanical characterization of the hydrogels demonstrated that their toughness, as reflected in work of extension to fracture, can exceed that of soft structural tissues, such as cartilage.

Materials and methods

Materials

Phosphorus(v) oxychloride, 2-hydroxyethyl methacrylate, triethylamine, and glycidyl methacrylate were purchased from Alfa Aesar (Ward Hill, MA). 4-Methoxyphenol was purchased from Tokyo Chemical Industry Co., Ltd, (Tokyo, Japan). Methacrylic acid, 2,2′-azobis(2-methylpropionitrile), acrylamide, *N*,*N*′-methylenebisacrylamide, and *N*,*N*,*N*′,*N*′-tetramethylethylenediamine were purchased from Sigma Aldrich (St Louis, MO). Ammonium persulfate was purchased from Fischer Scientific (Pittsburgh, PA).

Phosphate monomer synthesis

2-(Methacryloyloxy)ethyl phosphate (MOEP) was synthesized as described previously.[31] Briefly, phosphorus oxychloride (33.9 g, 220 mmol) was mixed with hydroxyl-ethyl-methacrylamide (HEMA) at a 0.7 : 1 molar ratio in dry toluene (480 ml) under flowing argon. The reaction was stirred at 4 °C while triethylamine (TEA) (77 ml) was added slowly over 10 min. Following addition of TEA, the reaction was stirred under argon gas for 6 h at 22 °C, then filtered to remove precipitated salt. The reaction was cooled to 4 °C before addition of DI water (480 ml), then stirred under argon at 22 °C for 2 h. The reaction was extracted twice with diethyl ether (100 ml). The organic layer was discarded. The aqueous layer was extracted using tetrahydrofuran (THF) and diethyl ether (1 : 2, 12 × 225 ml), then dried over anhydrous sodium sulfate. The monomer was verified by ^{1}H and ^{31}P NMR.

Synthesis of polyMOEP-MA

PolyMOEP was synthesized by free radical polymerization of MOEP (85 mol%), and methacrylic acid (15 mol%) in methanol (12.5 ml mg^{-1} MOEP). The reaction was initiated with azo-bis-isobutyronitrile (AIBN, 4.5 mol%) at 55 °C, and proceeded for 15 h. The product was precipitated with acetone, then dissolved in water (200 ml H_2O per 17 g pMOEP). Subsequently, methacrylate groups (MA) were grafted onto the methacrylic acid

sidechains with glycidyl methacrylate in 9-fold molar excess relative to the methacrylate sidechains. The methacrylated pMOEP (pMOEP-MA) was purified by tangential flow filtration using a Millipore Pellicon 3 cassette filter with an Ultracel 10 kD membrane. The polymer was washed with 10 volumes of water during filtration. The pH was adjusted to 7.3 with NaOH, the product lyophilized, and stored at −20 °C. The resulting phosphate prepolymer contained 62.6 mol% phosphate sidechains, 10.9 mol% HEMA, and 26.5 mol% MA sidechains, as determined by ^{1}H and ^{31}P NMR. The molecular mass (M_n) and polydispersity index (PDI) of pMOEP-MA was determined by size exclusion chromatography (SEC) using an Amersham Pharmacia AKTA-FPLC system equipped with Wyatt MiniDawn Treos (light scattering) and Wyatt Optilab rEX (refractive index) detectors. The Superose 6 HR 10/30 column was equilibrated with 0.1 M sodium acetate (pH 6.5) containing 30% (vol/vol) acetonitrile. The average M_n and PDI were calculated using Wyatt MiniDawn ASTRA software to be 89 kg mol^{-1} and 2.6, respectively.

Hydrogel polymerization

Hydrogels were formed by free radical polymerization of acrylamide (Aam) and *N*,*N*′-methylenebisacrylamide (bis-Aam) with the pMOEP-MA prepolymer in 150 mM NaCl and 5 mM tris (pH 8.0) (Fig. 1). The total wt% of Aam, bis-Aam and MOEP-MA pre-polymer was held constant at 7.5%, while the wt% of the prepolymer was varied from 0.5% to 7.0 wt%. The molar ratio of Aam to bis-Aam was 60 : 1. Polymerization was initiated by adding 10% ammonium persulfate (APS) and tetramethylethylenediamine (TEMED) to final concentrations of 70 μg ml^{-1} and 2.4 μl ml^{-1}, respectively, to the monomer/pre-polymer solution. Polymerization proceeded in dog bone-shaped molds for 90 min at 22 °C. Molds were laser cut from 2 mm thick silicone rubber sheets, which were clamped between two acrylic plates to form the complete molds. A layer of mineral oil was floated on top of the polymerization reaction to limit exposure to oxygen. Polymerized gels were soaked in 150 mM NaCl, 5 mM tris (pH 8) with repeated changes of solution for 24 h to remove unreacted materials.

Hydrogel metal ion exchange

Hydrogels were immersed in 150 mM NaCl, 10 mM tris (pH 8.0) with metal ions (Ca^{2+}, Mg^{2+}, or Zn^{2+}) added in 5 mM increments up to 50 mM over 24 h. Gradual addition of metal ions improved the homogeneity of the deswelled hydrogels. The hydrogels were then soaked in 50 mM metal ion and 10 mM tris (pH 8.0) for an additional 24 h with frequent solution changes. Images of hydrogels were recorded using a dissection microscope during volume equilibration and their dimensions were measured using ImageJ. Isotropic shrinking was assumed to calculate volume changes. Hydrogels were considered to be fully equilibrated when the volume reached steady state. Hydrogel density was measured by the buoyancy method using an analytical balance density kit (Mettler Toledo, Inc.) and calculated using the equation:

$$\rho_{\text{sample}} = \frac{(\text{sample weight}_{\text{air}}) \times (\rho_{\text{water}} - \rho_{\text{air}})}{(\text{sample weight}_{\text{air}} - \text{sample weight}_{\text{water}})} + \rho_{\text{air}}$$

The density of water was corrected for temperature. Metal phosphate ratios were determined by ICP-OES of two independent hydrogel specimens at a commercial testing facility (Advanced Labs, Salt Lake City, UT).

Mechanical testing of hydrogels

Hydrogels were strained while submerged in 5 mM tris, pH 8.0, containing 5 mM of the test metal ion on an Instron 3342 material test system controlled with Bluehill software (Instron, Inc.). Ca^{2+}-equilibrated hydrogels were strained at rates ranging from 0.01 to 1.0 s^{-1}. Strain to fracture and cyclical strain tests were done at 0.15 s^{-1}.

Infrared spectroscopy

Sodium equilibrated hydrogels were incubated overnight in 10 mM Na^{+} EDTA to remove rouge divalent metal ions potentially scavenged

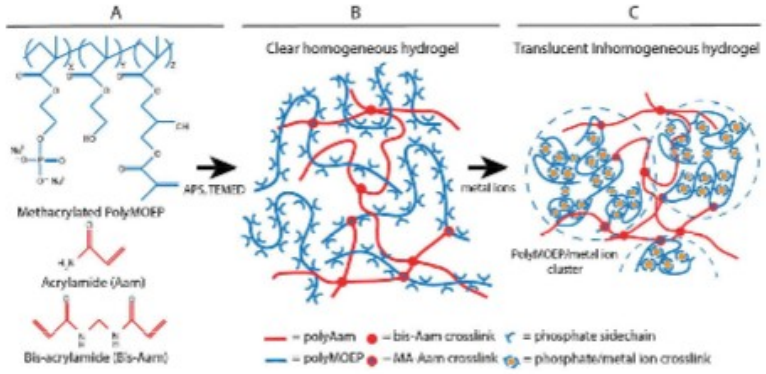

Fig. 1 Double network hydrogel synthesis. (A) The sodium salt of the pMOEP prepolymer was copolymerized with AAm and bis-AAm monomers. The total polymer concentration was kept constant at 7.5 wt%. (B) The pAAm network was covalently connected to the pMOEP network through MA sidechains to form a double network hydrogel. (C) The pMOEP network was crosslinked and de-swelled by exchange of Na^{+} with divalent metal ions (Mg^{2+}, Ca^{2+} and Zn^{2+}). The collapsed pMOEP-divalent metal ion network is conceptualized as dense clusters that function as sacrificial yield domains.

during polymerization and processing. Na^+ gels were stored in 1 mM EDTA to prevent binding of trace divalent metal ions. Divalent metal ion hydrogels were equilibrated with the respective metal ion as described above. After volume equilibration, the samples were rinsed with water, then lyophilized to remove water, and crushed into a powder using an agar mortar and pestle before applying to the diamond ATR crystal. The IR spectra were normalized to the intensity of an absorption band centered at 1665 cm^{-1}, which corresponds to absorption by amide groups in the polymethacrylamide backbone.[43] A linear baseline correction was applied to the intensity normalized spectra between 800 and 1300 cm^{-1}, which contains several phosphate vibrational modes. ATR-FTIR absorbance spectra were collected using a Nicolet 6700 spectrometer (Thermo Scientific, FL) with a diamond Smart iTR accessory, a deuterated triglycine sulfate detector, and a KBr/Ge mid-infrared optimized beamsplitter. Spectra were recorded with a resolution of 4 cm^{-1} and as 512 averaged scans.

Processing of experimental data

Data was processed in matlab (MathWorks). Linear fits to the initial part of the stress strain curve were used to estimate the initial modulus. The yield point was determined using a 5% strain offset from the initial linear portion of the curve. Energy dissipation, strain cycle hysteresis, was computed by subtracting the trapezoidal integration of the reverse curve from the forward curve of cyclical tests. Residual strain was measured by extending the initial linear portion of the stress strain curve (disregarding toe regions) through the base line.

Results

Synthesis of divalent metal-ion crosslinked double network hydrogels

The toughness of natural caddisfly silk is contributed mostly by the Ca^{2+}–phosphate crosslinked $(pSX)_n$ domains in the H-fibroin protein.[20] To create a simple analog of H-fibroin, polymethacrylate random copolymers were synthesized with varying mol% of ethyl-phosphate (MOEP), ethyl-hydroxy (HEMA) sidechains, and carboxylate (MAA) sidechains (Fig. 1A). The MAA groups were subsequently grafted with glycidyl methacrylate as crosslinking groups. To prepare double network hydrogels, the sodium salt of methacrylated polyphosphate (pMOEP-MA) prepolymers were mixed with acrylamide (AAM) and bisacrylamide (bis-AAM) monomers and copolymerized in 150 mM NaCl, and 5 mM tris (pH 8.0). The total wt% of polymer in the hydrogels was kept constant at 7.5 wt%. During polymerization, the pMOEP-MA prepolymer became crosslinked into the pAAM network through the MA sidechains (Fig. 1B). The pAAM network served as an analog of the passive elastic network of natural caddisfly silk. The resulting dog bone-shaped hydrogels, with Na^+ counterions, were clear and transparent.

As Na^+ was exchanged with the divalent metal-ions, Mg^{2+}, Ca^{2+}, and Zn^{2+}, the hydrogels shrank to about 65% of their initial volume (Table 1). The final volume had little dependence on the divalent metal ion species (Fig. 2). However, the hydrogels shrank fastest in Mg^{2+}, equilibrating in 90 min, whereas volume equilibration in both Ca^{2+} and Zn^{2+} took approximately 24 h. During divalent metal ion exchange, the initially transparent Na^+-hydrogels became slightly translucent. The resulting divalent ion-equilibrated DN hydrogels had three types of crosslinks within and between networks: covalent bis-AAM junctions between pAAM chains, covalent bis-AAM junctions between pAAM and methacrylated side chains in pMOEP networks, and reversible phosphate/metal ion junctions within the

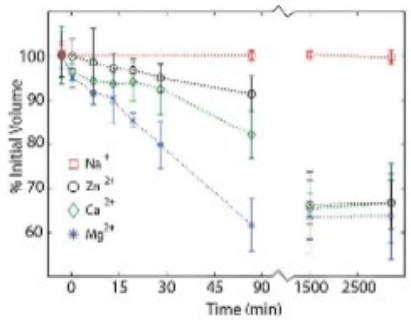

Fig. 2 Hydrogel volume change during metal ion exchange. The hydrogels contained 7.5 total wt% polymer, comprising 6.5 wt% pMOEP and 1.0 wt% pAAm, before deswelling by the addition of divalent metal ions. For each data point n = 3 and error bars = ±1 s.d.

Table 1 Composition and properties of DN hydrogels and native caddisworm silk

	pMOEP/pAAm Hydrogels[a]				Native caddisworm silk[b]
Ion	Zn^{2+}	Ca^{2+}	Mg^{2+}	Na^+	$(Ca^{2+})^c$
Volume (% of initial)	66.2 ± 1.2	66.5 ± 2.1	63.6 ± 3.3	97.2 ± 2.4	—
Water (wt%)	53.6 ± 1.3	55.6 ± 2.1	56.3 ± 1.9	92.5 ± 0.5	66[d]
Density (g cm^{-3})	1.10 ± 0.02	1.07 ± 0.02	1.05 ± 0.02	1.01 ± 0.01	—
M/P molar ratio	3.9	1.7	1.5	—	—
Initial modulus (MPa)	34.2 ± 2.5	10.3 ± 3.5	0.1 ± 0.04	0.04 ± 0.01	86.5 ± 19.2
Yield stress (MPa)	3.5 ± 0.4	1.8 ± 0.2	No yield	No yield	2.8 ± 0.4
Stress at fracture (MPa)	3.8 ± 0.3	1.9 ± 0.1	0.3 ± 0.01	0.05 ± 0.004	32.7 ± 6.6
Elongation at fracture (%)	40 ± 10	90 ± 50	220 ± 20	227 ± 14	126 ± 29
Work to fracture (MJ m^{-3})	10.4 ± 0.4	10.5 ± 1.2	0.3 ± 0.004	0.09 ± 0.01	17.3 ± 6.2

[a] 6.5 wt% pMOEP, 1.0 wt% pAAM. [b] Mechanical data from ref. 16 and 17. [c] Native caddisworm silk contains mostly Ca^{2+}. [d] Unpublished.

pMOEP network, which were likely a mix of inter- and intramolecular crosslinks (Fig. 1C).

The mechanical effect of varying the ratio of the pMOEP-MA prepolymer network to the pAAM network in hydrogels equilibrated with Ca^{2+} ions was evaluated by tensile testing. The concentration of pMOEP-MA prepolymer was varied from 1.5 to 7.0 wt% while holding the total polymer/monomer concentration constant at 7.5 wt% (Fig. 3A). The hydrogels were strained to failure at room temperature (20–22 °C) while fully submerged in a water bath to prevent water evaporation and to limit potential effects of uneven water flux out of and into the gels. The bath solutions contained 5 mM Ca^{2+} and were buffered at pH 8.0, above the pK_{a2} of the phosphate sidechains. At the lowest ratio of pMOEP-MA to pAAM, 1.5 : 6.0 wt%, the Ca^{2+}-equilibrated hydrogels were soft with an initial modulus of 0.020 ± 0.004 MPa. The stress increased linearly with strain until fracture occurred at 0.054 ± 0.002 MPa and less than 150% strain (Fig. 3A). As the pMOEP-MA to pAAM ratio was increased to above 5 wt% pMOEP-MA, the initial modulus rose sharply, strain at fracture increased toward 200%, and yield-like behavior—dramatic strain softening—appeared around 20% elongation (Fig. 3A). Hydrogel toughness, as reflected in the work of extension to fracture (Fig. 3B), also increased sharply with increasing pMOEP-MA, due primarily to the increase in yield stress of the hydrogels.

Hydrogel synthesis using pMOEP-MA as a prepolymer with a high mol% of phosphate sidechains was essential to toughen the Ca^{2+}-crosslinked DN hydrogels. Other hydrogel synthesis methods failed to produce toughened hydrogels. For example, hydrogels of 7.5 wt% pMOEP-MA with no pAAM, were brittle and frequently fractured during equilibration with divalent metal ions. Hydrogels prepared with 6.5 mol% pMOEP-MA with only 40 mol% phosphate sidechains stiffened considerably with Ca^{2+}, but did not display yield-like behavior, shrank less during equilibration with Ca^{2+}, and were less tough (not shown). Hence, further DN hydrogel mechanical characterization was done with hydrogels synthesized with 6.5 wt% pMOEP-MA and 1.0 wt% pAAM/bis-AAM.

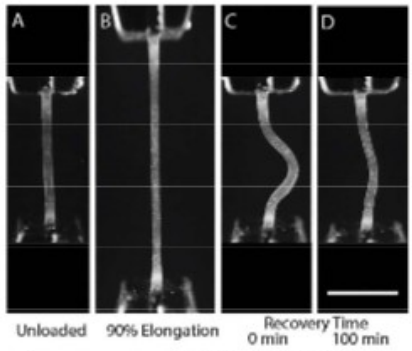

Fig. 4 Spontaneous recovery of initial length of a Ca^{2+}-hydrogel strained to 90% underwater. Scale bar = 6 mm.

Hysteresis and self-recovery kinetics of Ca^{2+}-crosslinked hydrogels during cyclical loading

The yield-like response of Ca^{2+} hydrogels was not a permanent plastic deformation. Instead, the initial length, modulus, and yield stress of hydrogels strained to 50% recover approximately 90% of their initial values within 90 min after unloading (Fig. 5 and 6). Hence, we refer to the phenomenon as pseudo-yield. The area within the forward and reverse curves of the highly hysteretic cycles represents dissipated strain energy, which also recovered to approximately 90% of the initial cycle value within 90 min. The recovery did not fit a single exponential process. In contrast, Mg^{2+} hydrogels had a linear elastic response to cyclical strains, displaying little hysteresis (Fig. 5A, green curves). Hydrogels equilibrated with Zn^{2+} were more brittle beyond the pseudo-yield point and could not be reliably strained to 50% elongation. Therefore the rate of refolding was not determined.

Strain rate dependence of Ca^{2+}-crosslinked hydrogels

The pseudo-yield stress of Ca^{2+}-equilibrated hydrogels strained to 100% at strain rates ranging over three orders of magnitude increased 5-fold (Fig. 6B). Likewise, the initial modulus, work of

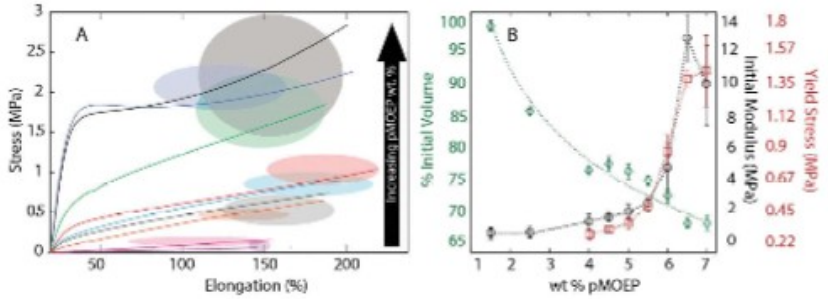

Fig. 3 Critical pMOEP concentration dependence of Ca^{2+}-hydrogel toughening. (A) Representative stress strain curves for hydrogels prepared with increasing pMOEP and decreasing pAAm concentrations. The total polymer concentration was fixed at 7.5 wt%. Ovals represent the area enclosed by ±1 s.d. of the mean stress and elongation for each hydrogel formulation ($n \geq 3$). (B) The equilibrium volume of the hydrogels declined with increasing pMOEP/pAAm wt% ratio. The initial modulus and yield stress had a non-linear dependence on pMOEP/pAAm wt% ratio. Error bars represent ±1 s.d., $n \geq 3$.

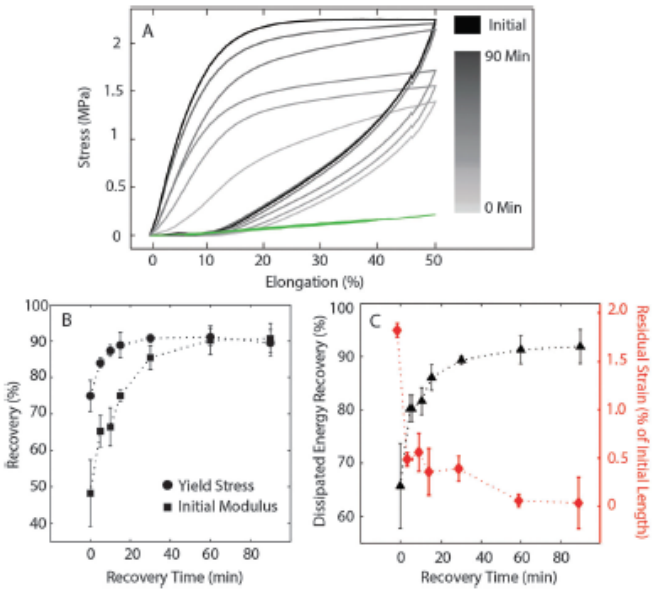

Fig. 5 Recovery kinetics of divalent metal ion-equilibrated hydrogels. (A) Representative stress strain profiles with increasing recovery periods between cycles. Grey curves: Ca^{2+}. Green curves: Mg^{2+}. (B) Time course of initial modulus and yield stress recovery. (C) Time course of hysteresis and initial length recovery. Error bars = ±1 s.d., $n \geq 3$.

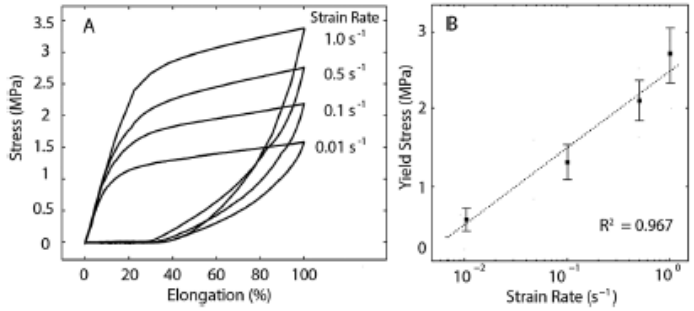

Fig. 6 Strain rate dependence of Ca^{2+}-hydrogel stress response. (A) Representative stress strain curves of cyclically loaded hydrogels. (B) Semi-log plot of yield stress as a function of strain rate. Dashed line is best linear fit. Error bars = ±1 s.d., $n \geq 3$.

extension, and dissipated energy increased by, 60%, 2-fold, and 2.3-fold, respectively (not shown). Pseudo-yield stress had a logarithmic dependence on strain rate (Fig. 6B). Strain rate had little effect on residual strain, which varied by only 5% over the range of strain rates.

Metal ion species dependence of hydrogel toughness

Hydrogels containing Na^+ counter ions were soft, linear elastomers that could be elongated about 250% before fracture (Fig. 4 and Table 1). Exchange with divalent metal ions increased the pseudo-yield stress in the following order: $Mg^{2+} < Ca^{2+} < Zn^{2+}$. Hydrogels exchanged with Mg^{2+}, like Na^+ hydrogels, were soft and displayed a linear dependence of stress on strain, whereas Ca^{2+} and Zn^{2+} hydrogels both displayed dramatic strain softening (yield-like) behavior around 20% strain. Although Zn^{2+} hydrogels fractured soon after the yield point, at strains of 40% compared to average strains of 90% for Ca^{2+} hydrogels, the work to fracture of Ca^{2+} and Zn^{2+} was nearly the same, 10.4 and 10.5 MJ m^{-3}, respectively, more than three times higher than Mg^{2+} (Table 1).

IR spectroscopy of divalent metal-ion crosslinked hydrogels

Interactions of divalent metal ions with phosphate sidechains was evaluated by IR spectroscopy (Fig. 8). Bands corresponding

to degenerate P–O$^-$ symmetric stretching modes occur between 950 and 1050 cm^{-1}. Band assignments were based on literature precedents for primary phosphate esters and pH titrations.[20,32,33] The Na^+ absorption band centered at 980 cm^{-1} corresponds to the combined absorption of two P–O$^-$ bonds of dibasic phosphate. The Na^+ absorption band centered at 980 cm^{-1} corresponds to the combined absorption of two P–O$^-$ bonds of dibasic phosphate. The 962 cm^{-1} band is not due to a phosphate vibration based on pH titrations (not shown). The 980 cm^{-1} was blue-shifted ~11, 17, and 21 cm^{-1} for Ca^{2+}, Mg^{2+}, and Zn^{2+}, respectively. The absorbance intensity of the shifted band increased in the order: $Zn^{2+} > Ca^{2+} > Mg^{2+}$.

Discussion

Caddisworm-inspired hydrogel structure and mechanics

Above a threshold concentration of phosphate sidechains on the pMOEP prepolymer, exchange of monovalent Na^+ with divalent metal ions resulted in collapse of the DN hydrogel structure, accompanied by exclusion of about 40% of its equilibrium water mass (Table 1), and a change in appearance from transparent to slightly translucent. Mechanically, the hydrogels transitioned from soft and elastic to tough and viscoelastic with non-permanent strain softening (yield) at a critical stress (Fig. 7). The synthetic method of concentrating the phosphate groups on a prepolymer as a separate, but covalently connected network within a second polyacrylamide network was critical to achieve the viscoelastic behavior and toughening effect on the hydrogels.

We interpret these observations as evidence divalent cations crosslinked the polyphosphate prepolymer network, both intra- and intermolecularly, through the phosphate sidechains into dense partially dehydrated clusters, as illustrated in Fig. 2C, that function as pseudo-domains. The collapsed phosphate prepolymer clusters are connected to one another through the elastic polyacrylamide network. The toughening effect—the extra work required to fracture the Ca^{2+} equilibrated hydrogels *versus* the Na^+ equilibrated hydrogels—was due to energy absorbed and dissipated by rupture and unfolding of the Ca^{2+} phosphate crosslinked clusters. The dense clusters functioned as a series of sacrificial yield domains undergoing sequential, viscous unfolding and extension in the stress plateau region. Rupture of the Ca^{2+} phosphate crosslinked clusters was reversible, which allowed the domain-like regions to slowly reform when unloaded, guided by the memory of the elastic polyacrylamide network. About 90% of the capacity to dissipate strain energy at moderate strain rates was recovered within 90 min. The less than complete recovery suggested some permanent damage occurred during the first strain cycle. The fatigue resistance of the hydrogels has yet to be thoroughly characterized.

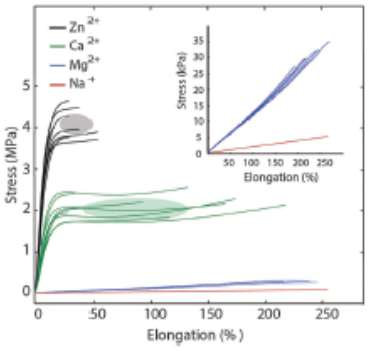

Fig. 7 Stress response during strain to fracture for hydrogels equilibrated with Na^+, Mg^{2+}, Ca^{2+}, and Zn^{2+}. Ellipses represent the mean ±1 s.d. Inset: Expanded scale to accent Mg^{2+} and Na^+ hydrogel stress response.

Modulating hydrogel strength and toughness with divalent metal ions

The stress response of the caddis silk-mimetic hydrogels can be tuned to some extent by multivalent metal ion selection, as one means to design hydrogels to meet the specifications of a particular application. Details of the metal ion interactions with the phosphate sidechains are not known, but several observations are worth noting. According to the HSAB classification scheme, Mg^{2+} and Ca^{2+} are hard acids, Zn^{2+} is intermediate, and dibasic phosphate is a hard base.[34] The interaction between non-polarizable hard acids and hard bases is predominantly ionic in character. Therefore, the divalent metal ion–phosphate complexes in the DN hydrogels may be more electrostatic in character, as opposed to charge transfer complexes. Exchange of Na^+ with Mg^{2+} caused dehydration and deswelling of the hydrogels to similar extents as Ca^{2+} and Zn^{2+}, although deswelling was fastest in Mg^{2+} (Fig. 2). The interaction of Mg^{2+} with phosphate sidechains was likewise evident in the blue-shift of absorption bands corresponding to the P–O$^-$ symmetric stretching modes in the IR spectra (Fig. 8). Despite evidence of phosphate Mg^{2+} coordination complexes, the complexes did not function as load bearing crosslinks in the hydrogels since there was comparatively little stiffening of the Mg^{2+} equilibrated hydrogels compared to Ca^{2+} and Zn^{2+} hydrogels (Fig. 7). Significantly, the weak mechanical effect of Mg^{2+} phosphate complexation, despite similar dehydration and volume change, rules out that the increased stiffness, strength, pseudo-plastic yield, viscoelasticity, and hysteresis of hydrogels equilibrated with Ca^{2+} and Zn^{2+} was due to more extensive dehydration and deswelling.

The preferred coordination geometry of Mg^{2+} is octahedral both in water and when bound by proteins or nucleic acids. In water, the coordination geometry is satisfied with six inner sphere water molecule ligands. Perturbing this rigid coordination geometry is energetically costly.[35] Proteins and nucleic acids bind Mg^{2+} ions differently; protein sidechain ligands bind Mg^{2+} directly (inner sphere mode), while nucleic acids bind Mg^{2+} indirectly through the hydration shell (outer sphere mode). Protein Mg^{2+} binding sites are usually buried in the protein interior where the low dielectric constant makes ligand exchange between inner sphere waters and anionic sidechains more energetically favorable.[36] All protein Mg^{2+}-binding sites retain at least one, and on average 2.2 inner sphere H_2O molecules in the Mg^{2+} binding site.[37] In nucleic acids, on the other hand, Mg^{2+} ions are usually

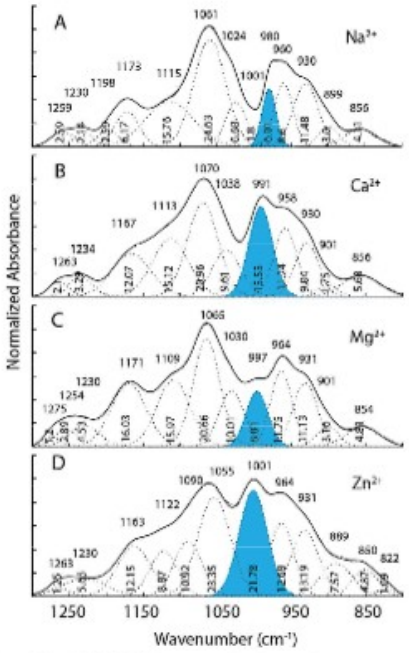

Fig. 8 Normalized ATR-FTIR spectra in the region corresponding to P–O⁻ vibrational modes of metal ion equilibrated hydrogels at pH 8.0 (blue shaded peaks). (A) Na^+-equilibrated hydrogels. (B) Ca^{2+}-equilibrated hydrogels. (C) Mg^{2+}-equilibrated hydrogels. (D) Zn^{2+}-equilibrated hydrogels. The vertical numbers are the area of the fit peak (dotted spectra) in normalized absorption units.

complexed by outer sphere phosphate oxygens leaving the octahedral hydration shell intact, or mostly intact.[38] For example, of the four octahedral Mg^{2+} ions that stabilize tRNA tertiary structure, one is bound as $Mg(H_2O)_6^{2+}$, two as $Mg(H_2O)_5^{2+}$, and one as $Mg(H_2O)_4^{2+}$, with zero, one, and two direct inner sphere phosphate oxygen coordinate bonds, respectively.[39] The weak effect of Mg^{2+} on pMOEP/pAMM hydrogel mechanics may be due to indirect coordination of $Mg(H_2O)_6^{2+}$ ions as outer sphere ligands by phosphate sidechains, or as a mix of outer and inner shell ligands with only partial exchange of inner shell water molecules, as observed in tRNAs. Although the blue shift of the P–O⁻ symmetric stretching mode band suggests at least some direct inner sphere coordination between Mg^{2+} and phosphates, the predominantly outer sphere nature of the phosphate–Mg^{2+} complexes may be too weak or too dynamic to form load bearing intra- or inter-chain crosslinks.

The greater stiffness and strength of the Ca^{2+} and Zn^{2+} hydrogels may be due to a greater propensity for their hydration shells to be displaced by inner sphere phosphate oxygen bonds, which may result in effectively stronger, load bearing, inter- and intra-chain crosslinks. The coordination numbers and geometries of Ca^{2+} and Zn^{2+} are more flexible than Mg^{2+}, and there are smaller energy barriers for transitions between coordination number and geometry.[37] In protein binding sites, Ca^{2+} ions mostly have 6 or 7 inner sphere oxygen ligands, and on average only 1.5 H_2O ligands.[40] Protein bound Zn^{2+} ions have a coordination number of six when coordinated by oxygen ligands, as is the case in the pMOEP/pAAM hydrogels. The radii, 0.74–1.04 Å and 0.71–1.03 Å, respectively, and therefore charge densities of Zn^{2+} and Mg^{2+} ions are similar.[44] The higher charge densities of Zn^{2+} and Mg^{2+} produce a blue shift of similar magnitude, relative to Na^+, in the P–O⁻ symmetric stretching mode (Fig. 8). Divalent Ca^{2+} ions, which have a radius of 1.14–1.48 Å and lower charge density than Zn^{2+} and Mg^{2+}, produce a smaller blue shift relative to Na^+ ions. Although their respective absorption coefficients are not known, the higher absorption intensity in the Zn^{2+} band compared to Mg^{2+} may be evidence that Zn^{2+} forms more inner sphere bonds with phosphate oxygens than Mg^{2+}, which may account for its much greater effect on hydrogel mechanical properties. The higher strength and stiffness of Zn^{2+} hydrogels compared to Ca^{2+} hydrogels may be due to stronger phosphate crosslinks, which in turn may be due to higher coordinate bond strengths, or the geometry of the complexes, or the number of complexes. The contribution, if any, of the higher Zn to P ratio compared to Ca and Mg is unknown and requires further investigation. The similar work of extension to failure, or toughness, of the Ca^{2+} and Zn^{2+} hydrogels is difficult to explain and may be coincidental.

Comparisons to other DN hydrogels, natural and synthetic

Several aspects of the mechanical response of natural silk fibers to controlled strains, including pseudo-yield behavior, logarithmic strain rate dependence, and self-recovery,[20] were qualitatively reproduced in the caddisworm silk mimetic DN hydrogels. The initial stiffness and work of extension to failure (toughness) fell well short of the natural fibers (Table 1, Fig. 9k). Much of the toughness of natural caddisfly silk is due to strain stiffening beyond the stress plateau region, where presumably the viscoelastic yield domains have been mostly unfolded.[19] In future work, design efforts will be directed, in part, toward increasing the stiffness and strength of the elastic network to further improve toughness of the synthetic DN hydrogels. The hydrogel toughening effect required high concentrations of phosphate sidechains compared to the natural fibers. The greater stiffness, yield stress, and fatigue resistance of the natural fibers with lower densities of Ca^{2+}–phosphate crossbridges may result from greater cooperativity in the strain dependent unfolding and refolding of the highly organized Ca^{2+}–phosphate β-domains compared to the random, less organized Ca^{2+}–phosphate pseudo-domains in the synthetic hydrogels.[20,21,41] Another factor may be the effective dielectric constant in the vicinity of the metal ion–phosphate bonds. The precise folding of β-domains in the natural fibers may exclude water from the local environment of the Ca^{2+}–phosphate complexes more effectively than the random collapse of the polyphosphate chains in the hydrogels. If so, the dielectric constant would be lower and the strength of the Ca^{2+} ion–phosphate bonds higher in the natural fibers than in the hydrogels.

The strength and toughness of the first generation caddisworm silk inspired hydrogels compare favorably with other reported synthetic DN hydrogels (Fig. 9). The initial modulus of Ca^{2+}

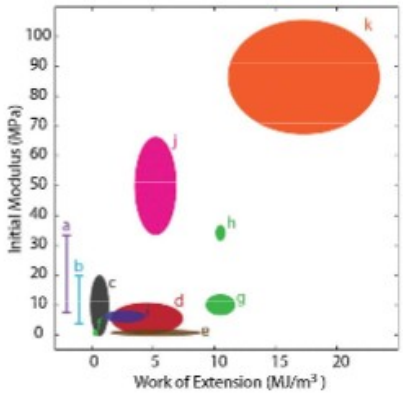

Fig. 9 Initial modulus *versus* toughness for several categories of hydrated materials. Ovals represent the area enclosed by ±1 s.d. of the initial modulus and work of extension to fracture. (a) dipole–dipole,[10] (b) PEG/pAAm,[6] (c) ionic triblock copolymers,[13] (d) polyampholytes,[11] (e) highly extensible hydrogels,[7,9,14] (f) Mg^{2+}-pMOEP/pAAm, this report, (g) Ca^{2+}-pMOEP/pAAm, this report, (h) Zn^{2+}-pMOEP/pAAm, this report, (i) articular cartilage,[42] (j) meniscus,[42] (k) caddisworm silk.[19]

hydrogels was in the same range as previous DN hydrogels, while Zn^{2+} hydrogels were considerably stiffer. Both Ca^{2+} and Zn^{2+} hydrogels were tougher than all other synthetic DN hydrogels, primarily because of greater stiffness rather than extreme extensibility. Synthetic hydrogels that achieve high toughness primarily through being highly extensible are not suitable as mechanical replacements for soft structural tissues, which do not operate under such extreme strains. Over three decades of strain rate, the initial stiffness and yield stress increased five-fold for the Ca^{2+} equilibrated pMOEP/pAAM hydrogels, and strain cycle energy dissipation (hysteresis) more than doubled (Fig. 6). Comparison of strain rate dependence of caddis silk-inspired DN hydrogels to earlier DN hydrogel architectures is difficult because strain rate dependence has rarely been reported. Strain rate dependence is a critical feature of viscoelastic hydrogels because the utility of a material will be limited to applications were the mechanical response is appropriate for the expected strain rates. At very low strain rates, below the relaxation time of the viscous yield domains, the toughening mechanism becomes irrelevant; the stress response of the hydrogels will correspond to only the elastic network component. Under sudden sustained loads, the stress will relax to the load supported by extension of the elastic network only. Finally, the mimetic hydrogels are tougher than articular cartilage and the fibrocartilage meniscus when compared to reported values of tissues that were loaded in tension (Fig. 9i and j).[42] The materials were compared in tension because cartilage and menisci loaded in unconfined compression experience radial tensile forces.

Conclusions

Using a greatly simplified polyphosphate analog of H-fibroin as a prepolymer network with dynamic phosphate metal ion crosslinks within an extensible polyacrylamide network a DN network hydrogel architecture was created that qualitatively replicated the mechanical properties of natural caddisworm silk, including high stiffness, pseudo-yield behavior, logarithmic strain rate dependence, high strain cycle hysteresis, and self-recovery. It was possible to replicate the mechanical properties by copying only relatively simple and synthetically accessible structural features of the natural fiber. We are confident that as further details of the natural caddisworm silk fiber architecture and metal phosphate chemistry are determined, the design of synthetic hydrogels can be improved to bring their toughness closer to the natural fibers. Beyond their potential utility as prosthetic biomaterials, the caddisworm mimetic hydrogels provide a simplified, inexpensive, and convenient model system to test hypotheses concerning the relationship between chemistry, structure, and mechanical properties of natural silk fibers.

Acknowledgements

This work was supported by the Army Research Office, award #W911NF1310319. We thank Nic Ashton for helpful discussions and Monika Sima for help with SEC.

References

1 A. C. T. Vrancken, P. Buma and T. G. van Tienen, *Int. Orthop.*, 2012, **37**, 291–299.
2 M. A. Haque, T. Kurokawa and J. P. Gong, *Polymer*, 2012, **53**, 1805–1822.
3 S. Naficy, H. R. Brown, J. M. Razal, G. M. Spinks and P. G. Whitten, *Aust. J. Chem.*, 2011, **64**, 1007.
4 X. Zhao, *Soft Matter*, 2014, **10**, 672–687.
5 R. Long, K. Mayumi, C. Creton, T. Narita and C.-Y. Hui, *Macromolecules*, 2014, **47**, 7243–7250.
6 J. P. Gong, Y. Katsuyama, T. Kurokawa and Y. Osada, *Adv. Mater.*, 2003, **15**, 1155–1158.
7 Q. Chen, L. Zhu, C. Zhao, Q. Wang and J. Zheng, *Adv. Mater.*, 2013, **25**, 4171–4176.
8 D. Myung, W. Koh, J. Ko, Y. Hu, M. Carrasco, J. Noolandi, C. N. Ta and C. W. Frank, *Polymer*, 2007, **48**, 5376–5387.
9 M. A. Haque, T. Kurokawa, G. Kamita and J. P. Gong, *Macromolecules*, 2011, **44**, 8916–8924.
10 Y. Han, T. Bai, Y. Liu, X. Zhai and W. Liu, *Macromol. Rapid Commun.*, 2011, **33**, 225–231.
11 T. L. Sun, T. Kurokawa, S. Kuroda, A. Bin Ihsan, T. Akasaki, K. Sato, M. A. Haque, T. Nakajima and J. P. Gong, *Nat. Mater.*, 2013, **12**, 932–937.
12 F. R. Kersey, D. M. Loveless and S. L. Craig, *J. R. Soc., Interface*, 2006, **4**, 373–380.
13 K. J. Henderson, T. C. Zhou, K. J. Otim and K. R. Shull, *Macromolecules*, 2010, **43**, 6193–6201.
14 J.-Y. Sun, X. Zhao, W. R. K. Illeperuma, O. Chaudhuri, K. H. Oh, D. J. Mooney, J. J. Vlassak and Z. Suo, *Nature*, 2012, **489**, 133–136.
15 W.-C. Lin, W. Fan, A. Marcellan, D. Hourdet and C. Creton, *Macromolecules*, 2010, **43**, 2554–2563.

16 S. Rose, A. Dizeux, T. Narita, D. Hourdet and A. Marcellan, *Macromolecules*, 2013, **46**, 4095–4104.
17 X. Qin, F. Zhao, Y. Liu, H. Wang and S. Feng, *Colloid Polym. Sci.*, 2009, **287**, 621–625.
18 T. Sakai, T. Matsunaga, Y. Yamamoto, C. Ito, R. Yoshida, S. Suzuki, N. Sasaki, M. Shibayama and U.-I. Chung, *Macromolecules*, 2008, **41**, 5379–5384.
19 N. N. Ashton, D. R. Roe, R. B. Weiss, T. E. Cheatham and R. J. Stewart, *Biomacromolecules*, 2013, **14**, 3668–3681.
20 N. N. Ashton and R. J. Stewart, *Soft Matter*, 2015, **11**, 1667–1676.
21 R. Stewart and C. Wang, *Biomacromolecules*, 2010, **11**, 969–974.
22 C.-S. Wang, N. N. Ashton, R. B. Weiss and R. J. Stewart, *Insect Biochem. Mol. Biol.*, 2014, **54**, 69–79.
23 N. Yonemura, K. Mita, T. Tamura and F. Sehnal, *J. Mol. Evol.*, 2009, **68**, 641–653.
24 F. Sehnal and M. Zurovec, *Biomacromolecules*, 2004, **5**, 666–674.
25 E. Degtyar, M. J. Harrington, Y. Politi and P. Fratzl, *Angew. Chem., Int. Ed.*, 2014, **53**, 12026–12044.
26 M. J. Harrington and J. H. Waite, *J. Exp. Biol.*, 2007, **210**, 4307–4318.
27 M. Harrington, A. Masic, N. Holten-Andersen, J. Waite and P. Fratzl, *Science*, 2010, **328**, 216.
28 N. Holten-Andersen, A. Jaishankar, M. J. Harrington, D. E. Fullenkamp, G. DiMarco, L. He, G. H. McKinley, P. B. Messersmith and K. Y. C. Lee, *J. Mater. Chem. B*, 2014, **2**, 2467–2472.
29 N. Yonemura, F. Sehnal, K. Mita and T. Tamura, *Biomacromolecules*, 2006, **7**, 3370–3378.
30 K. Ohkawa, Y. Miura, T. Nomura, R. Arai, K. Abe, M. Tsukada and K. Hirabayashi, *Biofouling*, 2013, **29**, 357–367.
31 H. Shao, G. M. Weerasekare and R. J. Stewart, *J. Biomed. Mater. Res.*, 2011, **97A**, 46–51.
32 J. Sanchez-Ruiz and M. Martinez-Carrion, *Biochemistry*, 1988, **27**, 3338–3342.
33 C. Fernández, S. F. Ausar, R. G. Badini, L. F. Castagna, I. D. Bianco and D. M. Beltramo, *Int. Dairy J.*, 2003, **13**, 897–901.
34 R. G. Pearson, *J. Am. Chem. Soc.*, 1963, **85**, 3533–3539.
35 C. W. Bock, A. Kaufman and J. P. Glusker, *Inorg. Chem.*, 1994, **33**, 419–427.
36 T. Dudev and C. Lim, *Chem. Rev.*, 2003, **103**, 773–788.
37 A. K. Katz, J. P. Glusker and S. A. Beebe, *J. Am. Chem. Soc.*, 1996, **118**, 5752–5763.
38 H. Robinson, Y. G. Gao, R. Sanishvili, A. Joachimiak and A. H. Wang, *Nucleic Acids Res.*, 2000, **28**, 1760–1766.
39 S. R. Holbrook, J. L. Sussman, R. W. Warrant, G. M. Church and S.-H. Kim, *Nucleic Acids Res.*, 1977, **4**, 2811–2820.
40 J. P. Glusker, A. K. Katz and C. W. Bock, *Rigaku J.*, 1999, **16**, 8–16.
41 S. Keten, Z. Xu, B. Ihle and M. J. Buehler, *Nat. Mater.*, 2010, **9**, 359–367.
42 E. K. Danso, J. T. J. Honkanen, S. Saarakkala and R. K. Korhonen, *J. Biomech.*, 2014, **47**, 200–206.
43 B. Stuart, *Infrared Spectroscopy: Fundamentals and Applications*, John Wiley & Sons, Hoboken, NJ, 2004.
44 F. A. Cotton, G. Wilkinson, C. A. Murillo and M. Bochmann, *Advanced Inorganic Chemistry*, John Wiley & Sons, New York, NY, 1999.

CHAPTER 3

SUSTAINED TOBRAMYCIN RELEASE FROM POLYPHOSPHATE DOUBLE NETWORK HYDROGELS

Authors Contributions: D.D.L. prepared and synthesized the monomers and polymers and hyrogels. Determination of tobramycin release assays was done by D.D.L. and A.K.F. Microbiology assays were done at the Bone Joint Research Lab by D.D.L. and S.G. under the direction of D.L.W. The design of experiments and interpretation of results was done by D.D.L., D.L.W. and R.J.S. D.D.L. and R.J.S. prepared the manuscript with methods input and proofreading from D.L.W.

Acta Biomaterialia 50 (2017) 484–492

Contents lists available at ScienceDirect

Acta Biomaterialia

journal homepage: www.elsevier.com/locate/actabiomat

Full length article

Sustained tobramycin release from polyphosphate double network hydrogels

Dwight D. Lane [a], Amber K. Fessler [a], Seungah Goo [b,c], Dustin L. Williams [b,c,d], Russell J. Stewart [a,*]

[a] Department of Bioengineering, University of Utah, 20 S. 2030 East, Salt Lake City, UT 84112, USA
[b] George E. Wahlen Department of Veterans Affairs, Bone and Joint Research Lab, 500 Foothill Dr. (151F), Salt Lake City, UT 84148, USA
[c] Department of Orthopaedics, University of Utah, Salt Lake City, UT, USA
[d] Department of Pathology, University of Utah, Salt Lake City, UT, USA

ARTICLE INFO

Article history:
Received 29 August 2016
Received in revised form 7 December 2016
Accepted 13 December 2016
Available online 18 December 2016

Keywords:
Double network hydrogel
Aminoglycoside
Tobramycin
Local drug delivery
Sustained release
Polyelectrolyte
Biofilm
Pseudomonas aeruginosa

ABSTRACT

Sustained local delivery of antibiotics from a drug reservoir to treat or prevent bacterial infections can avoid many of the drawbacks of systemic administration of antibiotics. Prolonged local release of high concentrations of antibiotics may also be more effective at treating bacteria in established biofilm populations that are resistant to systemic antibiotics. A double network hydrogel comprising an organic polyphosphate pre-polymer network polymerized within a polyacrylamide network de-swelled to about 50% of its initial volume when the polyphosphate network was crosslinked with polycationic tobramycin, an aminoglycoside antibiotic. The antibiotic-loaded hydrogels contained approximately 200 mg/ml of tobramycin. The hydrogels continuously released daily amounts of tobramycin above the *Pseudomonas aeruginosa* minimal bactericidal concentration for greater than 50 days, over the pH range 6.0–8.0, and completely eradicated established *P. aeruginosa* biofilms within 72 h in a flow cell bioreactor. The presence of physiological concentrations of Mg^{2+} and Ca^{2+} ions doubled the cumulative release over 60 days. The polyphosphate hydrogels show promise as materials for sustained localized tobramycin delivery to prevent post-operative *P. aeruginosa* infections including infections established in biofilms.

Statement of Significance

Polyphosphate hydrogels were loaded with high concentrations of tobramycin. The hydrogels provided sustained release of bactericidal concentrations of tobramycin for 50 days, and were capable of completely eradicating *P. aeruginosa* in established biofilms. The hydrogels have potential for localized prevention or treatment of *P. aeruginosa* infections.

1. Introduction

Infection prevention or eradication is a pivotal concern in management of chronic or deep wounds, at surgical sites, and in invasive medical procedures [1–4]. This is especially true at the surfaces of indwelling medical devices, such as catheters, vascular grafts, orthopedic fixtures, periodontal implants, wound dressings, and contact lenses. Bacteria preferentially adhere to and colonize biomaterial and medical device surfaces, often leading to the formation of biofilms [5]. Biofilms are communities of bacteria with exopolysaccharide matrices secreted by adhered bacterial cells that increase their antibiotic resistance by up to 1000 fold [6–8]. Some resistance may stem from frustrated penetration of antibiotic into the biofilm, as in the case of positively charged aminoglycosides that absorb to negatively charged biofilm components [9,10]. Additionally, nutrient depletion across the biofilm induces a transition to anaerobic metabolism with far less susceptibility to aminoglycosides [11]. Along with these growth state changes it is known that some subset of the population (~1%) will experience a phenotypic change resulting in increased resistance to antibiotics. It is thought that these "persister" cells reseed the colony following antibiotic regimens [12,13]. As a result, infections in chronic wounds or on medical device surfaces may require hospital readmission, long courses of high-dose antibiotics, and revision surgeries [4,14,15]. All of this culminates in patient discomfort, increased morbidity rates, and elevated health care costs [15,16]. While rates of infection are low, for example 1.2% following

* Corresponding author.
E-mail address: russell.stewart@utah.edu (R.J. Stewart).

http://dx.doi.org/10.1016/j.actbio.2016.12.030
1742-7061/

arthroplasty and 3–6% in revision surgeries [17], both the large number of procedures performed annually and an aging population drive predictions for a significant increase in procedure acquired infections [17–20]. Thus, preventing and eliminating infections remains a pressing healthcare problem.

The traditional approach to preventing and treating infections is systemic delivery of antibiotics. Adverse effects of systemic antibiotic use include organ toxicity, reduction of beneficial bacteria populations, and overgrowth of naturally resistant organisms, like Candida and *Clostridium difficile* [21]. Sustained local delivery of antibiotics from a delivery device avoids many of the pitfalls of systemic delivery [22–24]. Hydrogels have been extensively explored as vehicles for localized drug delivery due to their high water content, excellent biocompatibility, and ease of drug loading [24–26]. Passive loading and release of antibiotics from hydrogels generally does not provide for significantly prolonged release [27,28]. Numerous strategies have been devised for sustained release from hydrogels [28] that include controlling microstructure and porosity to slow diffusion [29–32], coupling release to the slow degradation of the hydrogel matrix [33], covalent conjugation to the hydrogel matrix with degradable linkers [29,33–35], environmentally triggered volume changes that modulate diffusion kinetics [31,32,36,37], and thin surface films that restrict diffusion [30,31]. Diffusion of charged molecules can also be restricted and release prolonged by electrostatic interactions with charged groups in the hydrogel matrix [38–44].

Here, we report prolonged release of tobramycin, a polycationic aminoglycoside antibiotic, from a double network polyphosphate hydrogel [45]. The hydrogel provided sustained release of tobramycin above the minimal bacteriocidal concentration (MBC) for the *P. aeruginosa* strain tested and eradicated established biofilms. The reported hydrogels show promise as materials for delivering aminoglycoside antibiotics during knee arthroplasty or revision surgery, and other indications [17,46–48].

2. Materials and methods

2.1. Materials

Phosphorus(V) oxychloride, 2-hydroxyethyl methacrylate, triethylamine, and glycidyl methacrylate were purchased from Alfa Aesar (Ward Hill, MA). Methacrylic acid, 2,2′-azobis(2-methylpropionitrile), acrylamide, *N*,*N*′-methylene-bisacrylamide, and *N*,*N*,*N*′,*N*′-tetramethylethylenediamine were purchased from Sigma Aldrich (St Louis, MO). Ammonium persulfate, FilmTracer™ LIVE/DEAD Biofilm Viability kit, Brain heart infusion (BHI) broth and cation adjusted Mueller Hinton broth (CAMHB) were purchased from Fischer Scientific (Pittsburgh, PA). Tobramycin (97%) was acquired from Acros Organics (New Jersey, USA). *P. aeruginosa* ATCC 27853 was purchased from the American Type Culture Collection (Manassas, VA). This strain was chosen because it is well-characterized and representative of pathogenic *P. aeruginosa*. *In vitro* results with ATCC 27853 have been shown to correlate with *in vivo* pathogenicity [49–52]. Columbia blood agar plates were purchased from Hardy Diagnostics (Murray, UT).

2.2. Synthesis of MOEP monomer and polyPEMA-MA copolymers

2-(Methacryloyloxy)ethyl phosphate (MOEP) was synthesized as previously described [53]. Briefly, phosphorus oxychloride (33.9 g, 220 mmol) and hydroxylethyl-methacrylamide (HEMA) were mixed at a 0.7:1 M ratio in dry toluene (480 mL) under argon. The reaction was stirred at 4 °C while triethylamine (TEA) (77 mL) was added in three increments over 10 m. Following addition of TEA, the reaction was stirred at 22 °C for 6 h under argon, then filtered to remove precipitated salt. The reaction was cooled to 4 °C before the addition of deionized water (480 mL), then stirred under argon at 22 °C for 12 h. The reaction was extracted twice with diethyl ether (100 mL) and the organic layers were discarded. The aqueous layer was extracted using tetrahydrofuran (THF) and diethyl ether (1:2, 12 × 225 mL), then dried over anhydrous sodium sulfate before evaporating the solvent. The monomer structure was verified by ^{1}H and ^{31}P NMR (Fig. S1A and B).

Poly(phosphoethyl-methacrylate-co-acrylic acid) (pPEMA-AA) was synthesized by free radical polymerization of MOEP (85 mol %), and methacrylic acid (15 mol%) in methanol (12.5 mL mg^{-1} MOEP). MOEP and methacrylic acid were degassed by bubbling with argon for 1 h, followed by addition of azo-bis-isobutyronitrile (AIBN, 4.5 mol%) at 55 °C to initiate polymerization. The reaction was stirred for 15 h before precipitation with acetone, then dissolved in water (200 mL H_2O per 17 g pPEMA-AA). Subsequently, methacrylate groups (MA) were grafted onto the methacrylic acid sidechains with glycidyl methacrylate in 9-fold molar excess relative to the carboxylate sidechains. The methacrylated pPEMA-AA (pPEMA-MA) was adjusted to pH 7.3 with NaOH and purified by tangential flow filtration using a Millipore Pellicon 3 cassette filter with an Ultracel 10 kD membrane. The polymer product was lyophilized, and stored at −20 °C.

The molecular weight (Mw) and polydispersity index (PDI) of pPEMA65-MA23 were determined by size exclusion chromatography (SEC) on an Agilent Infinity 1260 HPLC system with a PL-Aquagel-OH Mixed-M column (8 μm, 300×7.5 mm) column. The column buffer was 0.1 M $NaNO_3$/0.01 M NaH_2PO_4, pH 8.0 with a flow rate of 1 mL m^{-1}. The average M_m and PDI, 46 kg mol^{-1} and 1.67, respectively, were estimated using sodium polymethacrylic acid standards. The structure and composition of the polymers were verified by ^{1}H and ^{31}P NMR (Fig. S1C). The phosphate prepolymer contained 65 mol% phosphate sidechains, 12 mol% HEMA, and 23 mol% MA sidechains. The copolymers are referred to as pPEMA65-MA23 to indicate the mol% phosphate and methacrylate sidechains.

2.3. Hydrogel synthesis: copolymerization of polyPEMA65-MA23 and acrylamide

Hydrogels were formed by free radical polymerization of the pPEMA65-MA23 prepolymer with acrylamide (Aam) and N,N-methylenebisacrylamide (bis-Aam), a bifunctional crosslinker, in 150 mM NaCl (Fig. 1A and B). The wt% of pPEMA65-MA23 and Aam/bis-Aam were 6.5% and 1.0%, respectively. The molar ratio of Aam to bis-Aam was 60:1. Polymerization was initiated by adding 10% ammonium persulfate (APS) and tetramethylethylenediamine (TEMED) to final concentrations of 70 μg ml^{-1} and 2.4 μl ml^{-1}, respectively. Following addition of APS and TEMED, 250 μl aliquots were placed in wells of a 48 well plate with 200 μl of 2-propanol floated on top to limit oxygen exposure. After 90 m, polymerized hydrogel disks were removed and soaked in 150 mM NaCl for 24 h to remove unreacted reagents.

2.4. Hydrogel loading and measurement of tobramycin concentrations

Uniform 250 μl hydrogel disks were immersed in 2 M NaCl and 5 mM tobramycin adjusted to pH 7.7 with HCl for 8 h. The salt concentration was then diluted to 150 mM NaCl while maintaining the 5 mM tobramycin concentration at pH 7.7 for a total of 24 h (Fig. 1C). Initial loading in 2 M NaCl prevented cracks and defects in the hydrogels caused by rapid deswelling. Time lapse videos of hydrogel deswelling during tobramycin loading were analyzed in Image J to measure hydrogel diameters. Isotropic shrinking was assumed to calculate volume changes from the diameter.

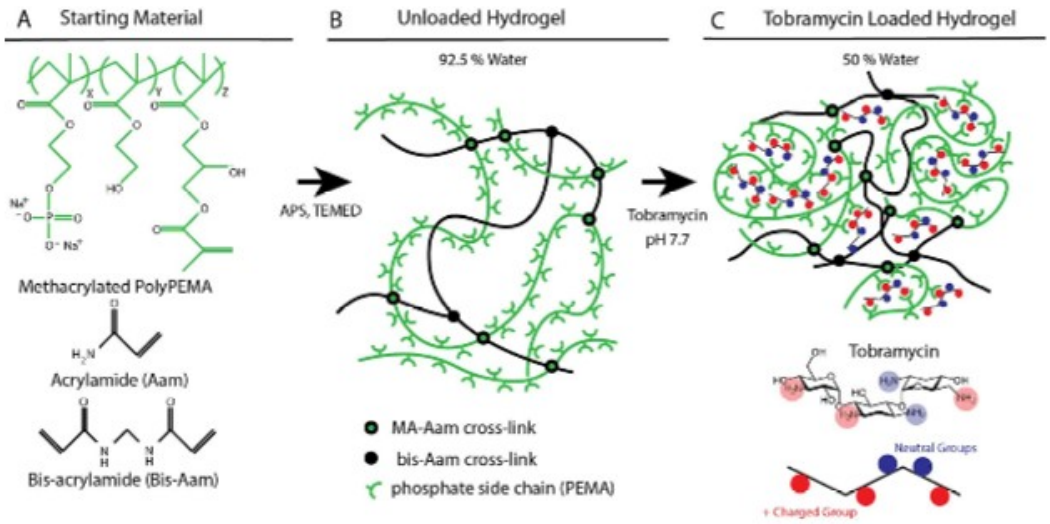

Fig. 1. Schematic diagram of the synthesis and loading of pPEMA-pAAm tobramycin double network hydrogels: (A) Structure of pPEMA-MA. (B) Double network structure after polymerization of acrylamide network. (C) Collapse of the polyphosphate network and expulsion of water due to electrostatic crosslinking of phosphates by tobramycin.

Total tobramycin concentrations in the hydrogels was determined by two methods: i.) gravimetrically by subtracting the average dry weight of unloaded hydrogels from the average dry weight of tobramycin equilibrated gels, ii.) by depletion of tobramycin in the loading solution. Tobramycin concentrations were measured colorimetrically using a Pyrogallol Red-Molybdate (PMR) assay for primary amines [54–56]. A PMR solution was prepared by mixing 0.4 mL of 1.2 mg/mL pyrogallol red in methanol, 9 mL of a solution of 55 mM succuinic acid and 4 mM sodium benzoate, and 0.04 mL each of 12 mM disodium molybdate and 261 mM sodium oxalate. Tobramycin containing samples (0.2 mL) were added to 0.8 ml of the PRM solution. After 45 m at 22 °C absorbance at 600 nm was measured in a Spectra Max M2 plate reader and compared to tobramycin standards.

2.5. Determination of release kinetics from tobramycin hydrogels

Three tobramycin loaded hydrogels disks for each time point were submerged in 2 mL of either 150 mM NaCl or 130 mM NaCl, plus 1.5 mM Mg^{2+} and 2.5 mM Ca^{2+} at pH 7.3 to approximate physiological ionic strength and the presence or absence of physiological concentrations of divalent metal ions [57]. The 2 mL solutions were replaced with fresh 2 ml solutions after 1, 2, 4, 12, and 24 h on day one, then every 24 h thereafter. The 2 mL volume was ~15 times greater than the volume of the loaded hydrogel (~140 μl). The tobramycin concentration in the solutions was determined using the PRM colorimetric assay. The effect of pH on tobramycin release kinetics was determined by incubating the hydrogel disks in solutions of 150 mM NaCl buffered with 5 mM 2-(N-morpholino)ethanesulfonic acid (MES) at pH 6 and 6.5, and with 5 mM 4-(2-hydroxyethyl)-1-piperazineethanesulfonic acid (HEPES) at pH 7, 7.5, and 8.

2.6. Measuring zones of inhibition (ZOI) against P. aeruginosa

Columbia blood agar plates were used to determine ZOIs. To do so, *P. aeruginosa* cultures were re-suspended and agar inoculated following protocols of the Manual of Antimicrobial Susceptibility Testing and Clinical Laboratory and Standards Institute (CLSI) M02-A12. Briefly, a 0.5 McFarland standard culture, approximately 1×10^8 CFUs mL^{-1}, was resuspended. A sterile cotton swab was dipped into the solution and aseptically swabbed in three directions over the agar plate surface to create a lawn of bacteria. Subsequently, one tobramycin loaded gel was placed in the center of each plate and left for 24 h at 37 °C. After 24 h the plates were photographed and the diameter of the ZOIs were measured using Image J software. The hydrogels were transferred same side down onto new plates. ZOI measurements were taken as described every 24 h until the ZOI decreased to zero.

2.7. Determining minimum inhibitory concentration (MIC) and minimum bactericidal concentration (MBC)

The MIC of the *P. aeruginosa* ATCC 27853 isolate used in this study was determined following a modified protocol of the Clinical and Laboratory Standards Institute (CLSI) guideline M07. Using a fresh overnight culture of bacteria grown in CAMHB, a 0.5 McFarland standard culture was made in phosphate buffered saline (PBS) using a nephelometer. The culture was diluted 1:100 in PBS to achieve a bacteria concentration of approximately 5×10^6 - CFU mL^{-1}. A tobramycin solution in CAMHB was serially diluted 1:2 with CAMHB in the wells of a 96 well plate to achieve final cultures with tobramycin concentrations ranging from 64 to 0.125 μg mL^{-1}. 50 μL of the diluted culture were added to each well to a final volume of 100 μL, the solutions were mixed, the plate was covered with adhesive film, and incubated 24 h at 37 °C. The negative growth control contained tobramycin only without bacteria. The positive growth control contained bacteria without antibiotic. The lowest concentration of tobramycin that inhibited growth, the MIC, was 0.5 μg mL^{-1}. The MBC was determined in conjunction with MIC testing by following the CLSI M26-A standard [58]. The cultures in wells with tobramycin concentrations above the MIC were plated in a 10-fold dilution series to quantify CFUs. The concentration of antibiotic that resulted in a 3 $\log_{10}$ reduction in CFUs was defined as the MBC. The MBC for tobramycin for *P. aeruginosa* ATCC 27853 was 2 mg mL^{-1}.

2.8. Testing tobramycin loaded hydrogels against P. aeruginosa biofilms

P. aeruginosa ATCC 27853 biofilms were grown using a biofilm reactor from Biosurface Technologies (Bozeman, MT) following published methods [59,60]. To set up the system, stainless steel (316L) coupons were loaded into reactor holders. The reactor was assembled, rinsed with deionized water, then autoclaved. Five hundred mL of BHI broth were aseptically poured into the reactor and an additional 1 mL of a 0.5 McFarland standard was added to the 500 mL of BHI resulting in $\sim 2 \times 10^5$ CFU mL^{-1}. The reactor was placed on a hot/stir plate set at 34 °C and 130 rpm. Bacteria were allowed to grow and establish a biofilm in batch phase for 24 h. A solution of 10% BHI was then flowed through the reactor at a rate of 7.0 mL m^{-1} for an additional 48 h, following which the coupons were aseptically removed and used for analysis.

2.8.1. Biofilm exposure to tobramycin-loaded gels in a biomimetic flow cell

To test the efficacy of the loaded hydrogels against biofilms, a custom flow cell was used to mimic an *in vivo* environment [61,62]. Tobramycin loaded hydrogels were placed on both sides of biofilm-covered stainless steel coupons (total surface area = 400 mm^2) and placed inside polystyrene cage. Cages were fashioned by cutting individual wells from a 24 well plate and drilling holes in the sides and bottom. The coupon containing cages were placed into flow cell chambers that contained 20 mL BHI. Fresh 10% BHI broth was flowed into the flow cell chambers through inlets and exited an effluent port at a flow rate of ~5 mL h^{-1} to mimic physiological fluid flow. Three coupons were removed every 24 h for up to 72 h and the CFUs per coupon was quantified. The affect of unloaded hydrogels on biofilm viability was tested in the same way.

2.8.2. Quantification of CFUs

Using standard methods [59,60], coupons were removed following treatment and placed in sterile 50 mL falcon tubes with 2 mL CAMHB and vortexed for 1 m, sonicated 10 m and then vortexed for 10 s. In a 10-fold dilution series, five 10 µL droplets were placed on agar plates and grown for 24 h at 37 °C, after which the CFUs were counted and used to calculate the CFU mm^{-2} biofilm.

2.8.3. Assessment of biofilm viability by confocal microscopy

Biofilm viability was also assessed using the FilmTracer™ live/dead biofilm viability kit and then imaging with confocal microscopy. Biofilms were fluorescently labeled using the viability kit protocols. Briefly, biofilm coated coupons were immersed for 30 m at 22 °C in 3 µl each of SYTO® 9 (green stain for live cells) and propidium iodide (red stain for dead cells) and 1 mL sterilized water. Coupons were then rinsed with sterilized water and imaged within 1 h with a Nikon A1 confocal microscope using a 10× objective and Nikon NIS-Elements acquisition software.

2.9. Statistical methods

All experiments were done with at least three independent samples. Results are reported as the mean +/− 1 standard deviation. The statistical significance of tobramycin release over time in Na^+ versus Ca^{2+}/Mg^{2+} (Fig. 4A) and versus pH (Fig. 5A) were tested by two-way repeated measures ANOVA using SPSS, version 24 (IBM). Following the two-way repeated measures ANOVA of the pH dependent release over time, the differences between the mean daily release over the first 10 days for each pH value (Fig. 5C) were evaluated for statistical significance by ANOVA followed by post hoc Tukey-HSD tests. P values less than 0.05 were considered significant.

3. Results and discussion

3.1. Tobramycin loading of pPEMA-pAAm hydrogels

The highly negatively charged pPEMA-pAAm hydrogel disks containing Na^+ counterions collapsed rapidly when equilibrated in a 5 mM solution of tobramycin in 150 mM NaCl (pH 7.7). At pH 7.7, each tobramycin molecule on average contained 2–3 ionized primary amine groups (Fig. 1) [63]. At physiological ionic strength the volume collapse as tobramycin crosslinked phosphate sidechains was so rapid and energetic that the de-swelled hydrogels were extensively fractured. To prevent fracture, the hydrogels were initially incubated with 5 mM tobramycin in 2 M NaCl (pH 7.7) to slow tobramycin induced deswelling. The hydrogel was then transferred to 5 mM tobramycin and 150 mM NaCl (pH 7.7). The hydrogel volumes equilibrated at ~55% of their initial volume (~140 µl) within 15 h (Fig. 2). The resulting tobramycin loaded hydrogel disks were transparent and homogeneous.

The tobramycin concentration in the pPEMA-pAAm hydrogels was determined gravimetrically after lyophilizing unloaded and tobramycin-loaded hydrogels. On average, dried unloaded hydrogels weighed 18.7 +/− 0.7 mg, while loaded hydrogels weighted 31.6 +/− 1.1 mg, which corresponds to 12.8 +/− 1.8 mg/gel, or 207 +/− 29 mg mL^{-1} of hydrogel. Tobramycin was concentrated 40-fold in the hydrogels compared to the incubation solution. To confirm the high loading capacity, tobramycin concentrations in the pPEMA-pAAm hydrogels was also determined by measuring the depletion of tobramycin in the equilibration solutions using a colorimetric assay for primary amines. At equilibrium, the tobramycin concentration in solution was 16.5 +/− 1.7 mg/ml, which corresponded to loading 13.5 +/− 3.2 mg tobramycin per hydrogel disk, or 218 +/− 52 mg tobramycin per mL of pPEMA-pAAm hydrogel. For comparison, 7.5 wt% pAAm hydrogels incubated in 5 mM tobramycin contained 8.8 +/− 2.0 mg/ml as determined gravimetrically, and 9.6 +/− 1.2 mg/ml as determined by tobramycin depletion. The pAAm hydrogels did not deswell in the tobramycin solution with 150 mM NaCl.

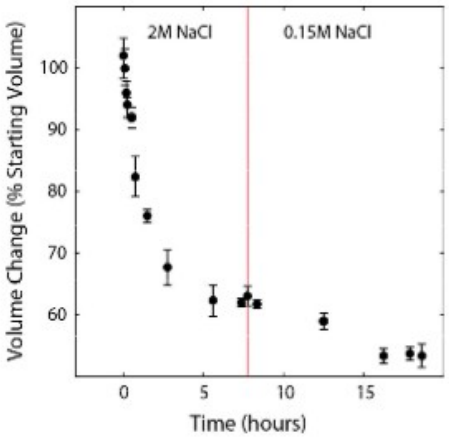

Fig. 2. Volume change of pPEMA-pAAm hydrogels following the addition of 5 mM tobramycin. The red line indicates the point at which salt concentration was decreased from 2 M to 0.15 M NaCl. Volume change is normalized to the average starting volume. n = 3, error bars are +/− 1 S.D. (For interpretation of the references to colour in this figure legend, the reader is referred to the web version of this article.)

3.2. Sustained tobramycin release

3.2.1. Tobramycin hydrogel ZOI

Sustained release was verified by placing the tobramycin-loaded pPEMA-pAAm hydrogel disks on freshly plated *P. aeruginosa* (Fig. 3A). After 24 h, the diameter of the ZOI were measured and the hydrogel disks were transferred to new *P. aeruginosa* plates. The diameter of the ZOI decreased by 17% during the first 24 h period for the tobramycin loaded pPEMA-pAAm hydrogels, after which the ZOI diameter remained constant until day 10, then declined steadily to zero by day 25 (Fig. 3B). The initial burst of tobramycin release was likely due to passive release of unbound tobramycin. As a control, the ZOIs created by 7.5 wt% pAAm hydrogel passively loaded by incubation with 5 mg/mL tobramycin were determined. The pAAm hydrogel disks did not shrink during incubation in the tobramycin solution. The diameters of the ZOI during the first 24 h period were 30% larger than the pPEMA-pAAm ZOIs and rapidly declined to zero by day 6, consistent with passive diffusion of tobramycin out of the swollen hydrogel (Fig. 3). The prolonged tobramycin release from the pPEMA-pAAm hydrogels compared to pAAm hydrogels was likely due to a combination of i.) restricted diffusion of tobramycin due to reversible electrostatic interactions with phosphate sidechains, ii.) restricted diffusion due to tobramycin crosslinking and hydrogel shrinkage, which resulted in decreased porosity of the hydrogel network, and iii.) substantially higher tobramycin concentrations in the pPEMA-pAAm hydrogels. Slow hydrolysis of the two ester linkages in the phosphate sidechains may have also contributed to the release of tobramycin by decreasing the negative charge density within the hydrogel matrix.

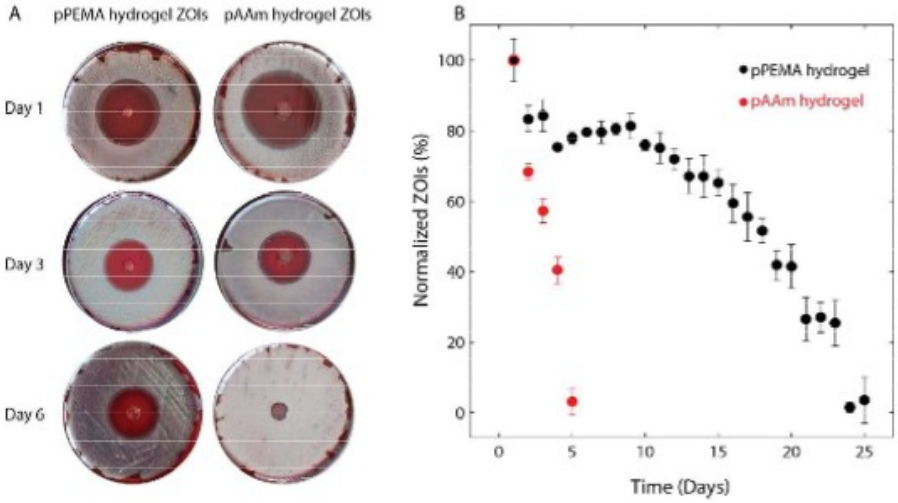

Fig. 3. (A) ZOIs created by tobramycin-loaded pPEMA-pAAM and pAAM hydrogels after six days. (B) ZOI diameters normalized to the ZOI on day 1. Black: Tobramycin-loaded pPEMA-pAAm hydrogels. Red: Tobramycin loaded pAAm gel. n = 3, error bars = +/− 1 S.D. (For interpretation of the references to colour in this figure legend, the reader is referred to the web version of this article.)

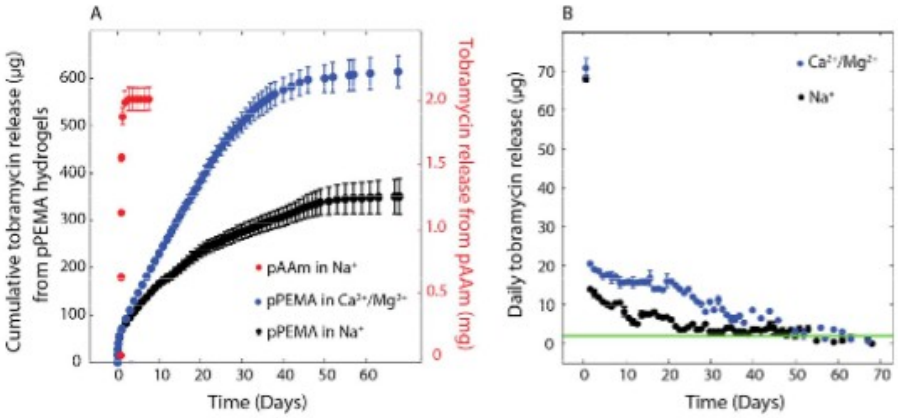

Fig. 4. Controlled release of tobramycin from pPEMA-pAAm hydrogels. (A) Cumulative release of tobramycin. Red symbols: pAAm hydrogel. Blue symbols: pPEMA-pAAm hydrogels in 150 mM NaCl plus Ca^{2+}/Mg^{2+}. Black symbols: pPEMA-pAAm hydrogels in 150 mM NaCl. By repeated measures analysis, the tobramycin release from pPEMA-pAAm hydrogels in the presence of Ca^{2+}/Mg^{2+} ions was significantly greater than in the presence of Na^{+} ($P < 0.001$). (B) Daily tobramycin release. Green Line: tobramycin MBC for *P. aeruginosa*. n = 3, Error bars = +/− 1 S.D.

3.2.2. Quantitative tobramycin release

Multivalent cations compete with tobramycin for phosphate binding sites and thereby change the release kinetics. The tobramycin release rate was therefore determined in the presence and absence of Mg^{2+} and Ca^{2+} ions, the most abundant multivalent metal ions in blood and serum [57]. Tobramycin-loaded pPEMA-pAAm hydrogel disks (250 µl volume) were incubated in 2 ml solutions of either 150 mM NaCl, or 130 mM NaCl plus 3 and 5 mM Mg^{2+} and Ca^{2+}, respectively, at pH 7.3. The solutions were changed every 24 h and the tobramycin concentration in the solution was determined using a colorimetric assay for primary amines [46–48]. The pPEMA-pAAm hydrogels released about 70 µg of tobramycin in the first 24 h in solutions with and without Mg^{2+}/Ca^{2+} ions (Fig. 4). The initial burst was likely due passive diffusion of unbound tobramycin entrapped in the hydrogel matrix. During the next 24 h, the rate of release declined to 10 and 7 µg ml^{-1} for the solutions with and without Mg^{2+}/Ca^{2+} ions, respectively. The MBC of tobramycin for *P. aeruginosa*, 2 µg ml^{-1} was included in Fig. 4 as a reference point. The daily release from a 140 µl hydrogel remained above the MBC for greater than 50 days. The daily release was less than 0.1% of the total tobramycin loaded in the hydrogel. The cumulative release after 60 days was 600 and 350 µg, respectively, in the saline solutions with and without Mg^{2+}/Ca^{2+} ions ($P < 0.001$) (Fig. 4A). For comparison, the rate of release from a 7.5 wt% pAAm hydrogel decreased to zero within two days and the cumulative release was ~2 mg, close to 100% of the loaded tobramycin (Fig. 4A). A major concern with antibiotic eluting materials and devices is that the antibiotic concentration could fall below the bactericidal concentration before the infection is completely eradicated, creating an environment for selection of antibiotic resistance strains. The *in vitro* elution conditions may not have accurately reflected *in vivo* conditions in tissues. Nevertheless, the continuous release of a bactericidal concentration for greater than 50 days, as well as the large total amount of tobramycin released, suggested the pPEMA-pAAm hydrogels will be capable of complete eradication of established infections *in vivo*, and therefore may have low potential for promoting development of bacterial drug resistance.

Total cumulative release after 50 days was only 5% of the total tobramycin loaded into the hydrogels. Similarly low percentages

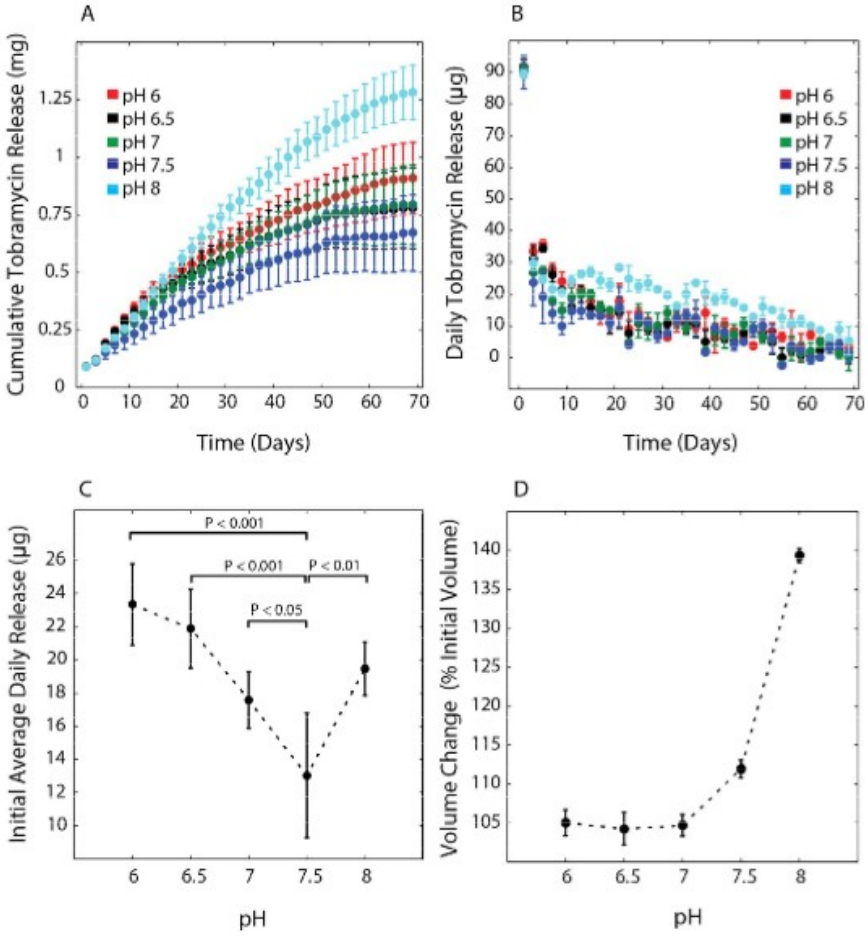

Fig. 5. pH dependence of tobramycin release from pPEMA-pAAm gels in buffered saline. (A) Cumulative release of tobramycin. (B) Daily release of tobramycin. (C) Average daily tobramycin release over the first 10 days. Brackets represent statistically significant differences between means ($P < 0.05$). (D) Volume change after 30 days as a percent of the initial volume. n = 3, error bars represent +/− 1 S.D.

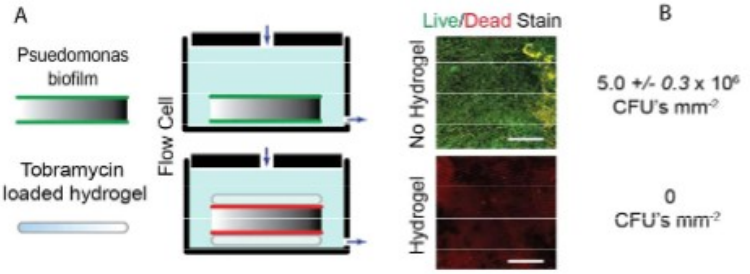

Fig. 6. Schematic of the flow cell bioreactor. Left: *P. aeruginosa* biofilms (green) were grown on both surfaces of stainless steel coupons (shaded grey) that were then placed in direct contact with tobramycin-loaded pPEMA-pAAM hydrogels (shaded light blue). Fresh medium was flowed through the cell at 5 ml h^{-1} to simulate fluid flux in tissue. Biofilm CFUs were counted after 24 and 72 h. Right: Treated biofilms were also stained for live (green) and dead (red) cells and imaged by confocal microscopy after 24 h. Representative confocal microscope fluorescent images of untreated biofilms and biofilms in contact with tobramycin hydrogels. Biofilm CFUs +/− 1 S.D. per surface area (n = 3) are displayed to the right of the confocal images. Scale bars = 400 μm. (For interpretation of the references to colour in this figure legend, the reader is referred to the web version of this article.)

of total release have been observed in other ionic systems. For example, a viscous gel of poly(allylamine hydrochloride) and inorganic polyphosphate released less than 3% of a charged drug proxy over 160 days [44]. Additional experiments with other aminoglycoside antibiotics with fewer positive charges, and with alternate pPEMA-pAAm hydrogels structures, fewer crosslinks and less deswelling for example, are necessary to understand the mechanistic basis for the modest total release.

Similar to the pPEMA-pAAm hydrogels, 2-methacryloxyethyl phosphate (MOEP) monomers were incorporated into soft contact lenses to release of naphazoline (2-(1-naphthylmethyl)-2-imidazoline hydrochloride), a vasoconstrictor with a single positive charge, for up to 5 h [38]. Compared to the pPEMA-pAAm hydrogels reported here, the concentrations of phosphate sidechains was limited by the need to maintain the precise shape and volume of the contact lenses.

3.2.3. pH dependence of tobramycin release

The pH at the application site of the tobramycin releasing hydrogels can vary considerably. For example, the pH can range from less than 6 to greater than 8 in a healing wound [64]. To investigate release in a range of physiological conditions, the effect of external pH on the tobramycin release rate was determined over the pH range 6–8. During the first 24 h, the cumulative release was approximately 90 μg for all pH values, which was likely due to the burst release of unbound tobramycin (Fig. 5B). After 24 h, the release varied significantly with pH ($P < 0.001$). Comparing the average daily release over the first 10 days (Fig. 5C), showed that the minimum release rate occurred near pH 7.5 and increased significantly at both higher and lower pH values ($P < 0.001$–0.05). Based on published potentiometric titrations of tobramycin, the pK_a values of the five tobramycin primary amines are 5.7, 7.1, 7.8, 8.3, and 8.9 [63]. Correspondingly, the calculated average number of positive charges on tobramycin are 4.2, 2.8, and 2.1 at pH 6.0, 7.5, and 8.0, respectively. The degree of ionization of the phosphate sidechains in the pPEMA-pAAm hydrogel as a function of pH was determined by potentiometric titration in 150 mM NaCl (Fig. S2). The mid-point of the transition from mono- to dianionic occurred around pH 7.4, near the pK_{a2} of free phosphate (Fig. S2). However, the transition was broad due to the range of phosphate microenvironments in the hydrogel matrix. The average charge on the phosphate sidechains varied from −1 to −2 as the pH was varied from 6 to 8.

The release rate minimum at pH 7.4 suggests that the ratio of tobramycin positive charges to phosphate negative changes at pH 7.4 results in the maximum electrostatic restriction of tobramycin diffusion, and thereby the slowest release rate. At lower pH, the average charge on tobramycin increased, but the decrease in phosphate charges in the hydrogel matrix resulted in less electrostatic restriction on tobramycin diffusion out of the hydrogels and greater release. The higher release rates at lower pH were not due to greater hydrogel porosity because the volume of the hydrogels was unchanged (Fig. 5D). The higher release rates at pH 8 could be due to both decreasing average charge density on tobramycin and to hydrogel swelling as additional phosphate sidechains were ionized (Fig. 5D) [26,37,65]. Regardless of the mechanism of the pH dependence, the results demonstrated that the pPEMA-pAAm hydrogels were capable of sustained release of tobramycin above the *P. aeruginosa* MBC over the pH range of 6 to 8 for at least 50 days.

3.3. Efficacy against established P. aeruginosa biofilms

To evaluate effectiveness against bacteria in established biofilms, the hydrogel disks were placed in direct contact with *P. aeruginosa* biofilms grown on stainless steel coupons in a flow cell bioreactor (Fig. 6). Medium was flowed past the biofilm at ~5 ml h^{-1} to mimic fluid flux in a living tissue environment [60]. The continuous flow prevented accumulation of free tobramycin in the chamber as it was released from the hydrogels. The effect of tobramycin loaded hydrogels on the biofilms compared to untreated biofilms was visualized by confocal microscopy using a fluorescent live/dead stain (Fig. 6). Untreated biofilms contained $5.0 +/- 0.3 \times 10^6$ CFUs mm^{-2} (n = 3). Biofilms in contact with tobramycin-loaded hydrogels had a 4 $\log_{10}$ reduction of CFUs mm^{-2} after 24 h. The CFUs were reduced to zero—a 6 $\log_{10}$ reduction in CFUs mm^{-2}—after 72 h (Fig. 6). In other words, a bactericidal concentration of tobramycin penetrated the biofilm within 72 h resulting in complete eradication. Unloaded hydrogel controls showed that eradication of the biofilm was not caused by physical contact with the hydrogels. The complete eradication of established biofilms is critical because some biofilms are capable of reinitiating infections with as few as 10^2 CFU g^{-1} of tissue [66–68]. Administration of free tobramycin is considered successful if 1–3 $\log_{10}$ reductions to below 10^5 CFU g^{-1} are achieved.

4. Conclusions

Localized and prolonged delivery of high concentrations of tobramycin from pPEMA-pAAm bulk hydrogels was shown to be effective both against planktonic *P. aeruginosa* and also established *P. aeruginosa* biofilms. The sustained release profile maintained

tobramycin concentrations above the *P. aeruginosa* MBC for greater than 50 days, in the presence of physiological concentrations of divalent metal ions, and over the pH range expected in healing wounds. Synthesis and loading of the hydrogels were simple compared to other methods of achieving prolonged release from hydrogels [30,34,36,39]. The hydrogels can be molded to any size and shape, or applied as thin films on rigid substrates. The tobramycin loaded hydrogels are promising candidates for localized and prolonged prevention or treatment of *P. aeruginosa* infections in wounds and surgical sites, including bacterial populations in established biofilms. In future studies other polycationic aminoglycoside antibiotics, which are expected to have qualitatively similar loading and elution characteristics, will be evaluated against *P. aeruginosa* and other pathogenic bacteria, including *Staphylococcus aureus*, the major causative agent in bone and joint infections [69]. This additional characterization will allow the pPEMA-pAAm hydrogels to be designed for specific clinical indications.

Finally, we have reported previously that similar double network pPEMA63MA27-pAAm hydrogels crosslinked with multivalent metal ions are tough, self-recovering, and load dissipating [45]. In fact, pPEMA63MA27-pAAm hydrogels loaded with Ca^{2+} or Zn^{2+} were tougher than articular and meniscal cartilage loaded in tension. Since only 5% of the total tobramycin loading capacity of the hydrogels was sufficient to maintain the concentration above the tobramycin MBC for *P. aeruginosa* for up to 50 days, it is conceivable that combined loading of lower amounts of aminoglycosides in combination with multivalent metal ions could result in tough double network hydrogels that play a structural role in tissue replacement as well as providing sustained local release of antibiotics.

Acknowledgments

This work was supported by the Army Research Office (W911NF1310319) and by the Center for Rehabilitation Science Research, Department of Physical Medicine & Rehabilitation, Uniformed Services University, Bethesda, MD (HU0001-11-1-0004 and HU0001-15-2-0003). The work was also supported with resources and facilities at the George E. Wahlen Department of Veterans Affairs, Salt Lake City, UT. The contents do not represent the views of the U.S. Department of Veterans Affairs or the United States Government. We thank Richard Tyler Epperson and Gina Allyn for help with imaging and biofilms as well as Dr. Ted Liu, M.D. for helpful discussions.

Appendix A. Supplementary data

Supplementary data associated with this article can be found, in the online version, at http://dx.doi.org/10.1016/j.actbio.2016.12.030.

References

[1] P.D. Sponseller, D.M. LaPorte, M.W. Hungerford, K. Eck, K.H. Bridwell, L.G. Lenke, Deep wound infections after neuromuscular scoliosis surgery: A multicenter study of risk factors and treatment outcomes, Spine 25 (2000) 2461–2466, http://dx.doi.org/10.1097/00007632-200010010-00007.
[2] R. Fitzgerald, D. Nolan, D. Ilstrup, R. Van Scoy, J. Washington, M. Coventry, Deep wound sepsis following total hip arthroplasty, J. Bone Joint Surg. 59 (1977) 847–855.
[3] N. Nakano, T. Matsumoto, K. Ishida, N. Tsumura, H. Muratsu, T. Hiranaka, R. Ryosuke, M. Kurosaka, Factors influencing the outcome of deep infection following total knee arthroplasty, Knee 22 (2015) 328–332, http://dx.doi.org/10.1016/j.knee.2015.04.005.
[4] J.D. Whitehouse, N.D. Friedman, K.B. Kirkland, W.J. Richardson, D.J. Sexton, The impact of surgical-site infections following orthopedic surgery at a community hospital and a university hospital, Infect. Control Hosp. Epidemiol. 23 (2002) 183–189.
[5] W.J. Costerton, M. Wilson, Introducing biofilms, Biofilms 1 (2004) 1–4, http://dx.doi.org/10.1017/S1479050504001164.
[6] P.S. Stewart, J.W. Costerton, Antibiotic resistance of bacteria in biofilms, Lancet 358 (2001) 135–138.
[7] P.S. Stewart, Mechanisms of antibiotic resistance in bacterial biofilms, Int. J. Med. Microbiol. 113 (2002) 107–113.
[8] E. Drenkard, Antimicrobial resistance of *Pseudomonas aeruginosa* biofilms, Microbes Infect. 5 (2003) 1213–1219, http://dx.doi.org/10.1016/j.micinf.2003.08.009.
[9] S.M. Dorrington, M.P.E. Slack, H.L. Walmsley, Inhibition of tobramycin diffusion by binding to alginate, Antimicrob. Agents Chemother. 32 (1988) 518–523.
[10] C.B. Whitchurch, T. Tolker-nielsen, P.C. Ragas, J.S. Mattick, Extracellular DNA required for bacterial biofilm formation, Science 295 (2002) 1487.
[11] K.R. Allison, M.P. Brynildsen, J.J. Collins, Metabolite-enabled eradication of bacterial persisters by aminoglycosides, Nature 473 (2011) 216–220, http://dx.doi.org/10.1038/nature10069.
[12] D.G. Davies, M.R. Parsek, J.P. Pearson, B.H. Iglewski, J.W. Costerton, E.P. Greenberg, The involvement of cell-to-cell signals in the development of a bacterial biofilm, Science 280 (1998) 295–298.
[13] N. Kaldalu, V. Hauryliuk, T. Tenson, Persisters—as elusive as ever, Appl. Microbiol. Biotechnol. (2016) 6545–6553, http://dx.doi.org/10.1007/s00253-016-7648-8.
[14] D.J. Leaper, Surgical-site infection, Br. J. Surg. 97 (2010) 1601–1602, http://dx.doi.org/10.1002/bjs.7275.
[15] M.L. Schweizer, J.J. Cullen, E.N. Perencevich, M.S. Vaughan Sarrazin, Costs associated with surgical site infections in veterans affairs hospitals, JAMA Surg. 149 (2014) 575–581, http://dx.doi.org/10.1001/jamasurg.2013.4663.
[16] National Collaborating Centre for Women's and Children's HealthSurgical Site Infection: Prevention and Treatment of Surgical Site Infection, RCOG Press, London, 2008, ISBN 978-1-904752-69-1.
[17] S.M. Kurtz, E. Lau, J. Schmier, K.L. Ong, K. Zhao, J. Parvizi, Infection burden for hip and knee arthroplasty in the United States, J. Arthroplasty. 23 (2008) 984–991, http://dx.doi.org/10.1016/j.arth.2007.10.017.
[18] N.M. Bernthal, A.I. Stavrakis, F. Billi, J.S. Cho, T.J. Kremen, S.I. Simon, A.L. Cheung, G.A. Finerman, J.R. Lieberman, J.S. Adams, L.S. Miller, A mouse model of post-arthroplasty Staphylococcus aureus joint infection to evaluate in vivo the efficacy of antimicrobial implant coatings, PLoS One 5 (2010) 1–11, http://dx.doi.org/10.1371/journal.pone.0012580.
[19] K.J. Bozic, M.D. Ries, The impact of infection after total hip arthroplasty on hospital and the impact of infection after total hip arthroplasty on hospital and surgeon resource utilization, J. Bone Joint Surg. 87 (2005) 1746–1751, http://dx.doi.org/10.2106/JBJS.D.02937.
[20] S. Kurtz, K. Ong, E. Lau, F. Mowat, M. Halpern, Projections of primary and revision hip and knee arthroplasty in the United States from 2005 to 2030, J. Bone Joint Surg. 89 (2007) (2005) 780–785, http://dx.doi.org/10.2106/JBJS.F.00222.
[21] J.W. Costerton, Biofilm theory can guide the treatment of device-related orthopaedic infections, Clin. Orthop. Relat. Res. 437 (2005) 7–11, http://dx.doi.org/10.1097/01.blo.0000175128.44966.d9.
[22] S.J. Dancer, How antibiotics can make us sick: The less obvious adverse effects of antimicrobial chemotherapy, Lancet Infect. Dis. 4 (2004) 611–619, http://dx.doi.org/10.1016/S1473-3099(04)01145-4.
[23] B. Cunha, Antibiotic Side Effects: General Review, Med. Clin. North Am. 85 (2001) 149–185. http://www.medscape.com/viewarticle/410873_2.
[24] J. Wright, D.S. Paauw, Complications of antibiotic therapy, Med. Clin. North Am. 97 (2013) 667–679, http://dx.doi.org/10.1016/j.mcna.2013.02.006.
[25] T.R. Hoare, D.S. Kohane, Hydrogels in drug delivery: Progress and challenges, Polymer 49 (2008) 1993–2007, http://dx.doi.org/10.1016/j.polymer.2008.01.027.
[26] E. Caló, J.M.S. de Barros, M. Fernández-Gutiérrez, J. San Román, L. Ballamy, V.V. Khutoryanskiy, Antimicrobial hydrogels based on autoclaved poly(vinyl alcohol) and poly(methyl vinyl ether-alt-maleic anhydride) mixtures for wound care applications, RSC Adv. 6 (2016) 55211–55219, http://dx.doi.org/10.1039/C6RA08234C.
[27] H. Anwar, J.W. Costerton, Enhanced activity of combination of tobramycin and piperacillin for eradication of sessile biofilm cells of *Pseudomonas aeruginosa*, Antimicrob. Agents Chemother. 34 (1990) 1666–1671, http://dx.doi.org/10.1128/AAC.34.9.1666.
[28] N. Bhattarai, J. Gunn, M. Zhang, Chitosan-based hydrogels for controlled, localized drug delivery, Adv. Drug Delivery Rev. 62 (2010) 83–99, http://dx.doi.org/10.1016/j.addr.2009.07.019.
[29] T.R. Hoare, D.S. Kohane, Hydrogels in drug delivery: Progress and challenges, Polymer 49 (2008) 1993–2007, http://dx.doi.org/10.1016/j.polymer.2008.01.027.
[30] R.G. Schoenmakers, P. Van De Wetering, D.L. Elbert, J.A. Hubbell, The effect of the linker on the hydrolysis rate of drug-linked ester bonds, J. Controlled Release 95 (2004) 291–300, http://dx.doi.org/10.1016/j.jconrel.2003.12.009.
[31] C.S. Kwok, T.A. Horbett, B.D. Ratner, Design of infection-resistant antibiotic-releasing polymers II. Controlled release of antibiotics through a plasma-deposited thin film barrier, J. Controlled Release 62 (1999) 301–311, http://dx.doi.org/10.1016/S0168-3659(99)00105-4.
[32] M. Matsusaki, H. Sakaguchi, T. Serizawa, M. Akashi, Controlled release of vascular endothelial growth factor from alginate hydrogels nano-coated with polyelectrolyte multilayer films, J. Biomater. Sci. Polym. Ed. 18 (2007) 775–783, http://dx.doi.org/10.1163/156856207781034160.

[33] Y. Yeo, T. Ito, E. Bellas, C.B. Highley, R. Marini, D.S. Kohane, In situ cross-linkable hyaluronan hydrogels containing polymeric nanoparticles for preventing postsurgical adhesions, Ann. Surg. 245 (2007) 819–824, http://dx.doi.org/10.1097/01.sla.0000251519.49405.55.

[34] C.R. Nuttelman, M.C. Tripodi, K.S. Anseth, Dexamethasone-functionalized gels induce osteogenic differentiation of encapsulated hMSCs, J. Biomed. Mater. Res. Part A. 76 (2006) 183–195, http://dx.doi.org/10.1002/jbm.a.30537.

[35] K. Nakamae, T. Nishino, K. Kato, T. Miyata, A.S. Hoffman, Synthesis and characterization of stimuli-sensitive hydrogels having a different length of ethylene glycol chains carrying phosphate groups: loading and release of lysozyme, J. Biomater. Sci. Polym. Ed. 15 (2004) 1435–1446, http://dx.doi.org/10.1163/1568562042368095.

[36] M. Feeney, M. Giannuzzo, P. Paolicelli, M.A. Casadei, Hydrogels of dextran containing nonsteroidal anti-inflammatory drugs as pendant agents, Drug Delivery 14 (2007) 87–93, http://dx.doi.org/10.1080/10717540600740003.

[37] Y. Qiu, K. Park, Environment-sensitive hydrogels for drug delivery, Adv. Drug Delivery Rev. 64 (2012) 49–60, http://dx.doi.org/10.1016/j.addr.2012.09.024.

[38] T. Sato, R. Uchida, H. Tanigawa, K. Uno, A. Murakami, Application of polymer gels containing side-chain phosphate groups to drug-delivery contact lenses, J. Appl. Polym. Sci. 98 (2005) 731–735, http://dx.doi.org/10.1002/app.22080.

[39] K. Nakamae, T. Nishino, K. Kato, Synthesis and characterization of stimuli-sensitive hydrogels having a different length of ethylene glycol chains carrying phosphate groups : loading and release of lysozyme, J. Biomater. Sci. Polym. Ed. 15 (2004) 1435–1446.

[40] P. Andrade-vivero, E. Fernandez-gabriel, C. Alvarez-lorenzo, A. Concheiro, Improving the loading and release of NSAIDs from pHEMA hydrogels by copolymerization with functionalized monomers, J. Pharm. Sci. 96 (2007) 802–813, http://dx.doi.org/10.1002/jps.

[41] T. Coviello, P. Matricardi, C. Marianecci, F. Alhaique, Polysaccharide hydrogels for modified release formulations, J. Controlled Release 119 (2007) 5–24, http://dx.doi.org/10.1016/j.jconrel.2007.01.004.

[42] H.F. Chuang, R.C. Smith, P.T. Hammond, Polyelectrolyte multilayers for tunable release of antibiotics, Biomacromolecules 9 (2008) 1660–1668, http://dx.doi.org/10.1021/bm800185h.

[43] J.S. Moskowitz, M.R. Blaisse, R.E. Samuel, H.P. Hsu, M.B. Harris, S.D. Martin, J.C. Lee, M. Spector, P.T. Hammond, The effectiveness of the controlled release of gentamicin from polyelectrolyte multilayers in the treatment of Staphylococcus aureus infection in a rabbit bone model, Biomaterials 31 (2010) 6019–6030, http://dx.doi.org/10.1016/j.biomaterials.2010.04.011.

[44] P.G. Lawrence, P.S. Patil, N.D. Leipzig, Y. Lapitsky, Ionically cross-linked polymer networks for the multiple-month release of small molecules, ACS Appl. Mater. Interfaces 8 (2016) 4323–4335, http://dx.doi.org/10.1021/acsami.5b10070.

[45] D.D. Lane, S. Kaur, G.M. Weerasakare, R.J. Stewart, Toughened hydrogels inspired by aquatic caddisworm silk, Soft Matter 11 (2015) 6981–6990, http://dx.doi.org/10.1039/C5SM01297J.

[46] J. Hansen, E.N. Adeli, B. Kenyon, R. Parvizi, Routine use of antibiotic laden bone cement for primary total knee arthroplasty: impact on infecting microbial patterns and resistance profiles, J. Arthroplasty. 29 (2014) 1123–1127.

[47] L. Lin, J. Kim, H. Chen, R. Kowalski, V. Nizet, Component analysis of multi-purpose contact lens solutions to enhance activity against *Pseudomonas aeruginosa* and Staphylococcus aureus, Antimicrob. Agents Chemother. (2016), http://dx.doi.org/10.1128/AAC.00644-16.

[48] J. Pinna, A. Usai, D. Zanetti, S. Thomas, P.A. Kaliamurthy, Susceptibility of various corneal fungal isolates and *Pseudomonas aeruginosa* to contact lens disinfecting solutions, J. Infect. Dev. Ctries. 7 (2013) 261–268.

[49] G. Cirioni, O. Silvestri, C. Ghiselli, R. Orlando, F. Riva, A. Mocchegiani, F. Chiodi, L. Castelletti, S. Gabrielli, E. Saba, V. Scalise, Protective effects of the combination of α-helical antimicrobial peptides and rifampicin in three rat models of *Pseudomonas aeruginosa* infection, J. Antimicrob. Chemother. 62 (2008) 1332–1338.

[50] G. Cirioni, O. Ghiselli, R. Tomasinsig, L. Orlando, F. Silvestri, C. Skerlavaj, B. Riva, A. Rocchi, M. Saba, V. Zanetti, M. Scalise, Efficacy of LL-37 and granulocyte colony-stimulating factor in a neutropenic murine sepsis due to *Pseudomonas aeruginosa*, Shock 30 (2008) 443–448.

[51] Liang Jin, Jian Li, Roger L. Nation, Joseph A. Nicolazzo, Effect of systemic infection induced by *Pseudomonas aeruginosa* on the brain uptake of colistin in mice, Antimicrob. Agents Chemother. 56 (2012) 5240–5246.

[52] M.S. Kumar, R. Sripriya, H.V. Raghavan, P.K. Sehgal, Wound healing potential of Cassia fistula on infected albino rat model, J. Surg. Res. 131 (2006) 283–289.

[53] H. Shao, G.M. Weerasekare, R.J. Stewart, Controlled curing of adhesive complex coacervates with reversible periodate carbohydrate complexes, J. Biomed. Mater. Res. A 97 (2011) 46–51, http://dx.doi.org/10.1002/jbm.a.33026.

[54] K. Marshall, Thomas and Williams, elimination of the interference from aminoglycoside antibiotics in the pyrogallol red-molybdate protein dye-binding assay, Clin. Chem. 50 (2004) 1674–1675, http://dx.doi.org/10.1373/clinchem.2004.033548.

[55] S.P. Yip, M.L. Wong, Aminoglycoside interference in the pyrogallol red-molybdate protein assay is increased by the addition of sodium dodecyl sulfate to the dye reagent, Clin. Chem. 49 (2003) 2111–2112, http://dx.doi.org/10.1373/clinchem.2003.023622.

[56] S. Bernard, An improved pyrogallol red-molybdate for determining total urinary protein, Clin. Chem. 35 (1989) 2233–2236.

[57] M.R.C. Marques, R. Loebenberg, M. Almukainzi, Simulated biological fluids with possible application in dissolution testing, Dissolution Technol. (2011) 15–28.

[58] A.L. Barry, W.A. Craig, H. Nadler, L.B. Reller, C.C. Sanders, J.M. Swenson, Methods for determining bactericidal activity of antimicrobial agents; approved guideline, NCCLS document M26-A 19 (18) (1999).

[59] D.L. Williams, K.L. Woodbury, B.S. Haymond, A.E. Parker, R.D. Bloebaum, A modified CDC biofilm reactor to produce mature biofilms on the surface of PEEK membranes for an in vivo animal model application, Curr. Microbiol. 62 (2011) 1657–1663, http://dx.doi.org/10.1007/s00284-011-9908-2.

[60] D.L. Williams, B.S. Haymond, J.P. Beck, P.B. Savage, V. Chaudhary, R.T. Epperson, B. Kawaguchi, R.D. Bloebaum, In vivo efficacy of a silicone-cationic steroid antimicrobial coating to prevent implant-related infection, Biomaterials 33 (2012) 8641–8656, http://dx.doi.org/10.1016/j.biomaterials.2012.08.003.

[61] D.L. Williams, R.D. Bloebaum, Observing the biofilm matrix of Staphylococcus epidermidis ATCC 35984 grown using the CDC biofilm reactor, Microsc. Microanal. 16 (2010) 143–152, http://dx.doi.org/10.1017/S143192760999136X.

[62] D.L. Williams, J. Vinciguerra, J.M. Lerdahl, R.D. Bloebaum, Does vitamin E-blended UHMWPE prevent biofilm formation?, Clin Orthop. Relat. Res. 473 (2014) 928–935, http://dx.doi.org/10.1007/s11999-014-3673-z.

[63] A. Karaczyn, H. Kozl, Copper (II) binding to tobramycin : potentiometric and spectroscopic studies, Carbohydr. Res. 313 (1998) 265–269.

[64] L.A. Schneider, A. Korber, S. Grabbe, J. Dissemond, Influence of pH on wound-healing: a new perspective for wound-therapy?, Arch Dermatol. Res. 298 (2007) 413–420, http://dx.doi.org/10.1007/s00403-006-0713-x.

[65] D.L. Williams, Preventing Biofilm Implant-related Osteomyelitis using a Novel Synthetic Analog of Antimicrobial Peptides, University of Utah, 2012.

[66] D.L. Williams, J.W. Costerton, Using biofilms as initial inocula in animal models of biofilm-related infections, J. Biomed. Mater. Res. 100 (2012) 1163–1169, http://dx.doi.org/10.1002/jbm.b.31979.

[67] P.G. Bowler, The 10 (5) bacterial growth guideline: Reassessing its clinical relevance in wound healing, Ostomy Wound Manage. 49 (2003) 44–53.

[68] D.E. Fry, R.V. Fry, Surgical site infection: the host factor, AORN J. 86 (2007) 813–814, http://dx.doi.org/10.1016/j.aorn.2007.06.022.

[69] Lius Pulido, Elie Ghanem, Ashish Joshi, James Purtill, J. Parvizi, Periprosthetic joint infection: the incidence, timing, and predisposing factors, Clin. Orthop. Relat. Res. 466 (2008) 1710–1715, http://dx.doi.org/10.1007/s11999-008-0209-4.

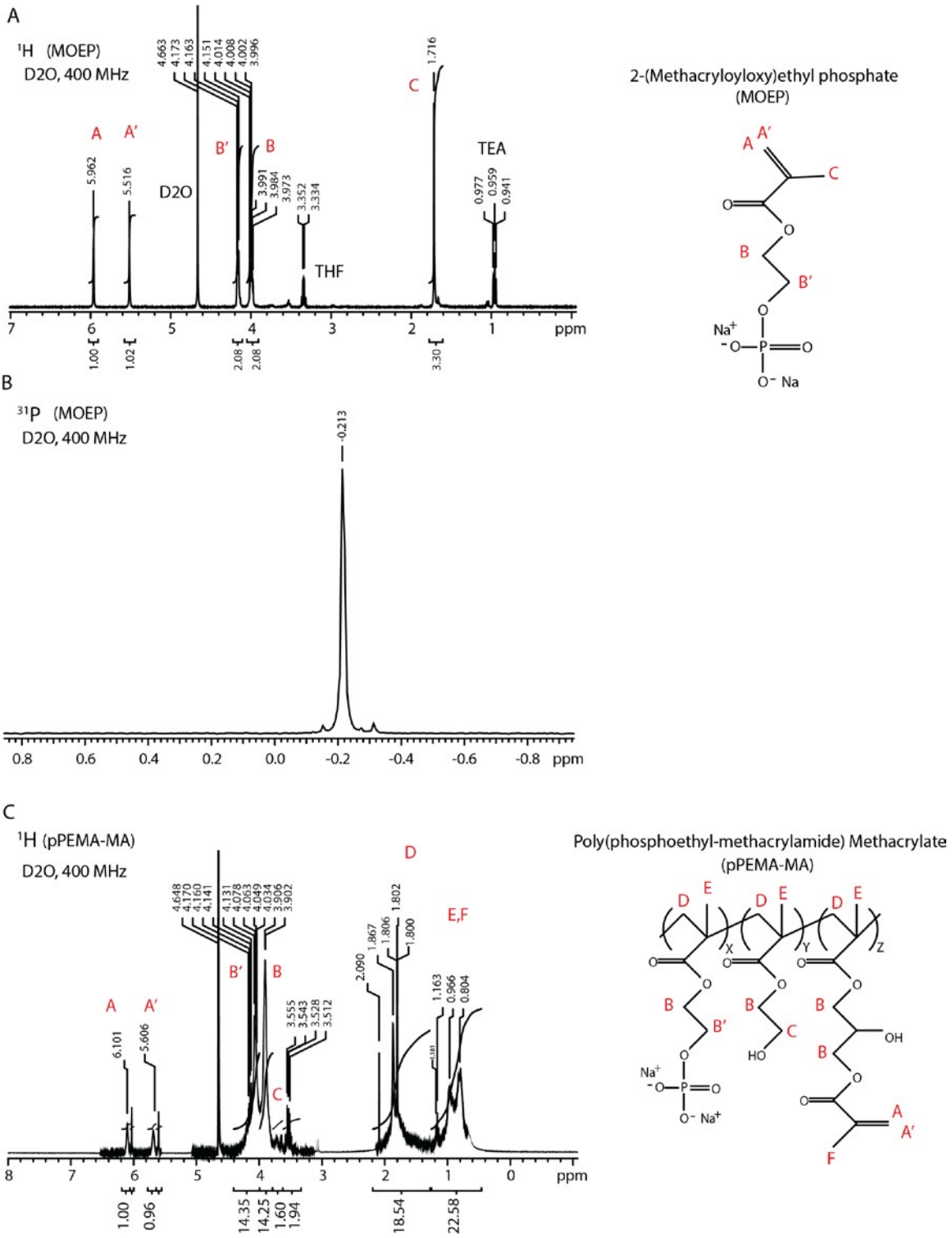

Figure 3.S1 A) H^1 NMR spectra for MOEP monomer. B) P^{31} NMR spectra for MOEP monomer. C) H^1 NMR spectra for pPEMA-MA polymer

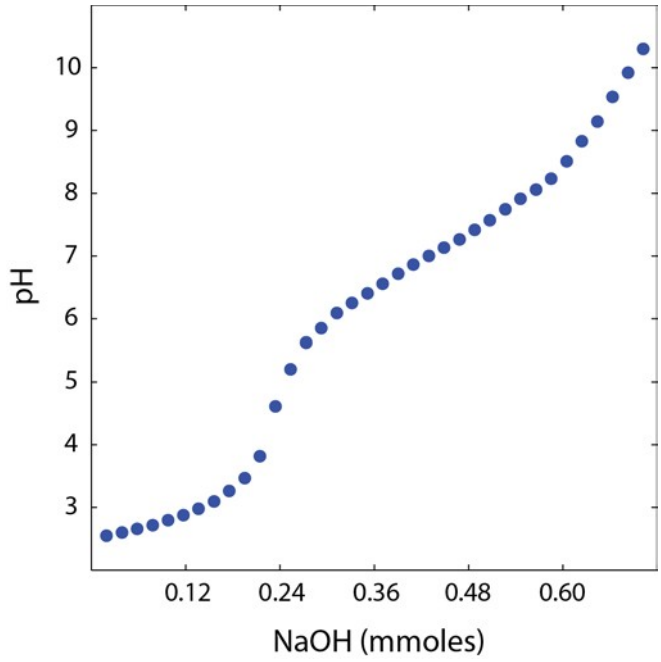

Figure 3.S2 Titration of pPEMA-pAAm hydrogels with NaOH.

CHAPTER 4

TOBRAMYCIN RELEASE FROM CADDISFLY INSPIRED TOUGH CA^{2+}/POLYPHOSPHATE DOUBLE NETWORK HYDROGELS

4.1 Introduction

Hydrogels are three-dimensional polymeric structures that retain large amounts of water and are currently employed as contact lens material, wound dressings, as scaffolds for tissue engineering, and as localized smart drug delivery materials.[1,2] Localized controlled delivery systems are intended to deliver drugs at prearranged rates for targeted periods of time and maintain high local concentrations while limiting the adverse effects from high systemic doses. The first hydrogels were developed in the 1960s and were simple networks like poly(2-hydroxyethyl methacrylate) (pHEMA) or poly(acrylamide) (pAAm).[3] Drug release from these simple single network hydrogels is purely diffusion based, for example, a pAAm hydrogel was shown to release its entire payload of tobramycin within 24 *h*.[4] However, more complex hydrogels have been adapted for *in vivo* use as controlled drug delivery materials with an ability to sustain drug release for much longer than 24 *h*.[5] Some strategies for sustained release have included: modification of gel microstructure to reduce diffusion of large molecules,[6–9] tying release to hydrogel degradation,[10] degradable conjugation of drug to the hydrogel network,[6,10–12] externally triggered volume changes to control diffusion,[8,9,13,14] diffusion restrictive thin surface coatings,[7,8] and electrostatic binding of charged molecules.[15–21] There is a particular need

for localized antibiotic drug release materials to both eliminate infection and avoid the pitfalls of traditional systemic delivery including organ toxicity, reduction of beneficial bacteria and overgrowth of resistant organisms such as Candida and Clostridium difficile.[22]

While hydrogels are promising materials for controlled drug delivery their application as *in vivo* implantable materials is hindered by their weak and brittle nature. Incorporation of a sacrificial component into the hydrogel structure results in increased toughness and blunting of crack propagation as the sacrificial network breaks resulting in preservation of the other network and maintaining hydrogel integrity. Sacrificial domains have been integrated into hydrogel structure through the use of Interpenetrating networks (IPN) or inclusion of double networks (DN). An example of an IPN hydrogel uses a densely crosslinked network of 2-acrylamide-2-methylpropanesulfonic acid interpenetrating within a sparsely crosslinked acrylamide network.[23] IPN hydrogels have the compressive strength of the densely crosslinked network in combination with the elasticity and extensibility of the loosely crosslinked network. During strain one network acts as an energy dissipating sacrificial domain, however accumulating damage in the sacrificial network reduces the long term usefulness of these IPN hydrogels. More complex hydrogels use covalent and noncovalent crosslinking to form a DN where the noncovalent crosslinked network acts as a reversible sacrificial domain to increase toughness while preventing damage accumulation through the reformation of noncovalent crosslinks. Examples of DNs include physical crosslinks,[24,25] hydrophobic bilayers,[26] dipole–dipole coupling,[27] electrostatic bonding between oppositely charged functional groups,[28] metal ion complexes,[29–31] controlling network structure and pore alignment[32], and reversible polymer absorption to solid particles.[33] By combining toughness with reversible crosslinks, DN hydrogels have emerged as a promising biomaterial compared to weak and brittle single network hydrogels and may expand the usefulness of hydrogels as *in viv*o controlled drug delivery

materials.

Caddisfly insects (order Trichoptera) have adapted a unique underwater silk that acts as a naturally occurring tough double network hydrated material. Caddisfly larva reside underwater in freshwater streams and lakes worldwide.[34] The success of this order in maintaining a diverse population across multiple freshwater habitats derives from a unique use of adhesive and tough underwater silk. Caddisfly silk comprises a viscoelastic silk core encased in a sticky peripheral layer allowing the larvae to construct protective underwater habitats from leaves, sticks, or stones. The viscoelastic properties of the silk has been associated with repetitive blocks of highly phosphorylated residues in the H-fibroin protein structure, the major protein constituent of the silk core.[35] When the silk is excreted in freshwater habitats the natural calcium present in freshwater sources crosslinks the phosphates inside the silk forming serial β-sheet domains of calcium crosslinked with phosphates. These phosphate-calcium domains rupture in response to stress leading to a pseudo-yield behavior that is recovered as phosphate and calcium domains reform in response to an elastic recoiling force. The tensile modulus of caddisfly silk ranges from 80-140 MPa with a strength of 10-20 MPa at 80% elongation and near 100% recovery of modulus and hysteresis within 120 m.[36,37] The modulus and toughness of the silk can be modified by exchanging calcium with other divalent metal ions further supporting the link between phosphate-metal crosslinks and observed mechanics.[38]

Other synthetic DN hydrogels have been improved by replacing the covalently linked sacrificial network with numerous types of reversible non-covalent crosslinks. These have included physical crosslinks,[24,25] hydrophobic bilayers,[26] dipole–dipole coupling,[27] electrostatic bonding between oppositely charged functional groups,[28] metal ion complexes,[29–31] controlling network structure and pore alignment[32], and reversible polymer absorption to solid particles.[33] By increasing toughness, DN hydrogels have emerged as a promising biomaterial compared to

weak and brittle single network hydrogels and can expand the usefulness of hydrogels as *in vivo* controlled drug delivery materials.

A biomimetic DN hydrogel was designed to derive toughness from phosphate-metal crosslinks, a common toughening component in natural materials such as caddisfly silk, spider fangs, stingers, and rag worm mandibles.[37,39,40] The DN hydrogel was synthesized from copolymerization and crosslinking of a polyphosphate prepolymer (pPEMA-MA) and polyacrylamide (pAAm).[41] The DN polyphosphate hydrogel was covalently crosslinked with bis-acrylamide crosslinker and MA groups on the prepolymer with a second network being formed with the addition of divalent metal ions. The result was a viscoelastic phosphate-metal crosslinked network in combination with an elastic covalently linked pAAm network. The resulting mechanics were strikingly similar to the caddisfly silk, including increased modulus up to 34.2 +/- 2.5 MPa, and pseudo yield behavior as metal-phosphate domains ruptured during strain. Like the caddisfly silk, the polyphosphate DN hydrogels self-recovered up to 90% of the modulus and hysteresis within 30 min as metal-phosphate crosslinks were reformed under the restoring force from the elastic network.

In addition to using phosphate metal complexes as a toughening component, the phosphate network can function as an aminoglycoside delivery vehicle by replacing divalent metals with polycationic aminoglycoside antibiotics.[4] Tobramycin loaded polyphosphate DN hydrogels were capable of sustained tobramycin release for up to 60 days, a result of electrostatically reduced diffusion of tobramycin out of the hydrogel. The sustained release resulted in formation of zones of inhibition against *Pseudomonas Aeruginosa* (*P.aeruginosa*) for 25 days and total eradication of *P.aeruginosa* biofilms within 72 h.

Despite extensive investigation into hydrogels as both drug delivery vehicles and as tough materials for *in vivo* applications there is an absence of reported DN hydrogels with

mechanisms for both toughening and sustained antibiotic release. Presented here is the use of a dual purpose double network polyphosphate hydrogel capable of replicating the toughness seen in caddisfly silk through phosphate-Ca^{2+} crosslinking while simultaneously binding and slowly releasing tobramycin antibiotic for over 60 days. This dual mechanism allows for tough hydrogels that could not only be used as structural materials in orthopedics, vascular access lines and bandages but also prevent and eliminate infections during and after invasive medical procedures.

4.2 Experimental section

4.2.1 Materials

Phosphorus(V) oxychloride, 2-hydroxyethyl methacrylate, triethylamine, and glycidyl methacrylate were purchased from Alfa Aesar (Ward Hill, MA). Methacrylic acid, 2,2'-azobis(2-methylpropionitrile), acrylamide, N,N'-methylene-bisacrylamide, and N,N,N',N'-tetramethylethylenediamine were purchased from Sigma Aldrich (St Louis, MO). Ammonium persulfate, Orion Ionplus calcium standard, and A optimum results filling solution were purchased from Fischer Scientific (Pittsburgh, PA). Tobramycin (97%) was acquired from Acros Organics (New Jersey, USA).

4.2.2 Synthesis of MOEP monomer and polyPEMA-MA copolymers

2-(Methacryloyloxy)ethyl phosphate (MOEP) was synthesized as previously described [42]. Briefly, phosphorus oxychloride (33.9 g, 220mmol) and hydroxylethyl-methacrylamide (HEMA) were mixed at a 0.7:1 molar ratio in dry toluene (480 mL) under argon. The reaction was stirred at 4°C and triethylamine (TEA) (77 mL) added in three increments over 10 m. Next the reaction was stirred at 22°C for 6 h under argon, then filtered to remove precipitated salt. The reaction

was cooled to 4°C before the addition of deionized water (480 mL), then stirred under argon at 22°C for 12 h. The reaction was extracted twice with diethyl ether (100 mL) and the organic layers discarded. The aqueous layer was extracted using tetrahydrofuran (THF) and diethyl ether (1:2, 12 X 225 mL), then dried over anhydrous sodium sulfate before evaporating the solvent.

Poly(phosphoethyl-methacrylate-co-acrylic acid) (pPEMA-AA) was synthesized by free radical polymerization of MOEP (85 mol%), and methacrylic acid (15 mol%) in methanol (12.5 mL mg^{-1} MOEP). MOEP and methacrylic acid were degassed by bubbling with argon for 1 h, followed by addition of azo-bis-isobutyronitrile (AIBN, 4.5 mol%) at 55°C to initiate polymerization. The reaction was stirred for 15 h before precipitation with acetone, then dissolved in water (200 mL H_2O per 17 g pPEMA-AA). Afterward, methacrylate groups (MA) were grafted onto the methacrylic acid sidechains with glycidyl methacrylate in 9-fold molar excess relative to the carboxylate sidechains. The methacrylated pPEMA-AA (pPEMA-MA) was adjusted to pH 7.3 with NaOH and purified by tangential flow filtration using a Millipore Pellicon 3 cassette filter with an Ultracel 10 kD membrane. The polymer product was lyophilized, and stored at -20°C.

The structure and composition of the monomer (MOEP) and polymers (pPEMA-MA) were verified by ^{1}H and ^{31}P NMR.[4] The pPEMA-MA polymer contained 65 mol% phosphate sidechains, 12 mol% HEMA, and 23 mol% MA sidechains. The molecular weight (Mw) and polydispersity index (PDI) of pPEMA-MA were determined by size exclusion chromatography (SEC) on an Agilent Infinity 1260 HPLC system with a PL-Aquagel-OH Mixed-M column (8 µm, 300x 7.5mm) column. The column buffer was 0.1 M $NaNO_3$ / 0.01 M NaH_2PO_4, pH 8.0 with a flow rate of 1 mL m^{-1}. The average M_m and PDI, 46 kg mol^{-1} and 1.67, respectively, were estimated using sodium polymethacrylic acid standards.

MOEP; ^{1}H NMR (D2O, 400 MHz); 5.9 (s, 1H), 5.5 (s, 1H), 4.2 (m, 2H), 4.0 (m, 2H), 1.7 (s, 3H).

^{31}P NMR (D2O, 400 MHz), 0.213 (s).

pPEMA-MA; ^{1}H NMR (D2O, 400 MHz); 6.1 (s, 1H), 5.6 (s, 1H), 4.2 (m, 2H), 4.1 (m, 2H), 3.5 (m, 2H), 1.8 (t, 2H), 1.0 (s, 3H), 0.8 (s, 3H).

4.2.3 Hydrogel synthesis: copolymerization of polyPEMA-MA and acrylamide

Hydrogels were formed by free radical polymerization of the pPEMA-MA prepolymer with acrylamide (Aam) and N,N-methylenebisacrylamide (bis-Aam), a bifunctional crosslinker, in 150 mM NaCl (Figure 4.1 A,B). The wt% of pPEMA-MA and AAm/bis-AAm were 6.5% and 1.0%, respectively. The molar ratio of AAm to bis-AAm was 60:1. Polymerization was initiated by adding 10% ammonium persulfate (APS) and tetramethylethylenediamine (TEMED) to final concentrations of 70 µg ml^{-1} and 2.4 µl ml^{-1}, respectively. Following addition of APS and TEMED, 250 µl aliquots were placed in wells of a 48 well plate with 200 µl of 2-propanol floated on top to limit oxygen exposure. After 90 m, polymerized hydrogel disks were removed and soaked in 150 mM NaCl for 24 h to remove unreacted reagents.

4.2.4 Determination of Ca^{2+} and tobramycin loading by measuring depletion in loading solutions

Uniform 250 µl hydrogel discs were immersed in 150 mM NaCl and Ca^{2+} at molar ratios of 1.8, 0.8, 0.3 and 0.1 total Ca^{2+}:OPO_3^{2-}. Ca^{2+} loaded hydrogels were subsequently loaded with 5 mM tobramycin and 150 mM NaCl adjusted to pH 7.7 with HCl for 12 h. Time lapse videos of hydrogel deswelling during Ca^{2+} and tobramycin loading were analyzed in Image J to measure hydrogel diameters. Isotropic shrinking was assumed to calculate volume changes from the diameter. Mechanical tests were performed both prior to and after loading with tobramycin.

Total tobramycin concentrations in the hydrogels was determined by depletion of

tobramycin in the loading solution. Tobramycin concentrations were measured colorimetrically using a Pyrogallol Red-Molybdate (PRM) assay for primary amines [43–45]. A PRM solution was prepared by mixing 0.4 mL of 1.2 mg/mL pyrogallol red in methanol, 9 mL of a solution of 55 mM succuinic acid and 4 mM sodium benzoate, and 0.04 mL each of 12 mM disodium molybdate and 261 mM sodium oxalate. Tobramycin containing samples (40 µL) were added to 160 µl of the PRM solution in a clear 96 well plate. After 45 min at 22° C absorbance at 600 nm was measured in a Spectra Max M2 plate reader and compared to tobramycin standards.

Total Ca^{2+} concentration was determined by depletion of Ca^{2+} in the loading solution. Ca^{2+} concentrations were measured using an Orion 9700 BNWP calcium selective probe paired with an Orion Dual Star meter from Fisher Scientific. A direct calibration curve of electrode potentials of standard solutions were measured and experimental solutions were compared to the linear range of the standard curve to determine concentration. Orion Ionplus calcium standard (0.1 M Ca^{2+}) was diluted in 130 mM NaCl for the calibration curve and Orion A Optimum Results filling solution was used to fill the interior of the probe.

4.2.5 Determination of release kinetics from Ca^{2+}-tobramycin hydrogels

Three tobramycin and 0.5 Ca^{2+}:OPO_3^{2-} loaded hydrogels disks were submerged in 2 mL of 130 mM NaCl, plus 1.5 mM Mg^{2+}, 2.5 mM Ca^{2+} and 5 mM 4-(2-hydroxyethyl)-1-piperazineethanesulfonic acid (HEPES) at pH 7.3 to approximate physiological ionic strength and the presence of physiological concentrations of divalent metal ions [46]. The 2 mL solutions were replaced with fresh 2 mL solutions after 1, 2, 4, 12, and 24 h on day one, then every 24 h thereafter. The tobramycin concentration in the solutions was determined using the PRM colorimetric assay. The 2 mL volume was ~15 times greater than the volume of the loaded hydrogel (~140 µL) and resulted in tobramycin concentration within the detectable window of

the colorimetric assay (0.001 to 0.05 mg mL^{-1}).

4.2.6 Loading and release of vancomycin using UV-Vis spectroscopy

Uniform 250 µL hydrogel discs were immersed in 150 mM NaCl and 5 mM Vancomycin HCl for 24 h. Vancomycin concentrations were measured by comparing absorbance values at 280 nm with a standard curve. Total vancomycin loading was measured via depletion of vancomycin in the loading solution. Vancomycin release kinetics was performed as described for tobramycin in section 2.5. Absorbance measurements were taken from a Spectra Max M2 cuvette reader.

4.2.7 Mechanical testing of hydrogels

Hydrogels were compressed while submerged in 130 mM NaCl, 1.5 mM Mg^{2+}, 2.5 mM Ca^{2+}, and 5 mM HEPES at pH 7.3 on an Instron 3342 material test system controlled with Bluehill 3 software (Instron, Inc.). Hydrogels were compressed at a rate of 0.15 s^{-1} to 80% compression for mechanical comparison of loading ratios. For recovery tests hydrogels were cyclically compressed to 50% 10 times to maximize hysteresis and modulus reduction. Following the 10^{th} cycle the hydrogels were rested while submerged for 30 min and cycled to 50% to determine recovery of modulus, hysteresis and strength. In all tests hydrogels underwent an initial conditioning compressive cycle to 50% with a 60 min dwell time before beginning mechanical tests.

4.2.8 Compressive cycles and subsequent tobramycin release

Hydrogels were cyclically compressed to 50% at a rate of 6 cycles per min to assess the effect of compression due to manipulation of joints or normal gait on release of tobramycin. Hydrogels were immersed in 2 mL of 130 mM NaCl, 1.5 mM Mg^{2+}, 2.5 mM Ca^{2+} and 5 mM HEPES at pH 7.3 during compression with control gels immersed in the same volume under no mechanical strain. The solution was replaced every 24 h and concentration of released tobramycin was measured with the PRM colorimetric assay.

4.2.9 Infrared spectroscopy

Ca^{2+} and tobramycin loaded pPEMA-pAAm hydrogels were lyophilized to remove water, and crushed into a powder using an agar mortar and pestle before applying to the diamond ATR crystal. ATR-FTIR absorbance spectra were collected using a Nicolet 6700 spectrometer (Thermo Scientific, FL) with a diamond Smart iTR accessory, a deuterated triglycine sulfate detector, and a KBr/Ge mid-infrared optimized beamsplitter. Spectra were recorded with a resolution of 4 cm^{-1} and as 512 averaged scans. The IR spectra were normalized to the intensity of an absorption band centered at 1665 cm^{-1}, which corresponds to absorption by amide groups in the polymethacrylamide backbone.[47] The integrated intensity of bands corresponding to degenerate $P\text{-}O^-$ symmetric stretching modes between 950 and 1050 cm^{-1} were measured for changes over time to identify any loss of phosphates due to hydrolysis.[36,48,49]

4.2.10 Statistical methods and data processing

Data are reported as mean +/- 1 standard deviation with an n of 3. Mean and standard deviation was calculated using Microsoft Excel. Mechanics data was processed using Matlab software (Mathworks). The initial modulus was determined from the slope of a linear fit of the

first 15% of the compressive cycle. Strength at 80% represents the maximum stress in the cyclic stress strain curve. Energy dissipation, strain cycle hysteresis, was computed by subtracting the trapezoidal integration of the reverse curve from the forward curve of cyclical tests. Difference between means was tested for statistical significance using a one way ANOVA using IBM SPSS Statistical Analysis 24 software.

4.3 Results and discussion

4.3.1 The utility of a tough, tobramycin loaded hydrogel

Tough Ca^{2+} loaded pPEMA-pAAm hydrogels were subsequently loaded with tobramycin to act as a prophylactic in orthopedic procedures or to eradicate biofilm based infections arising after joint replacement surgery. Tobramycin and gentamycin are the most commonly used antibiotics for loading bone cement for orthopedic applications.[50] Tobramycin was selected for loading into pPEMA-pAAM hydrogels due to its broad spectrum effectiveness against both staph and pseudomonas which make up over 80% of orthopedic infections.[20,50–53] Vancomycin is a common antimicrobial for use in orthopedics, especially against methicillin-resistant *S aureus* (MRSA), and was also explored for loading into pPEMA-pAAM hydrogels but lacked the sustained release profile as observed with loaded aminoglycoside antibiotics.[54,55]

4.3.2 Synthesis of Ca^{2+} and tobramycin crosslinked double network hydrogel

Crosslinking polycations with phosphates in pPEMA-pAAm hydrogels results in shrinking and can be controlled by adjusting the concentration of polycation, which results in sequential binding of different fractions of total phosphates. Submerging pPEMA-pAAm hydrogels in Ca^{2+} or polycationic aminoglycoside antibiotics like tobramycin resulted in rapid shrinking of the

hydrogel by up to 50% and the emergence of a second network structure comprised of electrostatic crosslinks between phosphates and Ca^{2+} or tobramycin (Figure 4.1C). pPEMA-pAAm hydrogels were first loaded with varying ratios of Ca^{2+} to OPO_3^{2-} resulting in a controlled volume decrease of 50% for higher Ca^{2+}:OPO_3^{2-} ratios (1.8 and 0.8), and only 20% volume decrease for 0.3 Ca^{2+}:OPO_3^{2-}. There was no volume decrease when Ca^{2+} was sufficiently low, 0.1 Ca^{2+}:OPO_3^{2-} (Figure 4.2A,C). The degree of volume change correlates with the amount of available Ca^{2+} and the quantity of formed crosslinks with phosphates. More available Ca^{2+} and thus more crosslinks leads to greater volume change. This volume change was used to estimate quantities of calcium required to crosslink only a fraction of phosphate binding sites, thus allowing for a subsequent equilibration and crosslinking with positively charged tobramycin.

To further explore the effect of charge on complex formation and crosslinking, pPEMA-pAAM hydrogels were loaded with tobramycin at pH ranging from 4 to 9. Gels shrink to ~50% the original volume at pH 4 due to crosslink formation between monovalent phosphates and tobramycin with 5 positively charged amines with pKa's of 6.2, 7.4, 7.4, 7.6 and 8.6, Figure 4.3A.[56] As pH is increased up to 7.7 the hydrogels still shrink by ~50% as phosphates become divalent with approximately 2.5 positive charges on tobramycin at pH 7.7.[56] At pH 8 the volume shrinks by 30% and only by 4% at pH 9, which corresponds to a drop in charge to less than 2+ on tobramycin, Figure 4.3A, B. This supports the argument that crosslinking is a result of multiple phosphates (that may be monovalent or divalent) interacting with tobramycin, which must have at least 2 positive charges to form the complex.

The combination of a calcium selective probe and colorimetric assay for tobramycin provided a quantitative measure of loaded Ca^{2+} or tobramycin and verified the possibility of sequential crosslinking of fractions of unbound phosphates. The total loaded Ca^{2+} decreased from 355 +/- 41, 177 +/- 38, 124 +/- 14, and 47 +/- 11 mg mL^{-1} with decreasing Ca^{2+} to OPO_3^{2-}

ratios of 1.8, 0.8, 0.3, 0.1 respectively (Figure 4.2D). The decreasing mass of loaded Ca^{2+} correlated with less shrinking observed with lower amounts of available Ca^{2+} and is consistent with less Ca^{2+}-tobramycin crosslinking. Ca^{2+} loaded pPEMA-pAAm hydrogels were subsequently submerged in 5 mM tobramycin resulting in a volume decrease down to 50% for hydrogels loaded with Ca^{2+} to OPO_3^{2-} ratios of 0.3 and 0.1 and no volume change for hydrogels already at 50% volume (Figure 4.2B,C). During tobramycin crosslinking some Ca^{2+} was exchanged with tobramycin in addition to crosslinking the remaining unbound phosphates. The loaded Ca^{2+} decreased during tobramycin loading from ratios of 1.8, 0.8, 0.3 and 0.1 Ca^{2+}:OPO_3^{2-} to 1.6. 0.5, 0.2, and 0.1 respectively. Total tobramycin loaded into the hydrogels was determined by measuring depletion of tobramycin in the loading solution via a colorimetric assay and was greatest at 15 +/- 3 mg mL^{-1} for hydrogels loaded with the least Ca^{2+} (0.1 Ca^{2+} to OPO_3^{2-}). Loaded tobramycin decreased to 72 +/- 2, 164 +/- 3 and 191 +/- 9 mg ml^{-1} for hydrogels with increasing loaded Ca^{2+}; 0.2, 0.5, and 1.6 Ca^{2+} to OPO_3^{2-} respectively. This trend of greater tobramycin loading with decreasing loaded Ca^{2+} is illustrated in Figure 4.2D and is explained by there being a greater fraction of phosphates available for binding.

While polyphosphate hydrogels are adept at binding and concentrating aminoglycoside antibiotics other antibiotics like glycopeptides such as vancomycin are not retained in the same way. For comparison, hydrogels loaded with vancomycin did not result in hydrogel shrinking and had a lower loading concentration (1.02 +/- 0.1 mg mL^{-1}) and therefore little or no crosslinking of phosphates. Vancomycin has more diverse ionizable groups including one carboxyl, two amino and three phenolic and has a total net charge from 2+ to 4-, depending on pH.[57] At pH 7.7, the net charge falls between 0 and 1-, which may explain the lack of electrostatically driven crosslinking of negatively charged phosphates.[57] In addition to charge differences, glycopeptides have much larger molecular weights than aminoglycosides; 1449.3 g mol^{-1} for vancomycin

versus 467.5 g mol^{-1} for tobramycin. Furthermore, glycopeptides have cyclical structures with carbohydrate and peptide components, which could affect the charge distributions or densities and therefore binding with phosphates in the hydrogel.

4.3.3 Metal-phosphate crosslinks increase modulus and strength

The formation of Ca^{2+}-phosphate crosslinks has been shown to significantly increase the modulus and toughness of pPEMA-pAAm hydrogels, which is dependent upon the quantity of available Ca^{2+} and thus number of added crosslinks. Caddisfly silk derives toughness from serial regions of Ca^{2+}-phosphate domains that viscously unravel upon strain followed by self-recovery of ruptured Ca^{2+}-phosphate bonds as directed by an elastic recoiling force. The inclusion of a sacrificial, self-recovering domain in combination with a permanent elastic network and high water content classify the caddisfly silk as a naturally occurring double network hydrogel material. This natural toughening mechanism has been replicated in the double network pPEMA-pAAm hydrogels with similar Ca^{2+}-phosphate domains coinciding with a covalently crosslinked elastic pAAm network. The initial modulus of the Ca^{2+} loaded hydrogels was highest at 0.8 +/- 0.07 MPa with the highest amount of loaded Ca^{2+} at 1.8 mol Ca^{2+}:OPO_3^{2-}. As the molar ratio of loaded Ca^{2+} to phosphate decreased from 1.8 to 0.1 the modulus decreased from 0.8 +/- 0.07 MPa to 0.01 +/- 0.001 MPa, corresponding to decreased Ca^{2+}-phosphate crosslinks (Figure 4.3C). The strength at 80% compression was 2.9 +/- 0.6, 2.6 +/- 0.7, 0.07 +/- 0.003, 0.05 +/- 0.001 MPa for Ca^{2+}:OPO_3^{2-} ratios of 1.8, 0.8, 0.3, 0.1 respectively (Figure 4.3F).

Like volume decrease, change in hydrogel initial modulus can also be used as a rough indication of quantity of crosslink formation. While a decrease in volume and increase in modulus indicate crosslink formation, the volume change and initial modulus do not correlate in exactly the same way. Volume was minimized around ~50% with only 0.8 Ca^{2+} per OPO_3^{2-},

however the initial modulus continued to increase with increasing Ca^{2+} up to 1.6 Ca^{2+} per OPO_3^{2-}. This may suggest there is some fraction of phosphates required for complete volume decrease upon crosslinking, which is less than the total number of possible crosslinks as evidenced by increased modulus and strength with increasing calcium after volume has reached steady state. Alternatively, there may be an optimization process where increased Ca^{2+} promotes reformation of transient Ca^{2+}-phosphate bonds leading to more stable complexes.

4.3.4 The effect of tobramycin crosslink formation on hydrogel mechanics

Inclusion of tobramycin crosslinks into Ca^{2+} loaded pPEMA-pAAm hydrogels reduces toughness by reducing the initial number of possible Ca^{2+} crosslinks and through an exchange process where some existing Ca^{2+} bonds are replaced by weaker tobramycin crosslinks. For hydrogels with a ratio of 1.8 and 0.8 Ca^{2+}:OPO_3^{2-}, the addition of tobramycin and corresponding reduction in Ca^{2+} OPO_3^{2-} crosslinks led to a decreased modulus from 0.8 +/- 0.07 to 0.7 +/- 0.2 MPa and 0.6 +/- 0.1 to 0.2 +/- 0.1 MPa, respectively (Figure 4.4A-E). Additionally there was a change in strength at 80% compression from 2.9 +/- 0.6 to 3.0 +/- 0.2 and 2.6 +/- 0.7 to 1.8 +/- 0.05 MPa respectively (Figure 4.4A,B,D-F). Previously the strength of metal-phosphate crosslinks was shown to be dependent on metal species identity; driven by changes in charge density, atomic radii, and coordination geometry between metals and phosphates where metals like Ca^{2+} were suspected of binding in an inner sphere mode and metals like Mg^{2+} with a high affinity for an inner sphere hydration shell bind phosphates in an outer sphere mode.[41] Tobramycin at 468 g/mol is >> than Ca^{2+} at 40 g/mol and results in a decrease in charge density resulting from the greater molecule size. Additionally the increased molecular size may result in less efficient crosslinking with less phosphates complexed compared to metals. Consequently, tobramycin

crosslinked hydrogels are weaker than Ca^{2+} crosslinked hydrogels as evidenced by the decrease in initial modulus and strength.

When the initial amount of loaded Ca^{2+} drops below 0.5 Ca^{2+}:OPO_3^{2-} tobramycin crosslink formation has a marginal toughening effect compared to unloaded pPEMA-pAAm hydrogels and resists fracture. For hydrogels loaded at lower ratios of 0.3 and 0.1 Ca^{2+}:OPO_3^{2-}, the addition of tobramycin results in an increased modulus from 0.03 +/- 0.01, and 0.01 +/- 0.001 to 0.09 +/- 0.02 and 0.04 +/- 0.01 MPa respectively (Figure 4.4C). This is a result of minimal Ca^{2+} crosslinking initially, thus the final mechanics of these hydrogels is driven by tobramycin crosslink formation instead of Ca^{2+}. In both cases (more Ca^{2+} crosslinks or more tobramycin crosslinks) the emergence of a double network structure comprising both electrostatic bonds and covalent crosslinks increases hydrogel toughness. Both Ca^{2+} and Ca^{2+}-tobramycin hydrogels resist fracture and do not fail when compressed to 80%. In contrast, primarily single network hydrogels with low calcium, 0.1 Ca^{2+}:OPO_3^{2-}, and no tobramycin fail prior to 80% compression (Figure 4.4E, blue curve).

4.3.5 Reversible phosphate crosslinks lead to recovery of modulus and hysteresis

Natural caddisfly silk strained in tension recovered close to 100% hysteresis area or energy dissipating potential after 120 m. The recovery behavior has been linked to rupture and reformation of electrostatic bonds between phosphate and divalent metal ions, which allow for beta-sheet protein structure to unravel and reform over multiple strain cycles. Double network pPEMA-pAAm hydrogels crosslinked with Ca^{2+} and tobramycin exhibit a recoverable reduction of modulus, energy dissipation, and strength at 80% compression over multiple compressive cycles (Figure 4.5A). The reduction in modulus, energy dissipation, and strength is 0.2 +/- 0.02, 0.1 +/-

0.01 and 0.6 +/- 0.02 MPa respectively between the 1st and 10th cycles. This is recovered by 113 +/- 10%, 108 +/- 7%, and 93 +/- 3% respectively over a 30 min dwell time (Figure 4.5B). The mechanical recovery mirrors observations from caddisfly silk and can be attributed to the transient nature of the Ca^{2+} or tobramycin OPO_3^{2-} crosslinks. In natural systems, like caddisfly silk, phosphate-Ca^{2+} complexes play a mechanical role and recoverability was linked to the reversible nature of the phosphate-metal complexes, which rupture upon strain and then spontaneously recover. Additionally, prior work with pPEMA-pAAm hydrogels loaded with Ca^{2+} demonstrated pseudo-yield behavior in tension as crosslinks were ruptured at a critical stress and reformed following strain as directed by an elastic restoring force. The hysteresis, shown in Figure 4.5A, is evidence of rupture of phosphate-Ca^{2+} bonds and associated energy dissipation. Progressive loss of hysteresis across multiple strains can be attributed to accumulating ruptured complexes with insufficient time for complete recovery between cycles. When the cycle dwell time is increased to 30 m, Figure 4.5B, recovery is near 100%. This shows that the recovery behavior of pPEMA-pAAM hydrogels is similar in compression compared to tests in tension and is dependent upon a transient crosslinked network of phosphate-metal complexes.

4.3.6 Sustained elution of tobramycin and vancomycin from tough double network hydrogels

Interactions between phosphates and tobramycin led to retention and sustained release of tobramycin for up to 66 days, Figure 4.6A. The tobramycin release rates were determined in a saline with Mg^{2+} and Ca^{2+} ions, the most abundant multivalent metal ions in blood and serum.[46] Ca^{2+} and tobramycin loaded pPEMA-pAAm hydrogel disks (250 µL volume) were incubated in 2 ml solutions of 130 mM NaCl plus 2.5 and 1.5 mM Ca^{2+} and Mg^{2+}, respectively, at pH 7.3. The solutions were replaced every 24 h and the tobramycin concentration in the solution was

determined using a colorimetric assay for primary amines. The pPEMA-pAAm hydrogels released 59 +/- 8.7 μg of tobramycin in the first 24 h (Figure 4.5B). The initial burst was likely due passive diffusion of unbound tobramycin entrapped in the hydrogel matrix. During the next 24 h, the rate of tobramycin release declined to 27.9 +/- 4.8 μg and then declined gradually to 0.1 +/- 0.5 μg mL^{-1} over 66 days (Figure 4.5B). The cumulative tobramycin release after 66 days was 1089 +/- 67 μg (Figure 4.5A). The sustained tobramycin release from the pPEMA-pAAm hydrogels has been speculated to be due to restricted diffusion of tobramycin, due to reversible electrostatic interactions with phosphate sidechains, or restricted diffusion due to hydrogel shrinkage, which resulted in decreased porosity of the hydrogel network. Furthermore, slow hydrolysis of the two ester linkages in the phosphate sidechains, and thus a degradation driven release, was not seen as a major contributor because the integrated intensity of ATR-FTIR spectra corresponding to the $P\text{-}O^-$ vibrational modes remained unchanged over 66 days, Figure 4.7. Additionally, the compressive modulus was 0.19 +/- 0.1 MPa after 8 weeks which was not statistically different ($P>0.9$) from hydrogels at week 1 (0.2 +/- 0.1 MPa) suggesting a constant quantity of phosphate-calcium crosslinks.

Total cumulative tobramycin release after 66 days was ~ 12% of the total tobramycin loaded into the hydrogels. Similarly low percentages of total release have been observed in other ionic systems. For example, a viscous gel of poly(allylamine hydrochloride) and inorganic polyphosphate released less than 3% of a charged drug proxy over 160 days.[21] In comparison, when pPEMA-pAAm hydrogels were previously loaded with only tobramycin the release of total drug was 5%. The difference in total drug released is not explained by tobramycin loading; 0.5 Ca^{2+}:OPO_3^{2-} tobramycin crosslinked hydrogels had lower total loaded drug 70 mg mL^{-1} versus 200 mg mL^{-1} in the tobramycin only loaded hydrogels. Additionally the total amounts of released tobramycin were similar, 1.089 mg for Ca^{2+}-tobramycin loaded hydrogels versus 0.75-1.25 mg

for tobramycin only loaded hydrogels, despite the difference in total loaded drug. This could be explained if tobramycin is released primarily from the surface resulting from accumulative electrostatic resistance to diffusion that may increase with hydrogel depth. By loading hydrogels in Ca^{2+} and inducing volume change before loading with tobramycin there may be an associated decrease in tobramycin loading in the center of the hydrogel but maintaining the total drug released from the surface.

In contrast to tobramycin loaded hydrogels, vancomycin loaded hydrogels did not exhibit the same prolonged release profile and are only usable in applications that would require a short vancomycin regimen of up to 5 days. The pPEMA-pAAm hydrogels released 560 +/- 11.1 μg of vancomycin in the first 24 h (Figure 4.6B). The daily release of vancomycin decreased to 0.2 +/- 0.2 μg ml^{-1} over 5 days (Figure 4.6B) with a cumulative vancomycin release of 730 +/- 17 μg. In comparison, a pAAm hydrogel loaded with tobramycin released 100% of its payload within 48 *h*.[4] In this case, an absence of phosphates in the hydrogel led to passive diffusion of the entire drug payload. While vancomycin has no net positive charge at pH 7.3 the release rate is twofold greater than diffusion of tobramycin from a pAAm hydrogel. It is possible that there are localized positive charges related to the two primary amine groups in the vancomycin structure, which interact with phosphates but are insufficient to extend release beyond 5 days. The increased size of vancomycin may also contribute to differences in charge distribution or density which may prevent crosslinking. Furthermore, vancomycin loaded hydrogels released 70% of the payload within 5 days illustrating some minimal level of electrostatic retention but not enough to produce dramatic hydrogel shrinking and retention of the drug.

A concern with antibiotic eluting materials and devices is that the antibiotic concentration could fall below the bactericidal concentration before the infection is completely

eradicated, creating an environment for selection of antibiotic resistance strains. While the *in vitro* elution conditions may not perfectly reflect *in vivo* conditions in tissues, the continuous release above 2 ug mL^{-1} for 60 days is greater than a previously determined bactericidal concentration for tobramycin against *P.aeruginosa*.[4] This prolonged elution as well as the large cumulative amount of tobramycin released, suggested the pPEMA-pAAm hydrogels can be capable of complete eradication of established infections *in vivo* before the release rate tails off, and therefore will have low potential for promoting development of bacterial drug resistance.

4.3.7 The effect of compression on tobramycin elution

Where pPEMA-pAAm hydrogels may be used as structural materials in joints compressive strains can effect the release behavior of tobramycin. Tobramycin loaded hydrogels were compressed to 50% at a rate of 6 cycles per min for 24 h increments. Over the first 24 h, tobramycin release increased from 59 +/- 8.7 ug mL^{-1} to 88.7 +/- 6.1 µg mL^{-1} with the addition of compressive cycles, Figure 4.8. Under cyclic compressive strain, tobramycin release through days 2-4 was increased by 6, 10, and 5 µg per day, Figure 4.8. Compressive strain could increase tobramycin release in multiple ways. One, strain induced rupture of phosphate tobramycin crosslinks could result in an increase of the population of tobramycin bound to only a single phosphate and thus rise the rate at which tobramycin diffuses out of the hydrogel. Two, compressive cycles force additional fluid flow both in and out of the hydrogel structure which can result in transportation of tobramycin due to the introduction of a flow rate which is faster than passive diffusion. While compressive cycles led to an increase in daily tobramycin release the increase was not great enough to deplete the loaded tobramycin reserve in a way that would shorten the duration of tobramycin release.

4.4 Conclusions

The polyphosphate hydrogels used a network dense in phosphates as a dual mechanism for toughening with Ca^{2+} crosslinks and sustaining tobramycin release for over 60 days via electrostatically reduced diffusion rates and could be useful as orthopedic materials for both fighting infection and structural components. In orthopedic applications antibiotics are chosen to have broad spectrum effectiveness and limited resistant strains. Tobramycin and gentamycin are the most commonly used gram negative antibiotics and vancomycin for gram positive.[58] Orthopedic materials often include calcium-phosphate matrices such as hydroxyapatite,[54] biphasic calcium phosphate[59,60] and calcium polyphosphate powders[54] paired with vancomycin to create bone replacement materials while fighting infection. In these cases the calcium-phosphate matrix are ceramic or dense putty and release of antibiotic is driven by diffusion and degradation of the matrix with sustained release for only a few days. Bone fillers and antibiotic impregnated bone cements have also been deployed as a preventative measures in joint replacement. An inorganic bone filler ProOsteon 500R has been mixed with polycaprolactone, polyethylene glycol, poly(D,L-lactide-co-glycolide), and tobramycin to form a moldable composite bone void filler with sustained release of tobramycin for over 20 days.[61] Gentamycin and tobramycin loaded cements like Palacos-R or Simplex-P have been formed into spacers via injection molding for use as a high dose prophylaxis during joint replacement and were demonstrated to release for up to 1 week.[62] Simplex-P cement loaded with tobramycin was shown to be effective against 99 strains representative of orthopedic infection including both gram positive, gram negative and strains resistant to systemic levels of tobramycin.[63] Previously, similar polyphosphate hydrogels loaded with only tobramycin were shown to totally eradicate *P.aeruginosa* biofilms *in vitro* within 72 h and were capable to maintaining zones of inhibition against *P.aeruginosa* for 4 weeks.[4] While polyphosphate hydrogels are probably not realistic

complete replacements for bone substitute materials that are replaced over time by natural bone, they could be included as a bone patch or mixed in as particles to extend the release of tobramycin.

A more obvious application for tough, tobramycin releasing polyphosphate hydrogels is as a spacer or artificial cartilage layer in total joint replacement surgery. In addition to localized sustained antibiotic elution the reported hydrogels mechanically demonstrated potential as structural components in joint replacement. Articular knee cartilage acts as a load distributer with normal loads ranging between 1-3 body weights depending on gait and cartilage location, proximal or distal and medial or lateral.[64,65] Loads were normalized by dividing by the average normal knee contact surface area.[66] As a result, cartilage or meniscus replacement materials should be capable of distributing forces of 1-2 MPa, this is in agreement with a similar published benchmark by J.P. Gong.[67] pPEMA-pAAm hydrogels loaded with Ca^{2+} and tobramycin were capable to withstanding several MPa loads by 80% compression without failure. The modulus of articular cartilage ranges from 6 to 14 MPa,[68,69] while the reported 0.5 Ca^{2+}:OPO^{2-} hydrogel had a modulus of 0.2 MPa. Previous work showed an increase in modulus for pPEMA-pAAm hydrogels from 10 MPa to 34 MPa by replacing Ca^{2+} with Zn^{2+}, which could be explored in future work.[41] Aditionally, the loading and release mechanism is unique, as mechanical manipulation of the material can alter the release behavior and expand the possible uses of pPEMA-pAAM hydrogels as a strain induced drug releasing material.

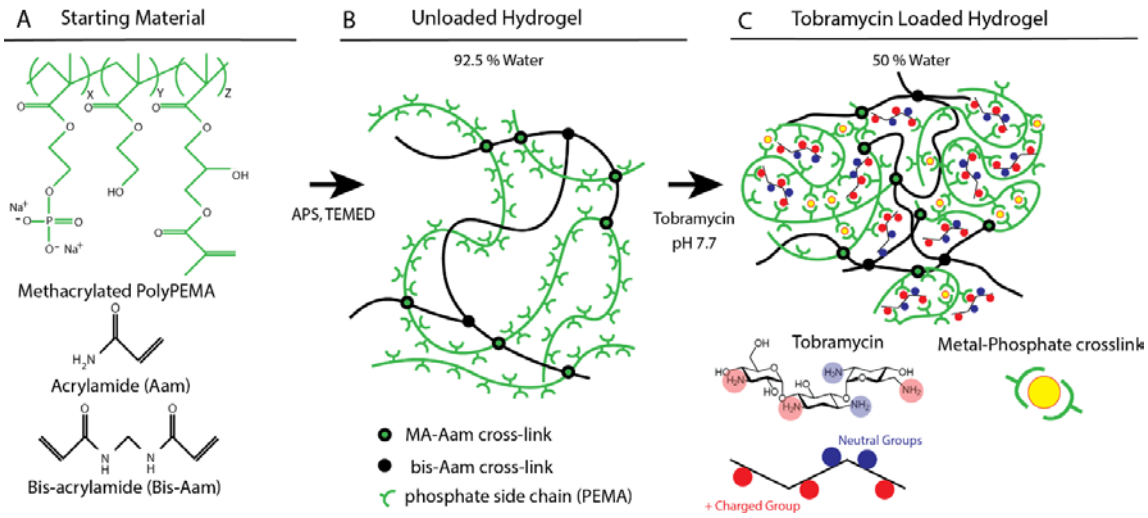

Figure 4.1: Schematic diagram of the synthesis and loading of pPEMA-pAAm tobramycin double network hydrogels: A) Structure of pPEMA-MA, acrylamide and bis-acrylamide. B) Double network structure after copolymerization of pPEMA and pAAm. C) Collapse of the polyphosphate network and expulsion of water due to electrostatic crosslinking of phosphates by Ca^{2+} and tobramycin.

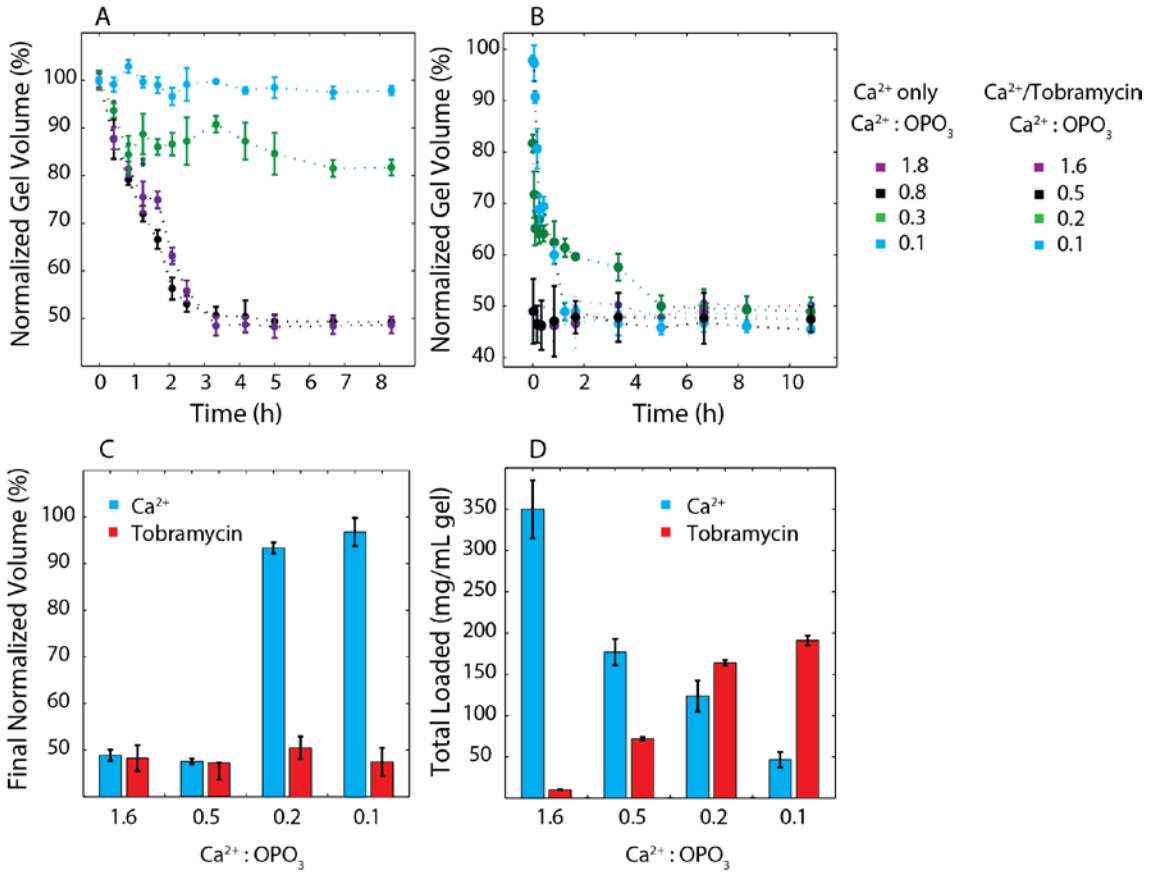

Figure 4.2: Loading of Ca^{2+} and tobramycin and associated volume change. A) Normalized volume change with addition of Ca^{2+} at ratios of 1.8 (Purple), 0.8 (black), 0.3 (green) and 0.1 (blue) Ca^{2+} to OPO_3^{2-}. B) Post Ca2+ addition of tobramycin results in further volume change and final Ca^{2+} to OPO_3^{2-} ratios of 1.6 (purple), 0.5 (black), 0.2 (green) and 0.1 (blue). C) Final normalized volumes with Ca^{2+} (blue) and after tobramycin loading (red). D) Total loaded cation in mg per ml of hydrogel, Ca^{2+} (blue), Tobramycin (red). Error bars are +/- 1 S.D. with n=3.

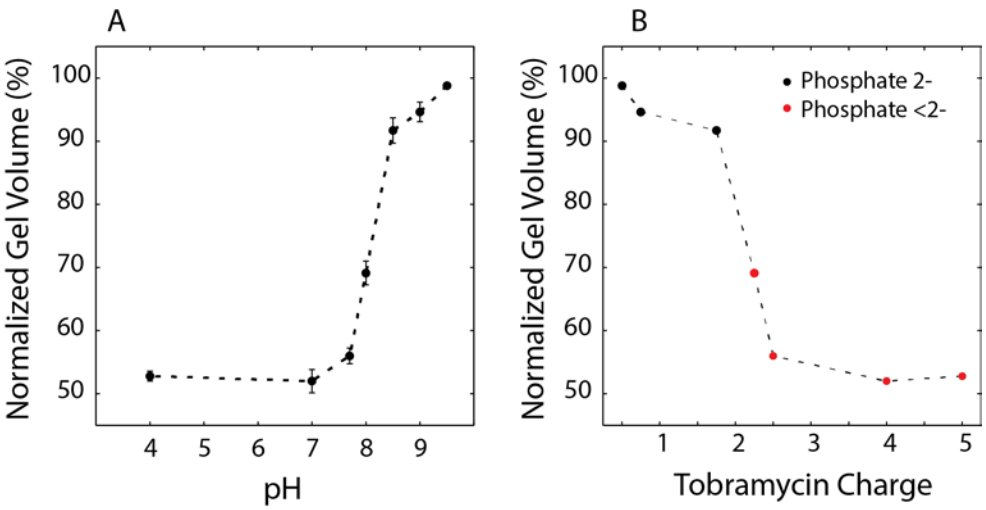

Figure 4.3: Normalized hydrogel volume reduction resulting from tobramycin loading A) Normalized gel volume reduction resulting from tobramycin loading is dependent upon pH. B) pH changes affect total charge on tobramycin (x axis) and charge on phosphate (red = less than -2 and black = -2) and affects hydrogel volume.

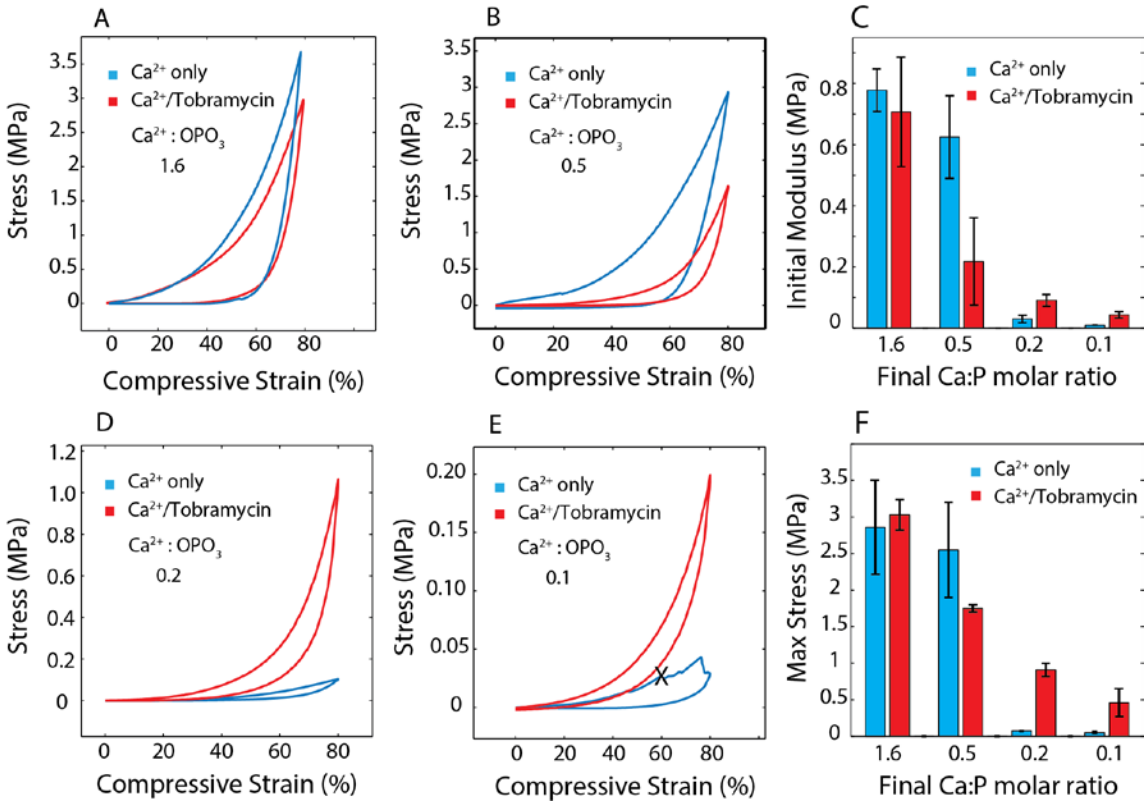

Figure 4.4: Representative stress strain curves for pPEMA-pAAm hydrogels with Ca^{2+} (blue) and after tobramycin loading (red). A) Final ratio of 1.6 Ca^{2+}:OPO_3^{2-}. B) Final ratio of 0.5. D) Final ratio of 0.2. E) Final ratio of 1.6. C) Comparison of initial modulus for hydrogels loaded with Ca^{2+} (blue) and after tobramycin loading (red) for all final ratios of Ca^{2+}:OPO_3^{2-}. F) Strength at 80% compression for hydrogels loaded with Ca^{2+} (blue) and after tobramycin loading (red). Error bars are +/- 1 S.D. with n=3, X symbol represents initial point of mechanical failure.

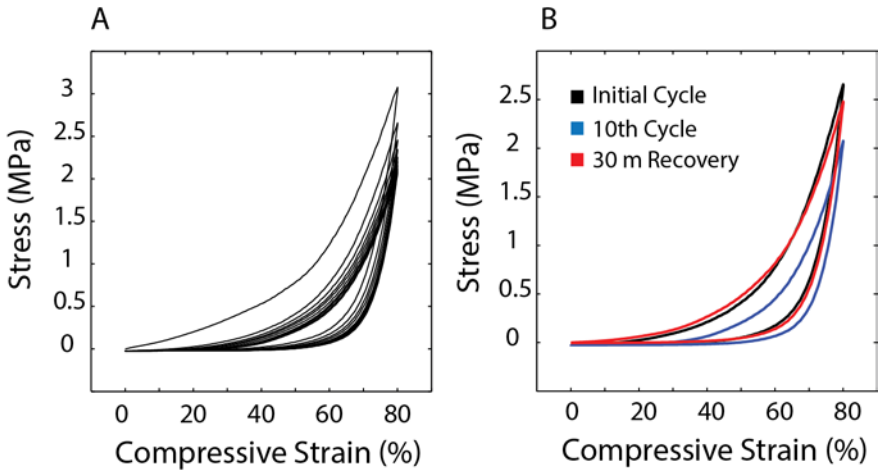

Figure 4.5: Recovery of mechanics following multiple cyclical compressive strains. A) Representative series of 10 compressive cycles of a pPEMA-pAAM hydrogeld loaded with 0.5 Ca^{2+}:OPO_3^{2-} and tobramycin. B) Representative stress strain curves showing the 2nd compressive cycle (black) excluding the first cycle as a conditioning step, and 10th cycle (blue) and subsequent cycle following a 30 min dwell time (red). Recovery of modulus, hysteresis, and strength is ~100% at 30 m.

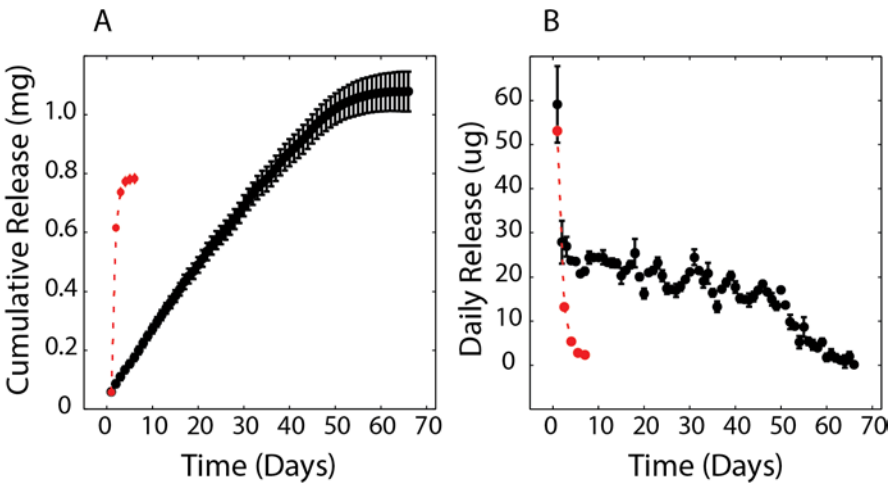

Figure 4.6: Controlled release of vancomycin or tobramycin from pPEMA-pAAm hydrogels loaded with 0.5 Ca^{2+}:OPO_3^{2-}. A) Cumulative release of tobramycin (black) and vancomycin (red). B) Daily tobramycin release (black), and vancomycin release (red). Error bars are +/- 1 S.D. with n=3.

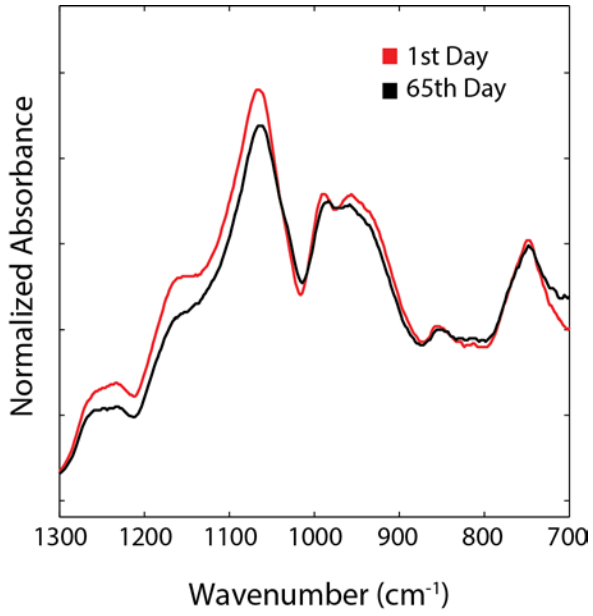

Figure 4.7: Normalized ATR-FTIR spectra in the region corresponding to P–O^- vibrational modes of Ca^{2+} and Tobramycin equilibrated pPEMA-pAAm hydrogels. The initial spectra for hydrogels is shown in red and then the spectra is retaken after 65 days in 130 mM NaCl, 2.5 mM Ca^{2+}, and 1.5 mM Mg^{2+} at pH 7.3. Spectra curves are representative and there was no statistical significance (P>0.9) between the integrated intensity of the area between 875 and 1025 cm^{-1}.

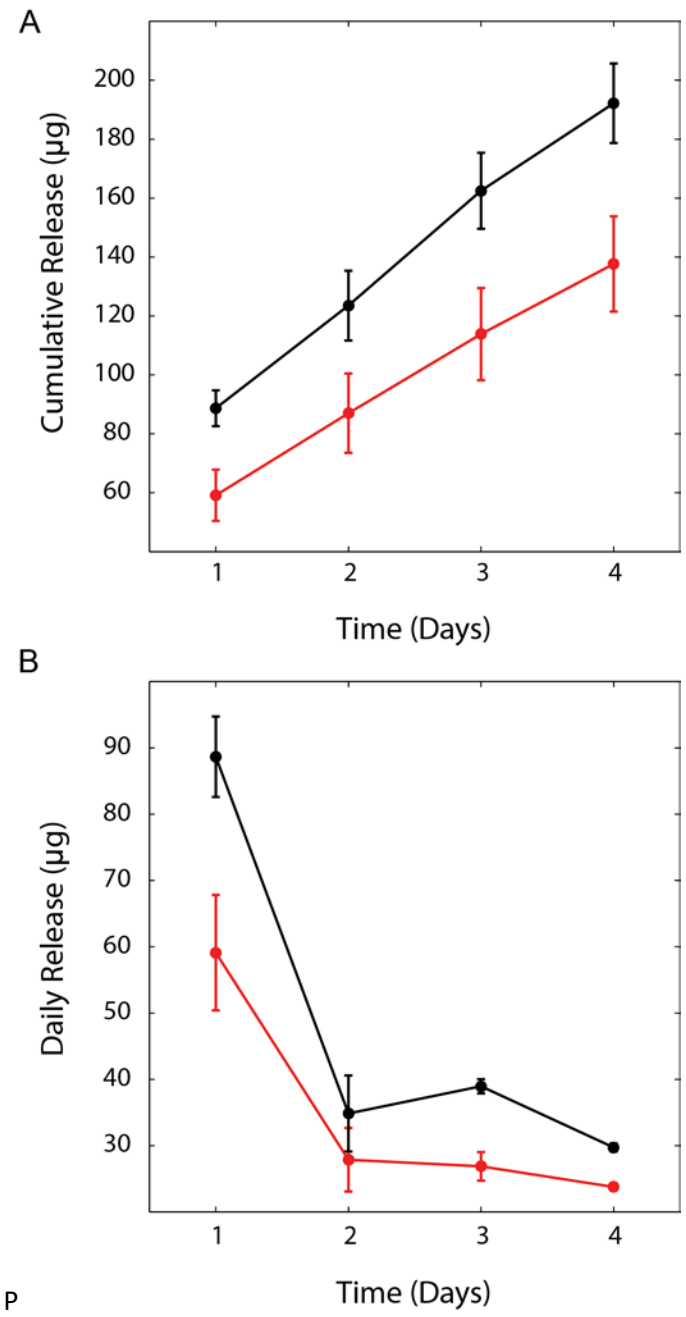

P

Figure 4.8: Effect of compression on tobramycin release A) Cumulative release of tobramycin from pPEMA-pAAm hydrogels B) Daily release of tobramycin from pPEMA-pAAm hydrogels. Hydrogels under cyclic compression are shown in black and control hydrogels with under zero strain are in red. n=3 and error bars are +/- 1 S.D.

4.5 References

(1) Caló, E.; Khutoryanskiy, V. V. Biomedical Applications of Hydrogels: A Review of Patents and Commercial Products. *Eur. Polym. J.* **2015**, *65*, 252–267 DOI: 10.1016/j.eurpolymj.2014.11.024.

(2) Hoare, T. R.; Kohane, D. S. Hydrogels in Drug Delivery: Progress and Challenges. *Polymer*. Elsevier Ltd 2008, pp 1993–2007.

(3) Buwalda, S. J.; Boere, K. W. M.; Dijkstra, P. J.; Feijen, J.; Vermonden, T.; Hennink, W. E. Hydrogels in a Historical Perspective: From Simple Networks to Smart Materials. *J. Control. Release* **2014**, *190*, 254–273 DOI: 10.1016/j.jconrel.2014.03.052.

(4) Lane, D. D.; Fessler, A. K.; Goo, S.; Williams, D. L.; Stewart, R. J. Sustained Tobramycin Release from Polyphosphate Double Network Hydrogels. *Acta Biomater.* **2016**, *50*, 1–9 DOI: 10.1016/j.actbio.2016.12.030.

(5) Bhattarai, N.; Gunn, J.; Zhang, M. Chitosan-Based Hydrogels for Controlled, Localized Drug Delivery. *Adv. Drug Deliv. Rev.* **2010**, *62* (1), 83–99 DOI: 10.1016/j.addr.2009.07.019.

(6) Hoare, T. R.; Kohane, D. S. Hydrogels in Drug Delivery : Progress and Challenges *. *Polymer (Guildf).* **2008**, *49* (8), 1993–2007 DOI: 10.1016/j.polymer.2008.01.027.

(7) Schoenmakers, R. G.; Van De Wetering, P.; Elbert, D. L.; Hubbell, J. A. The Effect of the Linker on the Hydrolysis Rate of Drug-Linked Ester Bonds. *J. Control. Release* **2004**, *95* (2), 291–300 DOI: 10.1016/j.jconrel.2003.12.009.

(8) Kwok, C. S.; Horbett, T. A.; Ratner, B. D. Design of Infection-Resistant Antibiotic-Releasing polymersII. Controlled Release of Antibiotics through a Plasma-Deposited Thin Film Barrier. *J. Control. Release* **1999**, *62* (3), 301–311 DOI: 10.1016/S0168-3659(99)00105-4.

(9) Matsusaki, M.; Sakaguchi, H.; Serizawa, T.; Akashi, M. Controlled Release of Vascular Endothelial Growth Factor from Alginate Hydrogels Nano-Coated with Polyelectrolyte Multilayer Films. *J. Biomater. Sci. Polym. Ed.* **2007**, *18* (6), 775–783 DOI: 10.1163/156856207781034160.

(10) Yeo, Y.; Ito, T.; Bellas, E.; Highley, C. B.; Marini, R.; Kohane, D. S. In Situ Cross-Linkable Hyaluronan Hydrogels Containing Polymeric Nanoparticles for Preventing Postsurgical Adhesions. *Ann. Surg.* **2007**, *245* (5), 819–824 DOI: 10.1097/01.sla.0000251519.49405.55.

(11) Nuttelman, C. R.; Tripodi, M. C.; Anseth, K. S. Dexamethasone-Functionalized Gels Induce Osteogenic Differentiation of Encapsulated hMSCs. *J. Biomed. Mater. Res. - Part A* **2006**, *76* (1), 183–195 DOI: 10.1002/jbm.a.30537.

(12) Nakamae, K.; Nishino, T.; Kato, K.; Miyata, T.; Hoffman, A. S. Synthesis and Characterization of Stimuli-Sensitive Hydrogels Having a Different Length of Ethylene Glycol Chains Carrying Phosphate Groups: Loading and Release of Lysozyme. *J. Biomater. Sci. Polym. Ed.* **2004**, *15* (11), 1435–1446 DOI: 10.1163/1568562042368095.

(13) Feeney, M.; Giannuzzo, M.; Paolicelli, P.; Casadei, M. A. Hydrogels of Dextran Containing Nonsteroidal Anti-Inflammatory Drugs as Pendant Agents. *Drug Deliv.* **2007**, *14* (2), 87–93 DOI: 10.1080/10717540600740003.

(14) Qiu, Y.; Park, K. Environment-Sensitive Hydrogels for Drug Delivery. *Adv. Drug Deliv. Rev.* **2012**, *64* (SUPPL.), 49–60 DOI: 10.1016/j.addr.2012.09.024.

(15) Sato, T.; Uchida, R.; Tanigawa, H.; Uno, K.; Murakami, A. Application of Polymer Gels Containing Side-Chain Phosphate Groups to Drug-Delivery Contact Lenses. *J. Appl. Polym. Sci.* **2005**, *98* (2), 731–735 DOI: 10.1002/app.22080.

(16) Nakamae, K.; Nishino, T.; Kato, K. Synthesis and Characterization of Stimuli-Sensitive Hydrogels Having a Different Length of Ethylene Glycol Chains Carrying Phosphate Groups : Loading and Release of Lysozyme. *J. Biomater. Sci. Polym. Ed.* **2004**, *15* (11), 1435–1446.

(17) Andrade-vivero, P.; Fernandez-gabriel, E.; Alvarez-lorenzo, C.; Concheiro, A. Improving the Loading and Release of NSAIDs from pHEMA Hydrogels by Copolymerization with Functionalized Monomers. *J. Pharm. Sci.* **2007**, *96* (4), 802–813 DOI: 10.1002/jps.

(18) Coviello, T.; Matricardi, P.; Marianecci, C.; Alhaique, F. Polysaccharide Hydrogels for Modified Release Formulations. *J. Control. Release* **2007**, *119* (1), 5–24 DOI: 10.1016/j.jconrel.2007.01.004.

(19) Chuang, H. F.; Smith, R. C.; Hammond, P. T. Polyelectrolyte Multilayers for Tunable Release of Antibiotics. *Biomacromolecules* **2008**, *9* (6), 1660–1668 DOI: 10.1021/bm800185h.

(20) Moskowitz, J. S.; Blaisse, M. R.; Samuel, R. E.; Hsu, H. P.; Harris, M. B.; Martin, S. D.; Lee, J. C.; Spector, M.; Hammond, P. T. The Effectiveness of the Controlled Release of Gentamicin from Polyelectrolyte Multilayers in the Treatment of Staphylococcus Aureus Infection in a Rabbit Bone Model. *Biomaterials* **2010**, *31* (23), 6019–6030 DOI: 10.1016/j.biomaterials.2010.04.011.

(21) Lawrence, P. G.; Patil, P. S.; Leipzig, N. D.; Lapitsky, Y. Ionically Cross-Linked Polymer Networks for the Multiple-Month Release of Small Molecules. *ACS Appl. Mater. Interfaces* **2016**, *8* (7), 4323–4335 DOI: 10.1021/acsami.5b10070.

(22) Costerton, J. W. Biofilm Theory Can Guide the Treatment of Device-Related Orthopaedic Infections. *Clin. Orthop. Relat. Res.* **2005**, *437*, 7–11 DOI: 10.1097/01.blo.0000175128.44966.d9.

(23) Gong, J. P.; Katsuyama, Y.; Kurokawa, T.; Osada, Y. Double-Network Hydrogels with Extremely High Mechanical Strength. *Adv. Mater.* **2003**, *15* (14), 1155–1158 DOI: 10.1002/adma.200304907.

(24) Chen, Q.; Zhu, L.; Zhao, C.; Wang, Q.; Zheng, J. A Robust, One-Pot Synthesis of Highly Mechanical and Recoverable Double Network Hydrogels Using Thermoreversible Sol-Gel Polysaccharide. *Adv. Mater.* **2013**, *25* (30), 4171–4176 DOI: 10.1002/adma.201300817.

(25) Myung, D.; Koh, W.; Ko, J.; Hu, Y.; Carrasco, M.; Noolandi, J.; Ta, C. N.; Frank, C. W. Biomimetic Strain Hardening in Interpenetrating Polymer Network Hydrogels. *Polymer (Guildf).* **2007**, *48* (18), 5376–5387 DOI: 10.1016/j.polymer.2007.06.070.

(26) Haque, M. A.; Kurokawa, T.; Kamita, G.; Gong, J. P. Lamellar Bilayers as Reversible Sacrificial Bonds To Toughen Hydrogel: Hysteresis, Self-Recovery, Fatigue Resistance, and Crack Blunting. *Macromolecules* **2011**, *44* (22), 8916–8924 DOI: 10.1021/ma201653t.

(27) Bai, T.; Zhang, P.; Han, Y.; Liu, Y.; Liu, W.; Zhao, X.; Lu, W. Construction of an Ultrahigh Strength Hydrogel with Excellent Fatigue Resistance Based on Strong Dipole–dipole Interaction. *Soft Matter* **2011**, *7* (6), 2825 DOI: 10.1039/c0sm01108h.

(28) Sun, T. L.; Kurokawa, T.; Kuroda, S.; Ihsan, A. Bin; Akasaki, T.; Sato, K.; Haque, M. A.; Nakajima, T.; Gong, J. P. Physical Hydrogels Composed of Polyampholytes Demonstrate High Toughness and Viscoelasticity. *Nat. Mater.* **2013**, *12* (10), 932–937 DOI: 10.1038/nmat3713.

(29) Kersey, F. R.; Loveless, D. M.; Craig, S. L. A Hybrid Polymer Gel with Controlled Rates of Cross-Link Rupture and Self-Repair. *J. R. Soc. Interface* **2007**, *4* (13), 373–380 DOI: 10.1098/rsif.2006.0187.

(30) Henderson, K. J.; Zhou, T. C.; Otim, K. J.; Shull, K. R. Ionically Cross-Linked Triblock Copolymer Hydrogels with High Strength. *Macromolecules* **2010**, *43* (14), 6193–6201 DOI: 10.1021/ma100963m.

(31) Sun, J.-Y.; Zhao, X.; Illeperuma, W. R. K.; Chaudhuri, O.; Oh, K. H.; Mooney, D. J.; Vlassak, J. J.; Suo, Z. Highly Stretchable and Tough Hydrogels. *Nature* **2012**, *489* (7414), 133–136 DOI: 10.1038/nature11409.

(32) Zhang, L.; Zhao, J.; Zhu, J.; He, C.; Wang, H. Anisotropic Tough Poly(vinyl Alcohol) Hydrogels. *Soft Matter* **2012**, *8* (40), 10439 DOI: 10.1039/c2sm26102b.

(33) Lin, W.-C.; Fan, W.; Marcellan, A.; Hourdet, D.; Creton, C. Large Strain and Fracture Properties of Poly(dimethylacrylamide)/Silica Hybrid Hydrogels. *Macromolecules* **2010**, *43*, 2554–2563 DOI: 10.1021/ma901937r.

(34) Wiggins, G. B. *Caddisflies: The Underwater Architects*; University of Toronto Press: Toronto, 2004.

(35) Stewart, R. J.; Wang, C. S. Adaptation of Caddisfly Larval Silks to Aquatic Habitats by Phosphorylation of H-Fibroin Serines. *Biomacromolecules* **2010**, *11* (4), 969–974 DOI: 10.1021/bm901426d.

(36) Ashton, N. N.; Stewart, R. J. Self-Recovering Caddisfly Silk: Energy Dissipating, Ca(2+)-Dependent, Double Dynamic Network Fibers. *Soft Matter* **2014** DOI: 10.1039/c4sm02435d.

(37) Ashton, N. N.; Roe, D. R.; Weiss, R. B.; Cheatham, T. E.; Stewart, R. J. Self-Tensioning Aquatic Caddisfly Silk: Ca2+-Dependent Structure, Strength, and Load Cycle Hysteresis.

Biomacromolecules **2013**, *14* (10), 3668–3681 DOI: 10.1021/bm401036z.

(38) Ashton, N. N.; Pan, H.; Stewart, R. J.; Stewart, R. J. Connecting Caddisworm Silk Structure and Mechanical Properties : Combined Infrared Spectroscopy and Mechanical Analysis. *Open Biol.* **2016**, *6*.

(39) Degtyar, E.; Harrington, M. J.; Politi, Y.; Fratzl, P. The Mechanical Role of Metal Ions in Biogenic Protein-Based Materials. *Angew. Chem. Int. Ed. Engl.* **2014**, *53* (45), 12026–12044 DOI: 10.1002/anie.201404272.

(40) Shao, H.; Bachus, K. N.; Stewart, R. J. A Water-Borne Adhesive Modeled after the Sandcastle Glue of P. Californica. *Macromol. Biosci.* **2009**, *9* (5), 464–471 DOI: 10.1002/mabi.200800252.

(41) Lane, D. D.; Kaur, S.; Weerasakare, G. M.; Stewart, R. J. Toughened Hydrogels Inspired by Aquatic Caddisworm Silk. *Soft Matter* **2015**, *11*, 6981–6990 DOI: 10.1039/C5SM01297J.

(42) Shao, H.; Weerasekare, G. M.; Stewart, R. J. Controlled Curing of Adhesive Complex Coacervates with Reversible Periodate Carbohydrate Complexes. *J. Biomed. Mater. Res. A* **2011**, *97* (1), 46–51 DOI: 10.1002/jbm.a.33026.

(43) Marshall, Thomas and Williams, K. Elimination of the Interference from Aminoglycoside Antibiotics in the Pyrogallol Red-Molybdate Protein Dye-Binding Assay,. *Clin. Chem.* **2004**, *50* (9), 1674–1675 DOI: 10.1373/clinchem.2004.033548.

(44) Yip, S. P.; Wong, M. L. Aminoglycoside Interference in the Pyrogallol Red-Molybdate Protein Assay Is Increased by the Addition of Sodium Dodecyl Sulfate to the Dye Reagent. *Clin. Chem.* **2003**, *49* (12), 2111–2112 DOI: 10.1373/clinchem.2003.023622.

(45) Bernard, S. An Improved Pyrogallol Red-Molybdate for Determining Total Urinary Protein. *Clin. Chem.* **1989**, *35* (11), 2233–2236.

(46) Marques, M. R. C.; Loebenberg, R.; Almukainzi, M. Simulated Biological Fluids with Possible Application in Dissolution Testing. *Dissolution Technol.* **2011**, No. August, 15–28.

(47) Stuart, B. *Infrared Spectroscopy: Fundamentals and Applications*; John Wiley & Sons: Hoboken,NJ, 2004.

(48) Sanchez-Ruiz, J. M.; Martinez-Carrion, M. A Fourier-Transform Infrared Spectroscopic Study of the Phosphoserine Residues in Hen Egg Phosvitin and Ovalbumin. *Biochemistry* **1988**, *27* (9), 3338–3342 DOI: 10.1021/bi00409a033.

(49) Fernández, C.; Ausar, S. F.; Badini, R. G.; Castagna, L. F.; Bianco, I. D.; Beltramo, D. M. An FTIR Spectroscopy Study of the Interaction between α S-Casein-Bound Phosphoryl Groups and Chitosan. *Int. Dairy J.* **2003**, *13* (11), 897–901 DOI: 10.1016/S0958-6946(03)00115-8.

(50) DiCicco, M.; Duong, T.; Chu, A.; Jansen, S. A. Tobramycin and Gentamycin Elution Analysis between Two in Situ Polymerizable Orthopedic Composites. *J. Biomed. Mater. Res. B.*

Appl. Biomater. **2003**, *65* (1), 137–149 DOI: 10.1002/jbm.b.10528.

(51) Diekema, D. J.; BootsMiller, B. J.; Vaughn, T. E.; Woolson, R. F.; Yankey, J. W.; Ernst, E. J.; Flach, S. D.; Ward, M. M.; Franciscus, C. L.; Pfaller, M. A.; Doebbeling, B. N. Antimicrobial Resistance Trends and Outbreak Frequency in United States Hospitals. *Clin.Infect.Dis.* **2004**, *38* (1537–6591 (Electronic)), 78–85 DOI: 10.1086/380457.

(52) Moran, E.; Masters, S.; Berendt, A. R.; McLardy-Smith, P.; Byren, I.; Atkins, B. L. Guiding Empirical Antibiotic Therapy in Orthopaedics: The Microbiology of Prosthetic Joint Infection Managed by Debridement, Irrigation and Prosthesis Retention. *J. Infect.* **2007**, *55* (1), 1–7 DOI: 10.1016/j.jinf.2007.01.007.

(53) Sponseller, P. D.; LaPorte, D. M.; Hungerford, M. W.; Eck, K.; Bridwell, K. H.; Lenke, L. G. Deep Wound Infections after Neuromuscular Scoliosis Surgery: A Multicenter Study of Risk Factors and Treatment Outcomes. *Spine (Phila. Pa. 1976).* **2000**, *25* (19), 2461–2466 DOI: 10.1097/00007632-200010010-00007.

(54) Dion, A.; Langman, M.; Hall, G.; Filiaggi, M. Vancomycin Release Behaviour from Amorphous Calcium Polyphosphate Matrices Intended for Osteomyelitis Treatment. *Biomaterials* **2005**, *26*, 7276–7285 DOI: 10.1016/j.biomaterials.2005.05.072.

(55) Kanj, W. W.; Flynn, J. M.; Spiegel, D. A.; Dormans, J. P.; Baldwin, K. D. Vancomycin Prophylaxis of Surgical Site Infection in Clean Orthopedic Surgery. *Orthopedics* **2013**, *36* (2), 138–146 DOI: 10.3928/01477447-20130122-10.

(56) Walter, F.; Vicens, Q.; Westhof, E. Aminoglycoside - RNA Interactions. *Curr. Opin. Chem. Biol.* **1999**, *3*, 694–704 DOI: 10.1016/S1367-5931(99)00028-9.

(57) Pfeiffer, R. R. Structural Features of Vancomycin. *Rev. Infect. Dis.* **1981**, *3*, S205–S209.

(58) Bistolfi, A.; Massazza, G.; Verné, E.; Massè, A.; Deledda, D.; Ferraris, S.; Miola, M.; Galetto, F.; Crova, M. Antibiotic-Loaded Cement in Orthopedic Surgery: A Review. *ISRN Orthop.* **2011**, *2011*, 1–8 DOI: 10.5402/2011/290851.

(59) Gautier, H.; Daculsi, G.; Merle, C. Association of Vancomycin and Calcium Phosphate by Dynamic Compaction : In Vitro Characterization and Microbiological Activity. *Biomaterials* **2001**, *22* (92), 2481–2487.

(60) Gautier, H.; Merle, C.; Auget, J. L.; Daculsi, G. Isostatic Compression , a New Process for Incorporating Vancomycin into Biphasic Calcium Phosphate : Comparison with a Classical Method. **2000**, *21*, 243–249.

(61) Brooks, B. D.; Sinclair, K. D.; Davidoff, S. N.; Lawson, S.; Williams, A. G.; Coats, B.; Grainger, D. W.; Brooks, A. E. Molded Polymer-Coated Composite Bone Void Filler Improves Tobramycin Controlled Release Kinetics. *J. Biomed. Mater. Res. B Appl. Biomater.* **2013**, *102B* (5), 1074–1083 DOI: 10.1002/jbm.b.33089.

(62) Moojen, D. J. F.; Hentenaar, B.; Vogely, H. C.; Verbout, A. J.; Castelein, R. M.; Dhert, W. J. A. In Vitro Release of Antibiotics from Commercial PMMA Beads and Articulating Hip

Spacers. *J. Arthroplasty* **2008**, *23* (8), 1152–1156 DOI: 10.1016/j.arth.2007.08.020.

(63) Scott, C. P.; Higham, P. A.; Dumbleton, J. H. Effectiveness of Bone Cement Containing Tobramycin in an Vitro Susceptibility Study of 99 Organisms Found in Infected Joint Arthroplasty. *J Bone Jt. Surg [Br]* **1999**, *81*, 440–443.

(64) Hurwitz, D. E.; Sumner, D. R.; Andriacchi, T. P.; Sugar, D. A. Dynamic Knee Loads during Gait Predict Proximal Tibial Bone Distribution. **1998**, *31*, 423–430.

(65) Winby, C. R.; Lloyd, D. G.; Besier, T. F.; Kirk, T. B. Muscle and External Load Contribution to Knee Joint Contact Loads during Normal Gait. *J. Biomech.* **2009**, *42* (14), 2294–2300 DOI: 10.1016/j.jbiomech.2009.06.019.

(66) Fukubayashi, T.; Kurosawa, H. The Contact Area and Pressure Distribution Pattern of the Knee : A Study of Normal and Osteoarthrotic Knee Joints. *Acta Orthop. Scand.* **1980**, *51*, 871–879 DOI: 10.3109/17453678008990887.

(67) Gong, J. P. Why Are Double Network Hydrogels so Tough ? *Soft Matter* **2010**, *6*, 2583–2590 DOI: 10.1039/b924290b.

(68) Barker, M. K.; Seedhom, B. B. The Relationship of the Compressive Modulus of Articular Cartilage with Its Deformation Response to Cyclic Loading : Does Cartilage Optimize Its Modulus so as to Minimize the Strains Arising in It due to the Prevalent Loading Regime ? *Rheumatology* **2001**, *40*, 274–284.

(69) Shepherd, D. E. T.; Seedhom, B. B. The “instantaneous” Compressive Modulus of Human Articular Cartilage in Joints of the Lower Limb. *Rheumatology* **1999**, *38*, 124–132.

CHAPTER 5

EMULSION OF POLYPHOSPHATE- TOBRAMYCIN COMPLEX COACERVATES FOR PULMONARY DELIVERY OF AMINOGLYCOSIDES TO TREAT CHRONIC INFECTION IN CYSTICFIBROSIS

5.1 Introduction

5.1.1 Cystic fibrosis leads to chronic pulmonary infection

Cystic Fibrosis (CF) is a life shortening genetic disease with significant adverse effects to the lungs including irregular mucus secretions and increased risk for infection.[1] Mutation occurs in the cystic fibrosis transmembrane conductance regulator (CFTR) gene leading to abnormal CFTR protein. This abnormality results in ineffective ion transport across epithelial mucosal cells leading to salt and water imbalance and consequently more viscous sticky mucus excretions.[2–5] Associated complications include: liver disease, pancreatic insufficiency, diabetes, and chronic lung infection, the leading cause of CF related death.[1,6,7]

The effect on the lungs is profound and disrupts normal lung immune response. The principal cause of reduced pulmonary immune response is complex and derives from multiple sources. Because mucus cannot be easily cleared from the airways, it provides an ideal niche for invasion of opportunistic bacteria. There is a link between the lack of CFTR protein and associated decrease in secretion of HCO_3^-, which in the presence of continued proton release results in lower pH or acidification of the surface airway liquid.[8] This acidification has been

suggested as an critical factor for explaining reduced effectiveness of the host immune system.[8] The combination of lack of mucosal clearance, surface airway acidification and formation of biofilms illustrates the complex environment that has resulted in chronic airway infection in cystic fibrosis.

Most CF patients experience some form of acute infection with gram-negative *Pseudomonas aeruginosa* most common. These initial infections eventually progresses into chronic biofilm based infection in almost all cases.[9] Despite extensive research and clinical efforts to eradicate chronic infection in CF patients, there is currently no successful solution for eradicating chronic *P. aeruginosa* infection.[9–11]

5.1.2 Biofilms reduce the effectiveness of current chemotherapies

Biofilms are an exopolysaccharide matrix secreted by adhered bacterial cells that increases antibiotic resistance by up to 1000 fold.[12–14] The complex biofilm structure includes large plumes and channels, hypothesized to transport nutrients throughout the biofilm and potentially transporting antimicrobials away, both of which improve surviability.[15] Furthermore, even after successful infection eradication these complex biofilm structures may be vacant but still intact, thus facilitating an external reseeding event by new pathogen invaders. This could be a potential explanation for why acute infection in younger CF patients eventually transitions into chronic infection.

Increased resistance could result from frustrated penetration of antibiotics into the biofilm. In the case of positively charged aminoglycosides, absorption to negatively charged biofilm components may reduce drug effectiveness.[16,17] Frustrated diffusion of aminoglycosides may be a short term problem because eventually all binding sites would be occupied and lead to a restoration of diffusion. As a contrasting view, some authors have argued that slowed

diffusion may accentuate an enzymatic inactivation of the antibiotics.[12,13]

While the 3-dimensional biofilm structure and potential reduction in diffusion are factors in antibiotic resistance they do not explain why even after eventual saturation of the biofilm with antibiotics there is ineffective eradication of bacterial cells. Multiple researchers have revealed a significant nutrient and oxygen gradient across the biofilm.[18,19] Oxygen levels and protein synthesis are directly linked to metabolic activity in the bacterial cells with only metabolically active cells having normal antibiotic suceptiability.[20,21] Near the biofilm surface bacteria remain in an aerobic metabolic state and are readily killed with chemotherapy. In contrast, bacteria in the interior transition to an anaerobic metabolic state with far less susceptibility to aminoglycoside antibiotics.[18,19]

Along with nutrient driven metabolic changes, biofilm structures, and frustrated antibiotic diffusion it is known that some subset of the population (~1%) will experience a phenotypic change resulting in tolerance to antibiotics. Called “persister” cells, these bacterial cells repopulate the colony following what would have been eradication events such as exposure to antibiotic treatment.[22] Treating biofilm infections becomes more complex over time. Long term infections, like those observed in chronic pulmonary infection in cystic fibrosis become more difficult to combat as the infection matures. There are genetic adaptations in chronic infection over several years that leads to a loss of virulence factors.[9] While virulence factors are important for initial invasion, it has been suggested that these factors are also ligands for the human immune system and the subsequent loss may yield a more robust bacterial population.[9] In addition, these mutations may represent a symbiotic step in preserving the host organism as well as a decreased need to injure the host to generate nutrients. The culmination of these genetic changes is a more diverse and healthy population.

5.1.3 Current treatments and patient compliance

State of the art care guidelines for P. aeruginosa infection includes inhaled Tobramycin (aminoglycoside) for 28 day cycles.[23] Tobramycin works via accumulation on the bacterial cell surface, prompting an energy dependent uptake into the cell. Subsequent binding of tobramycin to RNA prevents protein synthesis, resulting in cell death.[24] Treatment with tobramycin has shown success in early acute *P.aeruginosa* infection, but is ineffective in terms of total eradication of chronic infection. Additionally, the burden of taking multiple doses per day for 28 day cycles including the time to nebulize the drug and sanitize the equipment after every dose leads to decreased patient compliance. This is further exacerbated by additional time intensive tangential therapies including physical therapy and pharmaceutical treatments for inflammation of airways, mucolytics, digestion, diabetes, and liver disease. While these metrics are difficult to measure the compliance rates for some treatments is estimated to be as low as 16-20%.[25–28] pPEMA–tobramycin coacervates can be used to prolong delivery of tobramycin and could decrease the number of daily treatments thus easing the burdens that decrease patient compliance. Additionally, tobramycin coacervates could improve tobramycin effectiveness against Aeruginosa biofilms by maintaining a constant concentration of tobramycin and by sequestering metal ions, which have been linked to the biofilm structure and inflammation, in an exchange process with tobramycin.

5.1.4 Complex coacervates: formation and physiochemical properties

It is proposed that a complex coacervate of poly-anionic polyphosphate and poly-cationic tobramycin can be aerosolized and delivered to the lungs, resulting in sustained release of tobramycin. Coacervation was first identified by F.W. Tiebackx in 1911 as a liquid-liquid phase

separation in a colloidal system. [29–31] A coacervate is comprised of a dense "coacervate" phase and a dilute "equilibrium" phase. A theoretical explanation of coacervation began in 1957 by J.Overbeek and M. Voon, which described coacervation both electrostatically and through entropy. [32] Coacervation is driven by attractive forces between oppositely charged particles and an entropic driving force from delocalization of counter ions from cationic and anionic components to form a neutral "complex".[31] When both polyions are oppositely charged polymers the process has been coined complex coacervation. Several physiochemical conditions have been identified that effect coacervate formation including: polyelecrolyte strength, mixing ratio and charge balancing, salt concentration, polymer mobility and temperature.[31] It was predicted that strong polyelectrolytes may form precipitates rather than liquid coacervate, charge balancing leads to maximum coacervate yield, and salt will have a dissociating effect on complex formation at both high and low concentrations.[31] By mixing negatively charged pPEMA with positively charged tobramycin in an aqueous solution of 1 M NaCl, tobramycin coacervates can be formed and then aerosolized for deposition in the airways.

5.2 Experimental Section

5.2.1 Materials

Phosphorus(V) oxychloride, 2-hydroxyethyl methacrylate, triethylamine, and glycidyl methacrylate were purchased from Alfa Aesar (Ward Hill, MA). Methacrylic acid, 2,2'-azobis(2-methylpropionitrile), acrylamide, N,N'-methylene-bisacrylamide, and N,N,N',N'-tetramethylethylenediamine were purchased from Sigma Aldrich (St Louis, MO). Ammonium persulfate was purchased from Fischer Scientific (Pittsburgh, PA). Tobramycin (97%) was acquired from Acros Organics (New Jersey, USA).

5.2.2 Synthesis of MOEP monomer and polyPEMA-MA copolymers

2-(Methacryloyloxy)ethyl phosphate (MOEP) was synthesized as previously described.[33] Briefly, phosphorus oxychloride (33.9 g, 220 mmol) and hydroxylethyl-methacrylamide (HEMA) were mixed at a 0.7:1 molar ratio in dry toluene (480 mL) under argon. The reaction was stirred at 4° C and triethylamine (TEA) (77 mL) added in three increments over 10 m. The reaction was stirred at 21-23° C for 6 h under argon, then filtered to remove precipitated trimethylamine hydrochloride salt . The reaction was cooled to 4° C before the addition of deionized water (480 mL), then stirred under argon at 22° C for 12 h. The reaction was extracted twice with diethyl ether (100 mL) and the organic layers discarded. MOEP was extracted from the aqueous layer into tetrahydrofuran (THF) and diethyl ether (1:2, 12 X 225 mL), then dried over anhydrous sodium sulfate before evaporating the solvent. A pale yellow, oil product (MOEP) was produced with an approximate 60% yield. Monomer structure was verified through H1 and P31 NMR.

Poly(phosphoethyl-methacrylate-co-acrylic acid) (pPEMA-AA) was synthesized by free radical polymerization of MOEP (85 mol%), and methacrylic acid (15 mol%) in methanol (12.5 mL mg^{-1} MOEP). MOEP and methacrylic acid were degassed by bubbling with argon for 1 h, followed by addition of azo-bis-isobutyronitrile (AIBN, 4.5 mol%) at 55°C to initiate polymerization. The reaction was stirred for 15 h before precipitation with acetone, then dissolved in water (200 mL H_2O per 17 g pPEMA-AA). Afterward, methacrylate groups (MA) were grafted onto the methacrylic acid sidechains by adding glycidyl methacrylate to the aqueous solution in 9-fold molar excess relative to the carboxylate sidechains and stirred at 21-23° C for 12 h. The methacrylated pPEMA-AA (pPEMA-MA) was adjusted to pH 7.3 with NaOH and purified by tangential flow filtration using a Millipore Pellicon 3 cassette filter with an Ultracel 10 kD membrane. The polymer product was lyophilized, and stored at -20°C. To produce a fluorescently labeled pPEMA-MA, fluorescein o-acrylate was added during polymerization at a

molar ratio of 1 fluorescein to 100 MOEP.

The structure and composition of the monomer (MOEP) and polymers (pPEMA-MA) were verified by ^{1}H and ^{31}P NMR.[34] The pPEMA-MA polymer contained 65 mol% phosphate sidechains, 12 mol% HEMA, and 23 mol% MA sidechains. The molecular weight (Mw) and polydispersity index (PDI) of pPEMA-MA were determined by size exclusion chromatography (SEC) on an Agilent Infinity 1260 HPLC system with a PL-Aquagel-OH Mixed-M column (8 μm, 300x 7.5 mm) column. The column buffer was 0.1 M $NaNO_3$ / 0.01 M NaH_2PO_4, pH 8.0 with a flow rate of 1 mL m^{-1}. The average M_m and PDI, 46 kg mol^{-1} and 1.67, respectively, were estimated using sodium polymethacrylic acid standards.

MOEP; ^{1}H NMR (D2O, 400 MHz); 5.9 (s, 1H), 5.5 (s, 1H), 4.2 (m, 2H), 4.0 (m, 2H), 1.7 (s, 3H).

^{31}P NMR (D2O, 400 MHz), 0.213 (s).

pPEMA-MA; ^{1}H NMR (D2O, 400 MHz); 6.1 (s, 1H), 5.6 (s, 1H), 4.2 (m, 2H), 4.1 (m, 2H), 3.5 (m, 2H), 1.8 (t, 2H), 1.0 (s, 3H), 0.8 (s, 3H).

5.2.3 Determination of effects of salt and temperature on yield and form of pPEMA-MA and tobramycin complex coacervates

Complex coacervates were formed by dissolving pPEMA-MA and tobramycin in aqeous NaCl (0-1.5 M) at a 1:1 charge ratio,pH 7.4 and 5° to 40° C. Solutions comprised 25 mg mL^{-1} of both pPEMA-MA and tobramycin for a total concentration of ~50 mg mL^{-1}, Figure 5.1. Coacervate formation was assumed to be complete with the formation two liquid phases and when the dilute phase changed from cloudy to clear which indicated coalescence of coacervate droplets into a single, fluid coacervate phase, Figure 5.2. The mid-point of pPEMA-MA phosphate transition from mono- to dianionic has been previously estimated at pH 7.4 and the total charges on tobramycin have been estimated at ~2.8 at pH 7.5, which leads to a 1:1 charge

ratio with equal mass of polymer and tobramycin.[34,35] The effects of salt during coacervation on yield and form were determined by varying NaCl concentration from 0 to 1.5 M. The effect of temperature was determined using a MJ Research PTC-150 Mini Cycler to vary the temperature between 5° and 40° C. Single coacervate samples were used over a variety of temperatures but the order of temperature points was randomized. Yield was optically measured by photographing coacevates in PCR 250 µL tubes and comparing to a standard curve derived from photographs of PCR tubes with known volumes. After 24 h coacervates were classified as cloudy or clear or as a gel if there was no flow after tilting the tubes at 90 degrees for one min, Figure 5.3 D-F. Coacervates for subsequent experiments were formed in 1 M NaCl at ~22° C.

5.2.4 Determining tobramycin concentration in both dense and dilute phases

Tobramycin concentration in the coacervate was determined by measuring depletion of tobramycin from the dilute phase after coacervation was assumed to be complete. Tobramycin concentrations were measured colorimetrically using a Pyrogallol Red-Molybdate (PRM) assay for primary amines [36–38]. A PRM solution was prepared by mixing 0.4 mL of 1.2 mg/mL pyrogallol red in methanol, 9 mL of a solution of 55 mM succinic acid and 4 mM sodium benzoate, and 0.04 mL each of 12 mM disodium molybdate and 261 mM sodium oxalate. Tobramycin containing samples (40 µL) were added to 160 µL of the PRM solution in a clear 96 well plate. After 30 m at 22° C absorbance at 600 nm was measured in a Spectra Max M2 plate reader and compared to tobramycin standards.

5.2.5 Resuspension of coacervate emulsion and analysis of aerosolized mass and droplet size

Clear, fluid coacervates were hand shaken for 1 m to re-suspend the coacervate into a cloudy solution of micro-coacervate droplets. Droplet size was estimated by taking DIC images from emulsion droplets placed on microscope slides immediately following resuspension by vortex. Using Image J, DIC images were converted to 8-bit images then a common threshold was applied and particle size calculated using the Image J analyze particles function. The resuspended solution or coacervate emulsion was aerosolized using a Respironics nebulizer attached to an Inspiration Elite compressor. Mass of aerosolized coacervate was estimated by aerosolizing coacervate emulsion onto pre-weighed tissue paper for 2 m. Subsequently, the tissue paper was dried via evaporation at 22° C for 15 m. Dry tissue paper was weighed and the mass of aerosolized materials between coacervate, free tobramycin and saline was compared. Additionally, an aerosolized mist of tobramycin coacervate was collected onto round glass cover slips for between 4-5 s and immediately placed into 2 mL of 130 mM NaCl, 1.5 mM Mg^{2+} and 2.5 mM Ca^{2+} at pH 7.3. After 24 h concentration of aerosolized tobramycin was quantified using the colorimetric PRM assay. Finally, fluorescently labeled pPEMA-MA was used in tobramycin coacervate formation and aerosolized onto standard glass slides and fluorescently imaged. Rapid formation of salt crystals prevented estimation of aerosolized droplet size via fluorescent microscopy but coacervate thin film formation was verified by measuring integrated intensity of the image using Image J and compared to the integrated intensity of an aerosolized 1 M NaCl saline.

5.2.6 *In vitro* release kinetics of tobramycin from tobramycin phosphate coacervate

Polyphosphate-tobramycin coacervates were formed in 2 mL aliquots in glass vials to form a thin coacervate layer on the bottom of the vial. The thickness of the coacervate layer was calculated by using the known surface area of the glass vial and know coacervate volume yield. The coacervate layer from a single 2 mL aliquot was approximately 0.3 mm thick. After coacervate formation the dilute phase was replaced by new 2 mL aliquots to produce coacervate layers of 0.6 and 1.2 mm thickness. After coacervate formation the dilute phase was replaced by 150 mM NaCl or a solution containing biologically relevant metals, 1.5 mM Mg^{2+} and 2.5 mM Ca^{2+}, then replaced again every 24 h and measured for tobramycin concentration using the PRM colorimetric assay.

5.2.7 Assessing the effectiveness at polyphosphate-tobramycin coacervate against gram negative bacteria in cystic fibrosis sputum and CFU quantification

Cystic fibrosis sputum was collected from patients from the Adult Cystic Fibrosis Center at the University Hospital, Salt Lake City, Utah. The study was reviewed and approved by the University of Utah Investigational Review Board (IRB). Written, informed consent was obtained from patient volunteers prior to collecting samples and data. Patients who presented with chronic *P.aeruginosa* infection were selected for sputum collection. Efforts were made to simply the experiment by avoiding collection from patients who were infected with other bacteria such as burkholderia cepacia to simply the experiment. Sputum was pipetted in 200 µL alliquots and spread evenly onto the bottom of 24 transwell plate inserts. The insert was subsequently placed into a custom holder in a 100 mL specimen cup with 80 mL of 0.9% saline. 25 µg of tobramycin-

polyphosphate coacverate or free tobramycin was spread across the top of the sputum and colony forming units were counted at 24 h. For CFU quantification sputum was resuspended in saline and removed from the transwell membrane. In a 10-fold dilution series, five 10 µL droplets were placed on agar plates and grown for 24 h at 37° C, after which the CFUs were counted. Since sputum samples contain a diverse microbiome, quantification was carried out for any gram negative strain against which aminoglycosides are particularly effective.

5.2.8 Data processing and statistical analysis

Data is reported as mean +/- 1 standard deviation with an n of 3. Mean and standard deviation was calculated using Microsoft Excel. Difference between means was tested for statistical significance using a one way ANOVA using IBM SPSS Statistical Analysis 24 software with a P value < 0.05 considered significant.

5.3 Results

5.3.1 Salt concentration and temperature affect coacervate yield and form

Both NaCl concentration and temperature were explored for their effects on coacervate volume yield, transparency and phase state, either gel or coacervate. Coacervate yield was maximized at 0.9 M NaCl and decreased with either increasing or decreasing salt concentration, (Figure 5.4). Temperature did not have an effect on coacervate yield. At zero NaCl a dense gel was formed (Figure 5.3 D) and at 0.15 mM NaCl the coacervate remained cloudy (Figure 5.3 A) . Clear coacervates were formed with 0.3 M NaCl between 5° and 30° C and with 0.9-1.5 M NaCl between 5° and 35° C, Figure 5.3 B. Temperature above 35° C resulted in cloudy coacervates across all salt concentrations, 0.15 M to 1.5 M, Figure 5.4.

5.3.2 Salt concentration affects tobramycin concentration in the coacervate phase

NaCl concentration not only affects coacervate volume yield and form but also affected the amount of tobramycin in the dense coacervate phase. Tobramycin content was measured in the supernatant of pPEMA-MA and tobramycin coacervates across NaCl concentrations from 0 to 1.2 M, Figure 5.5. The concentration of total tobramycin in coacervate and dilute phases was 25 mg mL^{-1}. At zero NaCl the tobramycin was concentrated primarily in the gel phase, 24 mg mL^{-1}, and decreased gradually to 20 mg mL^{-1} as NaCl concentration was increased to 0.9 M. Increasing NaCl concentration above 1 M resulted in more tobramycin remaining in the supernatant and only 9 mg mL^{-1} tobramycin in the coacervate at 1.2 M NaCl.

5.3.3 Aerosolization of coacervate by traditional jet nebulization

The current clinical methods for pulmonary delivery tobramycin requires aerosolization, therefore, the same methods were employed for aerosolizing tobramycin-pPEMA-MA coacervates. Aerosolization was accomplished using a standard clinical jet nebulization system, Figure 5.6. Before aerosolization clear coacervates were shaken by hand to resuspend the coacervate into an emmulsion of micro-coacervate droplets, Figure 5.6, 5.3 C.

Commercial jet nebulizers produce an aerosolized mist of particles between 1-5 µm and coacervate droplets can be nebulized in a similar size range as individual droplets or as smaller droplets contained in a larger droplet of dilute phase solution, Figure5.2. To assess droplet size prior to nebulization pre-aerosolized droplets were pipetted onto a glass slide immediately after resuspension and imaged using DIC microscopy. Using image J particle analyzer the droplet diamaters were calculated to be between 1 and 4 µm with the majority of droplets between 1 and 2 µm, Figure 5.7 C.

To determine successful aerosolization of coacervate droplets, nebulized particles were lected on filter paper for 2 minutes and weighed to compare mass. Weight of aerosolized coacervate was 17.7 +/- 4 mg, free tobramycin 8.7 +/- 4 mg, and saline 7 +/- 2 mg, Figure 5.6. There was significantly ($P<0.05$) more coacervate by weight nebulized versus aerosolized free tobramycin or 1 M saline, thus illustrating that the weight of material nebulized was not a result of free tobramycin or salt but in fact successful aerosilization of coacervate material.

As an alternative method to verify successful coacervate aerosolization, fluorescently labeled pPEMA-MA was used to form tobramycin-pPEMA-MA coacervates and was subsequently aerosolized onto glass slides and imaged with fluorescent microscopy. Evaporation of water quickly left salt crystals on the slide which prevented un-obstructed visualization of the aerosolized coacervate film and determination of droplet size or film formation. However, the integrated intensity of the fluorescent images is directly correlated with the quantity of fluorescent signal from surface b coacervate. The normalized integrated intensity was 1.5 +/- 0.8 for surfaces with labeled coacervate and 0.18 +/- 0.04 for surfaces with only aerosolized saline, Figure 5.8.

5.3.4 *In vitro* release of tobramycin from coacervates

The release kinetics of tobramycin from tobramycin pPEMA-MA coacervates was determined in both 150 mM saline and a more biolocically relevant solution of 130 mM NaCl, 1.5 mM Mg^{2+} and 2.5 mM Ca^{2+}. While polyphosphate-tobramycin coacervates dissolved completely within 48 h in 150 mM NaCl, they were stabilized in the presence of Ca^{2+} and Mg^{2+} due to formation of metal-phosphate complexes, which prevent dissociation of the coacervate. There was a corresponding sustained release of tobramycin as it exchanged with metal ions for up to 10 days. Immediately after replacing the dilute phase with a 130 mM NaCl, 1.5 mM Mg^{2+}

and 2.5 mM Ca^{2+} solution, the coacervate spontaneously re-suspended into a partly cloudy solution which was immediatly centrifuged to re-settle the coacervate phase. The quantity of tobramycin released was related to the thickness of the coacervate film. The initial 24 h release of tobramycin was 0.81 +/- 0.07, 1.08 +/- 0.05, and 1.35 +/- 0.02 mg for coacervates thickness of 0.3, 0.6 and 1.2 mm respectively, Figure 5.9. Tobramycin release decreased gradually to close to zero release at day 12 regardless of coacervate thickness, Figure 5.9. After 12 days, cumulative tobramycin release was 2.3 +/- 0.16, 3.1 +/- 0.14, 3.9 +/- 0.21 mg for coacervates thickness of 0.3, 0.6 and 1.2 mm respectively.

5.3.5 Efficacy against bacteria in CF sputum

CFUs were counted before and after exposure of sputum to free tobramycin and tobramycin coacervate. After 24 h there was a reduction in CFUs from 570 CFU gram positive mL^{-1} sputum to 14 CFU gram positive mL^{-1} sputum with free tobramycin and 10 CFU gram positive mL^{-1} sputum with coacervate. At the same time point there was a corresponding drop in gram negative CFU's from 5 CFU mL^{-1} sputum to 4 CFU mL^{-1} with free tobramycin and 1 CFU mL^{-1} with tobramycin-coacervate. It is important to note that there was a significant reduction of CFU's in all samples including the control over a 48 h time course.

5.4 Discussion

5.4.1 Factors effecting the yield, form and tobramycin content of pPEMA-MA coacervates

Formation of clear coacervates is dependent on the type of polyions. Strong polyions trend toward precipitation while weak polyions form coacervates.[31] For example, coacervates have been formed by weak interactions between negatively charged carboxyl groups and

charged residues in proteins such as B-lactoglobulin, whey protein, and albumin.[39–45] On the other hand, precipitates, instead of coacervates, resulted from stronger interactions between sulfate or phosphate groups and proteins like albumin and whey protein.[46–49] Preliminary work by Stewart and Song have shown that pPEMA-MA will form precipitates with Ca^{2+} and clear coacervates with Mg^{2+} an ion shown to form a weaker complex with phosphates.(unpublished) In pPEMA-pAAm hydrogels strong phosphate-Ca^{2+} crosslinks resulted in increased toughness while phosphate-Mg^{2+} crosslinks had much lower modulus and negligible work to fracture. The weakness of the Mg^{2+} bonds may be due in part to a higher affinity to retain an inner sphere hydration shell, a feature that may also assist in forming hydrated coacervates.[34,50] Like Mg^{2+}, tobramycin forms weak crosslinks in pPEMA-MA pAAm hydrogels, as evidenced by lower modulus and lack of yield (Chapter 4), and as a weak polyion also was shown to form clear coacervates with pPEMA-MA.

Coacervates were formed with a 1:1 charge ratio between the charged phosphates on pPEMA-MA and primary amines on tobramycin. Maximizing coacervate yield has been linked to forming neutral complexes or complete charge balance, a result that has been verified with polyphosphate-tobrmaycin coacervates (unpublished).[31] Both high and low NaCl concentrations have a general dissociative effect on complex formation, which explains the drop off in coacervate volume yield at salt concentrations higher or lower than 0.9 M NaCl, Figure 5.4. Lower salt concentration may result in electrostatic repulsive forces between charged phosphates while very high salt concentration shields these charges and may result in a shortened debye length, thus a reduction in complex formation.[51] Alternatively, high salt may also reduce the entropic driving force through counter ion release for complex formation. Furthermore, while the lower salt coacervates have a reduced volume the state change from clear coacervate to gel may suggest a denser material that is a result of dense crosslinking and

gel formation. Tobramycin content was shown to be maximized at low salt and supports the argument that, at low NaCl concentrations, the coacervate volume decrease is a result of condensing into a gel versus formation of less coacervate. Raising the salt concentration of beyond 1M NaCl results in less tobramycin in the dense coacervate phase due to increase charge screening and a reduction of tobramycin-pPEMA-MA complex formation. It is also possible that the presence of coacervate, when a majority of tobramycin remains in the dilute phase, may be driven by a salting out of the polymer from the dilute solution.[52]

5.4.2 Coacervates can be aerosolized using traditional jet nebulization

The current method for pulmonary delivery of tobramycin is jet nebulization of a solution of dissolved or unbound tobramycin. These devices use negative pressure arising from high-velocity gas, which draws liquid from a reservoir up a narrow opening or venturi where is it aerosolized, called the Bernoulli effect.[53] The overall technology for jet nebulization has remained consistant since the 1940's although recent designs by Pari LC® have increased efficiency.[54,55] Efforts to directly aerosolize the dense caocervate phase using current nebulization techniques was unsuccessful due to the high viscosity and cohesive forces. To aid in nebulization coacervates were shaken by hand to re-suspend the dense coacervate phase into micro-droplets in the dilute phase, forming a tobramycin-pPEMA-MA coacervate emmulsion. These re-suspended micro coacervate droplets were imaged with DIC microscopy and had diameters between 1-4 μm with ~90% below 2 μm. These droplet sizes fall into the normal range for nebulized droplets (1-5 um) and it is expected that coacervate droplets are either directly aerosolized or aerosolized as contained in droplets of dilute phase solution.

Re-suspended pPEMA-MA and tobramycin coacervates were successfully nebulized for pulmonary delivery as determined by both gravimetric data and fluorescent imaging. The

significantly (P<0.05) higher weight (+9 mg) of aerosolized coacervate material over tobramycin and 1M NaCl illustrates that the material aerosolized is due to coacervate complexes and not due to the salt content alone or from aerosolization of released or unbound tobramycin. In addition to increased aerosolized mass from nebulized coacervates fluorescein labeled coacervates were also nebulized and collected onto a glass slide as a film composed of collected aerosolized coacervate droplets. It is evident from fluorescent images and integrated pixel intensity that aerosolized droplets are collecting on the slide surface and merging to form a coacervate film. The significantly higher (P<0.01) integrated intensity of images of surfaces with labeled coacervate show successful nebulization of tobramycin-pPEMA-MA coacervate.

5.4.3 Evidence for sustained release from polyphosphate-tobramycin coacervate films

In the presence of divalent metal ions, coacervates are stabilized and have a sustained release profile with an initial bolus release followed by a slower release for up to 12 days. Initial replacement of the dilute phase with 150 mM NaCl and no divalent metal ions results in disruption of the equilibrium between dense and dilute phases and leads to dissolving of the coacervate within 48 h. However, in the presence of Ca^{2+} and Mg^{2+}, the dense coacervate phase is stabilized as tobramycin is released and replaced with metal-phosphate bonds. This was evident in pPEMA-pAAm hydrogels where metal ions such as Mg2+, Ca2+, and Zn2+ were shown to crosslink phosphates in the hydrogel. Similarly, metal ions can crosslink phosphates in the coacervate with a subsequent transition from fluid coacervate to crosslinked gel. The metal crosslinked coacervate or gel does not dissolve and leads to a sustained tobramycin release. The bolus release in the initial 24 h could be a result mixing that occurs during the first replacement of the dilute phase with the release solution. Divalent metal ions appear to initially

cause dispersion of the coacervate, increasing the interface area between the coacervate and release solution. Subsequent solutions changes did not result in any observable dispersion of the coacervate or change to solution transparency and the related tobramycin release was much lower than day 1. The quantity of tobramycin released in the first 24 h correlates with coacervate thickness with 0.81 +/- 0.07, 1.08 +/- 0.05, and 1.35 +/- 0.02 mg tobramycin for coacervates thickness of 0.3, 0.6, and 1.2 mm, respectively. This is expected, especially with an initial mixing event, that the tobramycin bolus release should increase with increasing mass of coacervate.

After the first 24 h, daily release decreased steadily down to zero by day 12. The percentage of total tobramycin release is dependent upon coacervate thickness. There is a 6%, 10%, and 15% release of total payload for coacervates with 1.2, 0.6, and 0.3 mm thickness respectively, Figure 5.9. A similar pPEMA-MA and pAAm hydrogel showed sustained release of tobramycin over 70 days but only released ~5% of total loaded tobramycin.[34] Both hydrogel and coacervate retain tobramycin through electrostatic interactions between phosphates and primary amine groups on tobramycin. Additionally, in both cases the release is suspected to be a gradual result of electrostatically reduced diffusion in combination with replacement by Ca^{2+} or Mg^{2+}. It has been argued in Chapter 3 that release of tobramycin from pPEMA-pAAm hydrogels may occur primarily from the surface of the material with interior tobramycin experiencing an insurmountable electrostatic barrier to diffusion. This may explain the release profile from tobramycin coacervates. While the amount of tobramycin coacervate doubles from thickness of 0.3 to 0.6 and from 0.6 to 1.2 mm the total drug release only increases by ~ 35% with most of the difference resulting from the initial bolus release, Figure 5.9. Additionally, since all coacervate samples have the same surface area and transition from fluid coacervate to gel in the presence of Ca^{2+}, it is reasonable to suggest that tobramycin release between days 2 and 12

is primarily from the surface of the coacervate, while interior tobramycin experiences a steep, electrostatic barrier to diffusion. This would explain the disproportionate increase to release tobramycin with increasing coacervate thickness and aligns with observations from tobramycin loaded hydrogels.

5.4.4 Reduction of bacteria in CF sputum by exposure to polyphosphate-tobramycin coacervate

Quantification of colony forming units from CF sputum showed a reduction in gram positive CFUs from 570 to 14 CFU uL^{-1} sputum for free tobramycin and 10 CFU uL^{-1} sputum for tobramycin coacervates. There was also a reduction in gram negative bacteria from 50 CFU uL^{-1} sputum to 4 and 1 with unbound tobramycin and tobramycin-coacervate respectively. In both cases, the coacervate samples were marginally more effective than free tobramycin. However, it is important to note that the control sample also saw a reduction in CFUs from 570 CFU uL^{-1} sputum to 54. This suggests some external event or environmental factor, which prevented growth of the bacteria. There are several potential sources for this observation: one, decreasing CFU count may have resulted from the freezing or storage process of sputum samples; two, sputum samples were taken from a patient on a current cycle of tobramycin. Prior preliminary experiments with fresh sputum showed little to no reduction of bacterial CFU's in sputum samples in a similar experimental set up over a 24 h time point. This could mean that the current results have discounted the sustained release of tobramycin from the coacervates because the bacteria in the unbound tobramycin sample was not capable of growing once the antibiotic had diffused out of the system. These results warrant further experimentation with fresh sputum samples and use of more stringent patient selection criteria to select only patients at least a week or two removed from their last tobramycin cycle. Additionally, progress can be

made by using tobramycin-coacervate in chronic pulmonary infection rat models or CF animal models.

5.5 Conclusions

Spontaneous coacervation between negatively charged polyphosphate polymer and positively charged tobramycin results in a phase separation into two aqueous layers, where tobramycin and polyphosphate polymer is concentrated into a dense coacervate phase. This tobramycin rich dense phase can easily be re-suspended, by simple vortexing, into an emulsion of micro droplets that are then readily aerosolized using current, standard nebulization equipment. Characterization of the coacervation process including NaCl concentration and temperature has revealed optimal synthesis conditions and a corresponding *in vitro* release assay has illustrated the materials potential for sustained delivery to tobramycin. Furthermore, initial tests of coacervate against bacteria in CF sputum show that coacervate particles successfully penetrate and deliver bactericidal levels of tobramycin. While it is unclear yet if there is significant improvement over the current state of the art, in terms of total infection eradication, the *in vitro* release assays show a prolonged release action, which can lead to a reduction of dosing frequency and thereby improve clinical outcomes.

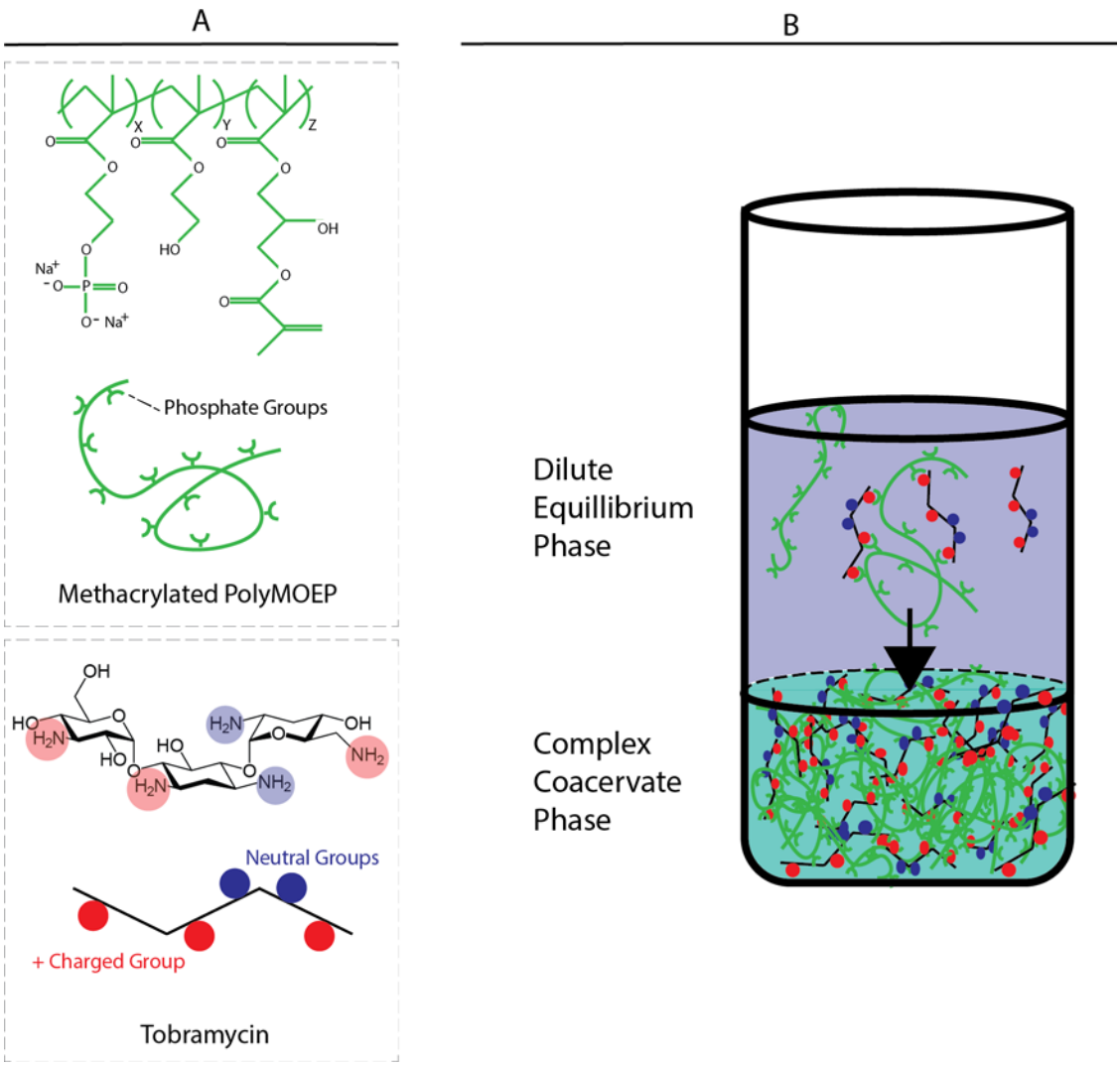

Figure 5.1: Schematic of tobramycin-polyphosphate coacervate formation. A) Starting materials consist of pPEMA-MA and tobramycin at initial concentrations of 50 mg mL^{-1} and pH 7.7. B) Combining both materials produces a liquid-liquid phase separation or coacervate. The dilute phase is shown in purple and the dense coacervate phase in blue.

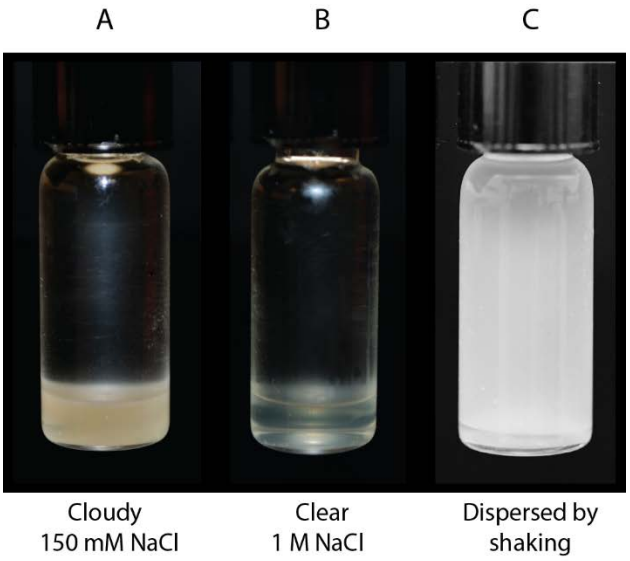

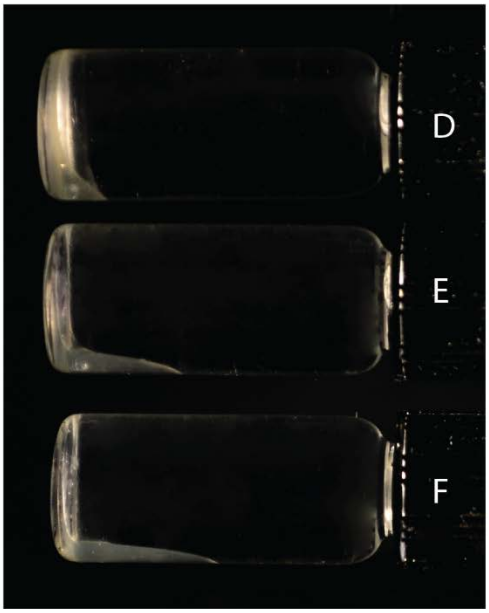

Figure 5.2: Photographs of coacervates to determine form and flow. NaCl concentration effects the transparency of coacervate: A) low salt (150 mM NaCl) resulted in cloudy coacervate, B) higher salt (1 M NaCl) results in a clear coacervate. C) Clear coacervates can be re-suspended into an emulsion of micro-coacervate droplets. D-F) The flow rate of coacervates is dependent on NaCl concentration: D) minimal flow in the gel-like coacervate with 150 mM NaCl, the flow rate increases with increasing NaCl concentration E) 500 mM NaCl and F) 1 M NaCl.

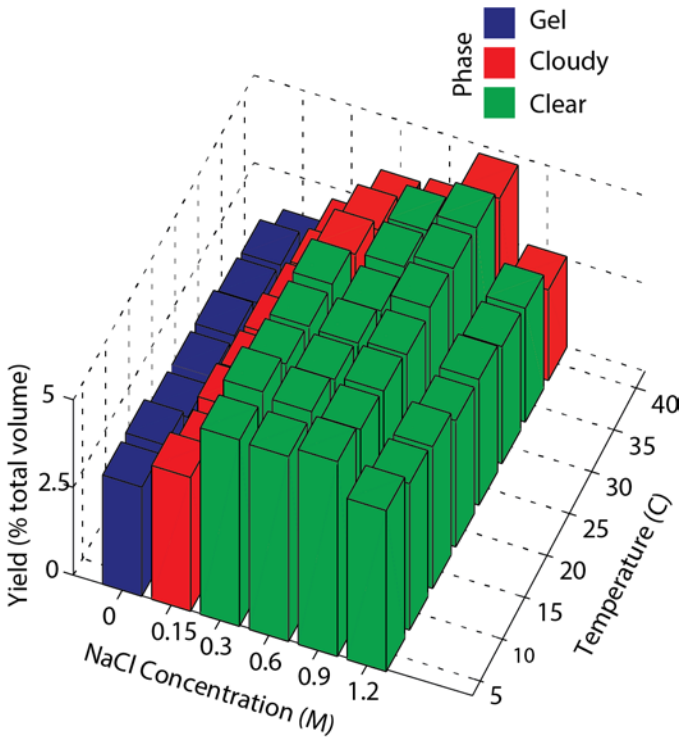

Figure 5.3: Four dimensional phase diagram for coacervate yield and form with varying salt concentration and temperature. Phase is gel (blue), cloudy (red) or clear (green). Total coacervate yield is presented as a percentage of total volume. Clear, fluid coacervates (area in green) are optimal for easy resuspension of the coacervate by simple shaking, followed by aerosolization.

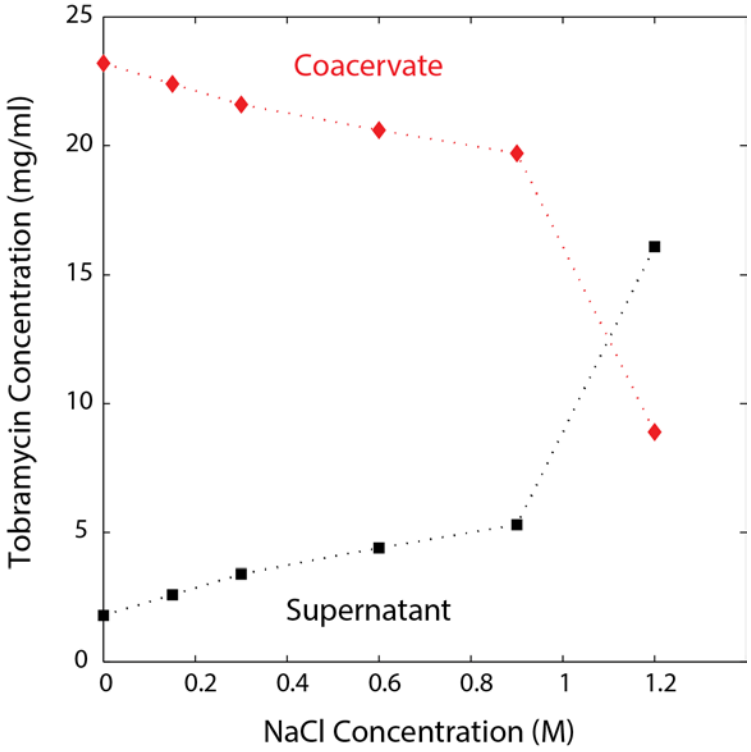

Figure 5.4: Effect of NaCl concentration on amount of tobramycin (mg/mL) in the dense coacervate phase (red) and dilute equilibrium phase (black). The crossover point between 1 M and 1.2 M NaCl indicates a noticeable drop off in coacervate yield.

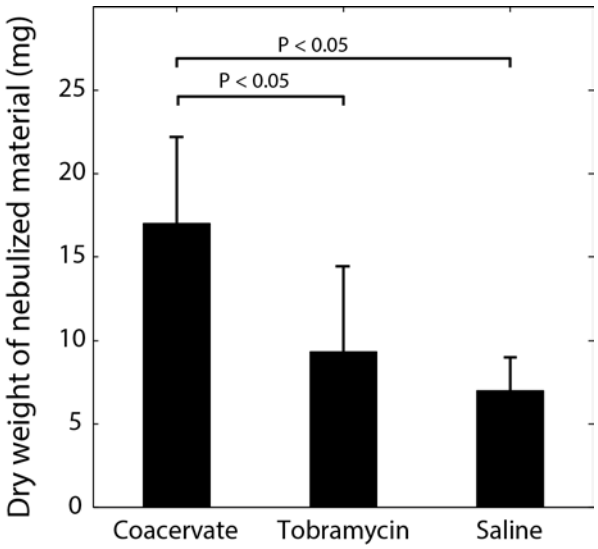

Figure 5.5: Gravimetric assessment of coacervate aerosolization. The weight of nebulized materials is significantly higher for coacervate sample versus free tobramycin and a 1 M NaCl saline. Error bars are +/- 1 S.D., n=3, and connecting bars and P values indicate statistical significance.

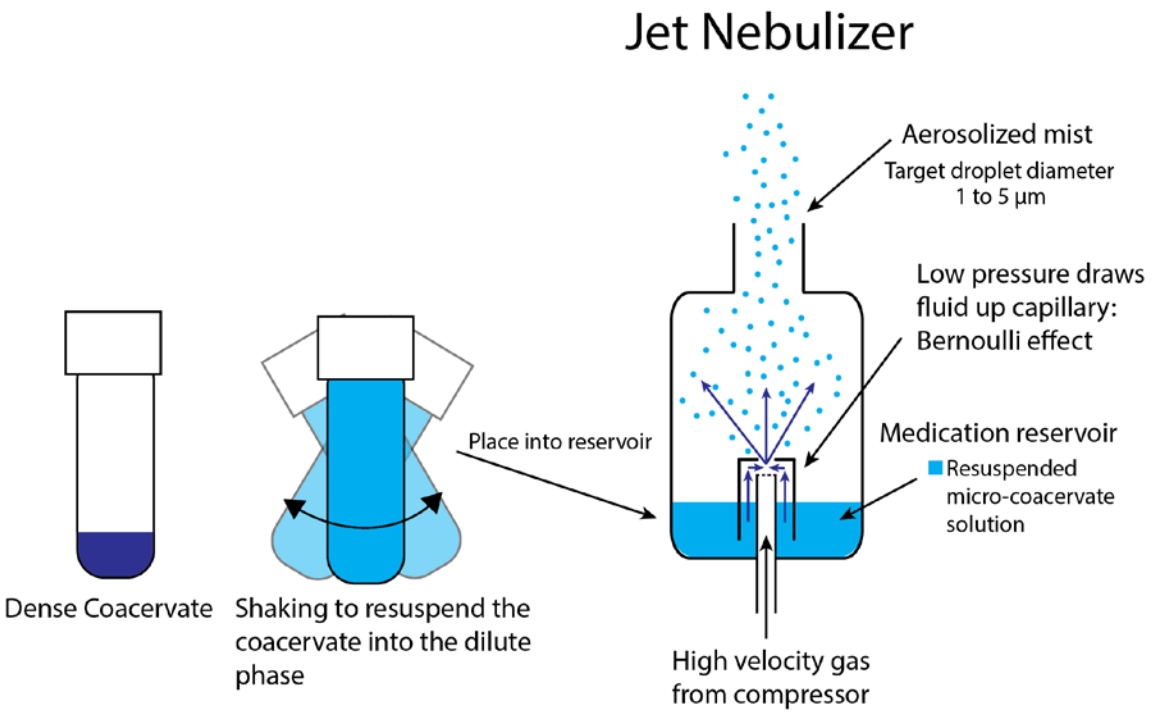

Figure 5.6: Schematic of coacervate resuspension and subsequent nebulization using a traditional jet nebulizer system. Dense coacervate is shown in dark blue and is easily resuspended into the dilute phase by shaking, shown in light blue. The coacervate suspension is placed into a nebulizer reservoir and aerosolized using high velocity gas jet and capillary. The resulting aerosolization should produce droplets between 1 and 5 µm diameter.

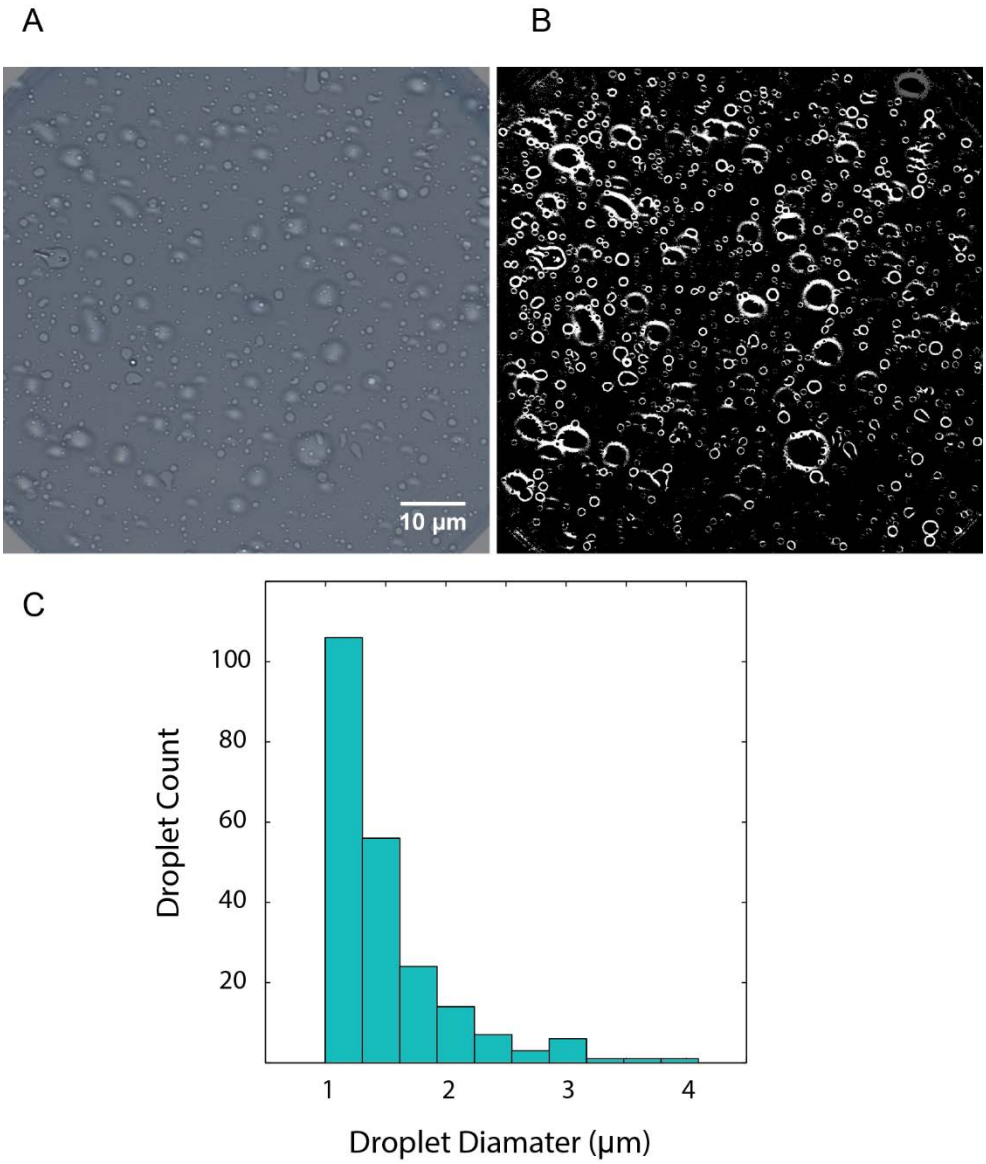

Figure 5.7: Coacervates can be resuspended into microdroplets with diameters less than 5 µm. A) DIC image of coacervate droplets within 1 minute of resuspension of coacervate droplets. B) DIC image after 8 bit conversion, thresholding and was used for particle size analysis. C) Histogram of droplet size from automated particle size analyzer function in Image J. Droplet diameter should be less than 5 µm for efficient aerosolization in the jet nebulizer system.

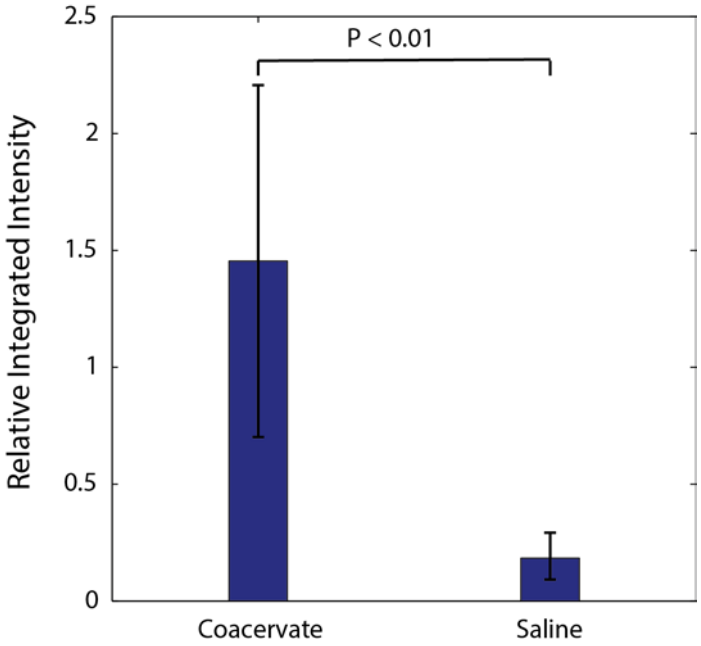

Figure 5.8: Fluorescently labeled pPEMA-MA tobramycin coacervates were aerosolized and collected on a glass slide. The integrated intensity of these images were compared between aerosolized coacervates and 1 M NaCl saline. The increased integrated intensity for the coacervate images indicated successful aerosolization of pPEMA-MA. Error bars are +/- 1 S.D., n=3, and connecting bar and P value indicate statistical significance.

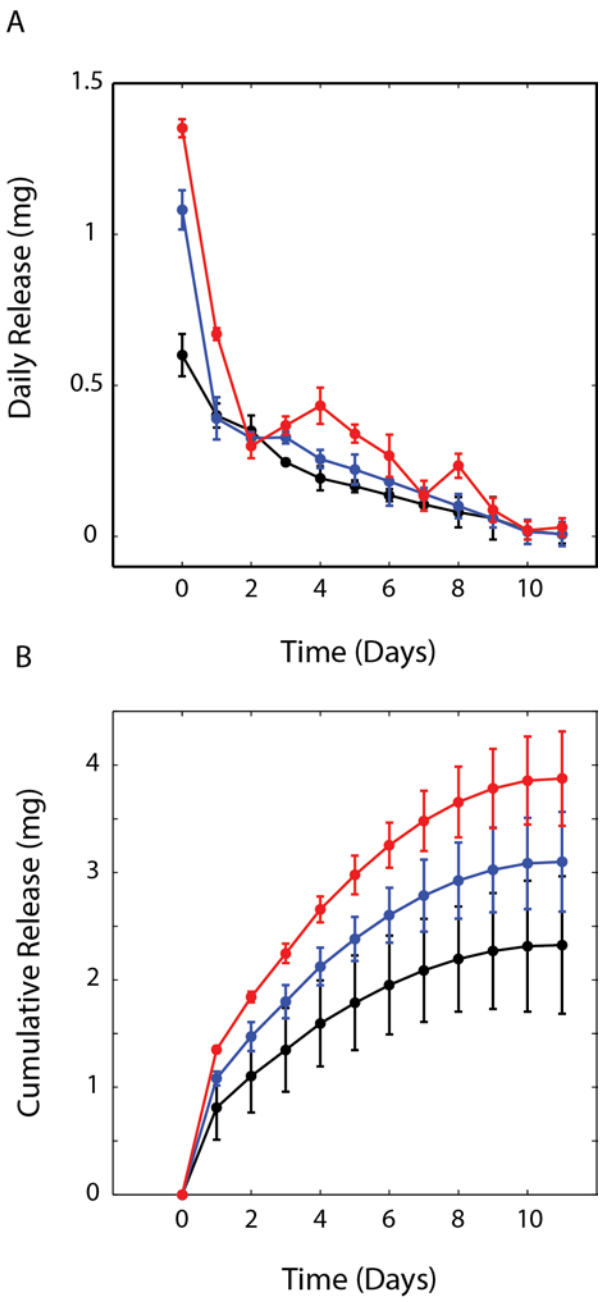

Figure 5.9: *In vitro* release of tobramycin from polyphosphate coacervates. A) Daily release of tobramycin from coacervate films of varying thickness, Red: 1.2 mm, Blue 0.6, and Black 0.3. B) Cumulative release of tobramycin summed from the daily tobramycin release data. Error bars are +/- 1 S.D. and n=3.

5.6 References

(1) Rosenstein, B. J.; Cutting, G. R. The Diagnosis of Cystic Fibrosis: A Consensus Statement. *J. Pediatr.* **1998**, *132* (4), 589–595 DOI: 10.1016/S0022-3476(98)70344-0.

(2) Cheng, S. H.; Gregory, R. J.; Marshall, J.; Paul, S.; Souza, D. W.; White, G. a; O'Riordan, C. R.; Smith, a E. Defective Intracellular Transport and Processing of CFTR Is the Molecular Basis of Most Cystic Fibrosis. *Cell* **1990**, *63* (4), 827–834 DOI: 10.1016/0092-8674(90)90148-8.

(3) Sheppard, D. N.; Ostedgaard, L. S. Understanding How Cystic Fibrosis Mutations Cause a Loss of Cl- Channel Function. *Mol.Med.Today.* **1996**, *2* (7), 290–297 DOI: 10.1016/1357-4310(96)10028-9.

(4) Quinton, P. M. Chloride Impermeability in Cystic Fibrosis. *Nature* **1983**, *301*, 421–422.

(5) Welsh, M. J.; Smith, a. E. Molecular Mechanisms of CFTR Chloride Channel Dysfunction in Cystic Fibrosis. *Cell* **1993**, *73* (7), 1251–1254 DOI: 10.1016/0092-8674(93)90353-R.

(6) FitzSimmons, S. C. The Changing Epidemiology of Cystic Fibrosis. *J. Pediatr.* **1993**, *122* (1), 1–9 DOI: 10.1128/CMR.00068-09.

(7) Singh, P. K.; Schaefer, a L.; Parsek, M. R.; Moninger, T. O.; Welsh, M. J.; Greenberg, E. P. Quorum-Sensing Signals Indicate That Cystic Fibrosis Lungs Are Infected with Bacterial Biofilms. *Nature* **2000**, *407* (6805), 762–764 DOI: 10.1038/35037627.

(8) Shah, V. S.; Meyerholz, D. K.; Tang, X. X.; Reznikov, L.; Alaiwa, M. A.; Ernst, S. E.; Karp, P. H.; Wohlford-lenane, C. L.; Heilmann, K. P.; Leidinger, M. R.; Allen, P. D.; Zabner, J.; Jr, P. B. M.; Ostedgaard, L. S.; Stoltz, D. A.; Randak, C. O.; Welsh, M. J. Airway Acidification Initiates Host Defense Abnormalities in Cystic Fibrosis Mice. *Science (80-.).* **2016**, *351* (6272), 503–507.

(9) Singh, P. K. Evolving Stealth: Genetic Adaptation of Pseudomonas Aeruginosa during Cystic Fibrosis Infections. *Proc. Natl. Acad. Sci. U. S. A.* **2009**, *103* (22), 1–5.

(10) Nguyen, D.; Emond, M. J.; Mayer-Hamblett, N.; Saiman, L.; Marshall, B. C.; Burns, J. L. Clinical Response to Azithromycin in Cystic Fibrosis Correlates with in Vitro Effects on Pseudomonas Aeruginosa Phenotypes. *Pediatr. Pulmonol.* **2007**, *42* (6), 533–541 DOI: 10.1002/ppul.20620.

(11) D'Argenio, D. a.; Wu, M.; Hoffman, L. R.; Kulasekara, H. D.; Déziel, E.; Smith, E. E.; Nguyen, H.; Ernst, R. K.; Larson Freeman, T. J.; Spencer, D. H.; Brittnacher, M.; Hayden, H. S.; Selgrade, S.; Klausen, M.; Goodlett, D. R.; Burns, J. L.; Ramsey, B. W.; Miller, S. I. Growth Phenotypes of Pseudomonas Aeruginosa lasR Mutants Adapted to the Airways of Cystic Fibrosis Patients. *Mol. Microbiol.* **2007**, *64* (2), 512–533 DOI: 10.1111/j.1365-2958.2007.05678.x.

(12) Stewart, P. S.; Costerton, J. W. Antibiotic Resistance of Bacteria in Biofilms. *Lancet* **2001**, *358*, 135–138.

(13) Stewart, P. S. Mechanisms of Antibiotic Resistance in Bacterial Biofilms. *Int. J. Med. Microbiol.* **2002**, *113*, 107–113.

(14) Drenkard, E. Antimicrobial Resistance of Pseudomonas Aeruginosa Biofilms. *Microbes Infect.* **2003**, *5*, 1213–1219 DOI: 10.1016/j.micinf.2003.08.009.

(15) Lawrence, J. R.; Korber, D. R.; Hoyle, B. D.; Costerton, J. W.; Caldwell, D. E. Optical Sectioning of Microbial Biofilms. *J. Bac* **1991**, *173* (20), 6558–6567.

(16) Dorrington, S. M.; Slack, M. P. E.; Walmsley, H. L. Inhibition of Tobramycin Diffusion by Binding to Alginate. *Antimicrob. Agents Chemother.* **1988**, *32* (4), 518–523.

(17) Whitchurch, C. B.; Tolker-nielsen, T.; Ragas, P. C.; Mattick, J. S. Extracellular DNA Required for Bacterial Biofilm Formation. *Science (80-.).* **2002**, *295* (22), 1487.

(18) III, M. C. W.; Roe, F.; Bugnicourt, A.; Franklin, M. J.; Stewart, P. S.; Iii, M. C. W.; Roe, F.; Bugnicourt, A.; Franklin, M. J.; Stewart, P. S. Contributions of Antibiotic Penetration , Oxygen Limitation , and Low Metabolic Activity to Tolerance of Pseudomonas Aeruginosa Biofilms to Ciprofloxacin and Tobramycin Contributions of Antibiotic Penetration , Oxygen Limitation , and Low Metabolic Activi. *Antimicrob. Agents Chemother.* **2003**, *47*, 317–323 DOI: 10.1128/AAC.47.1.317.

(19) Borriello, G.; Werner, E.; Roe, F.; Kim, A. M.; Ehrlich, G. D.; Stewart, P. S. Oxygen Limitation Contributes to Antibiotic Tolerance of Pseudomonas Aeruginosa in Biofilms Oxygen Limitation Contributes to Antibiotic Tolerance of Pseudomonas Aeruginosa in Biofilms. *Antimicrob. Agents Chemother.* **2004**, *48* (7), 2659–2664 DOI: 10.1128/AAC.48.7.2659.

(20) Allison, K. R.; Brynildsen, M. P.; Collins, J. J. Metabolite-Enabled Eradication of Bacterial Persisters by Aminoglycosides. *Nature* **2011**, *473* (7346), 216–220 DOI: 10.1038/nature10069.

(21) Gilbert, P.; Collier, P. J.; Brown, M. R. Influence of Growth Rate on Susceptibility to Antimicrobial Agents: Biofilms, Cell Cycle, Dormancy, and Stringent Response. *Antimicrob. Agents Chemother.* **1990**, *34* (10), 1865–1868 DOI: 10.1128/AAC.34.10.1865.

(22) Davies, D. G.; Parsek, M. R.; Pearson, J. P.; Iglewski, B. H.; Costerton, J. W.; Greenberg, E. P. The Involvement of Cell-to-Cell Signals in the Development of a Bacterial Biofilm. *Science (80-.).* **1998**, *280* (April), 295–298.

(23) Mogayzel, P. J.; Naureckas, E. T.; Robinson, K. a; Brady, C.; Guill, M.; Lahiri, T.; Lubsch, L.; Matsui, J.; Oermann, C. M.; Ratjen, F.; Rosenfeld, M.; Simon, R. H.; Hazle, L.; Sabadosa, K.; Marshall, B. C. Cystic Fibrosis Foundation Pulmonary Guideline. Pharmacologic Approaches to Prevention and Eradication of Initial Pseudomonas Aeruginosa Infection. *Ann. Am. Thorac. Soc.* **2014**, *11* (10), 1640–1650 DOI: 10.1513/AnnalsATS.201404-166OC.

(24) Taber, H. W.; Mueller, J. P.; Miller, P. F.; Arrow, a S. Bacterial Uptake of Aminoglycoside Antibiotics. *Microbiol. Rev.* **1987**, *51* (4), 439–457.

(25) Zindani, G. N.; H, M. P.; Streetman, D. D.; Pharm, D.; Streetman, D. S.; Pharm, D.; Nasr, S. Z.; D, M. Adherence to Treatment in Children and Adolescent Patients with Cystic Fibrosis. *J. Adolesc. Heal.* **2006**, *38*, 13–17 DOI: 10.1016/j.jadohealth.2004.09.013.

(26) Patricia, R.; Llorente, A.; Bousoño, C.; José, J.; Martín, D. Treatment Compliance in Children and Adults with Cystic Fibrosis. *J. Cyst. Fibros.* **2008**, *7*, 359–367 DOI: 10.1016/j.jcf.2008.01.003.

(27) Ziaian, T.; Sawyer, M. G.; Reynolds, K. E.; Carbone, J. A.; Clark, J. J.; Peter, A.; Couper, J. J.; Kennedy, D.; Martin, A. J.; Staugas, R. E.; French, D. J. Treatment Burden and Health-Related Quality of Life of Children with Diabetes , Cystic Fibrosis and Asthma. *J. Paediatr. Child Health* **2006**, *42*, 596–600 DOI: 10.1111/j.1440-1754.2006.00943.x.

(28) Sawicki, G. S.; Sellers, D. E.; Robinson, W. M. High Treatment Burden in Adults with Cystic Fibrosis : Challenges to Disease Self-Management. *J. Cyst. Fibros.* **2009**, *8* (2), 91–96 DOI: 10.1016/j.jcf.2008.09.007.

(29) Tiebackx, F. W. Gleichzeitige Ausflockung Zweier Kolloide. *Colloid Polym. Sci.* **1911**, *8* (4), 198–201.

(30) Bungenberg de Jong, H. G.; Kruyt, H. R. Coacervation (Partial Miscibility in Colloid Systems). *Proc K. Ned. Akad. Wet.* **1929**, *32*, 849–856.

(31) De Kruif, C. G.; Weinbreck, F.; De Vries, R. Complex Coacervation of Proteins and Anionic Polysaccharides. *Curr. Opin. Colloid Interface Sci.* **2004**, *9* (5), 340–349 DOI: 10.1016/j.cocis.2004.09.006.

(32) Overbeek, J. T. G.; Voorn, M. J. Phase Separation in Polyelectrolyte Solutions. Theory of Complex Coacervation. *J. Cell. Physiol.* **1957**, *49*, 7–26.

(33) Shao, H.; Weerasekare, G. M.; Stewart, R. J. Controlled Curing of Adhesive Complex Coacervates with Reversible Periodate Carbohydrate Complexes. *J. Biomed. Mater. Res. A* **2011**, *97* (1), 46–51 DOI: 10.1002/jbm.a.33026.

(34) Lane, D. D.; Fessler, A. K.; Goo, S.; Williams, D. L.; Stewart, R. J. Sustained Tobramycin Release from Polyphosphate Double Network Hydrogels. *Acta Biomater.* **2016**, *50*, 1–9 DOI: 10.1016/j.actbio.2016.12.030.

(35) Walter, F.; Vicens, Q.; Westhof, E. Aminoglycoside - RNA Interactions. *Curr. Opin. Chem. Biol.* **1999**, *3*, 694–704 DOI: 10.1016/S1367-5931(99)00028-9.

(36) Marshall, Thomas and Williams, K. Elimination of the Interference from Aminoglycoside Antibiotics in the Pyrogallol Red-Molybdate Protein Dye-Binding Assay,. *Clin. Chem.* **2004**, *50* (9), 1674–1675 DOI: 10.1373/clinchem.2004.033548.

(37) Yip, S. P.; Wong, M. L. Aminoglycoside Interference in the Pyrogallol Red-Molybdate Protein Assay Is Increased by the Addition of Sodium Dodecyl Sulfate to the Dye Reagent. *Clin. Chem.* **2003**, *49* (12), 2111–2112 DOI: 10.1373/clinchem.2003.023622.

(38) Bernard, S. An Improved Pyrogallol Red-Molybdate for Determining Total Urinary Protein. *Clin. Chem.* **1989**, *35* (11), 2233–2236.

(39) Burgess, D. J.; Kwok, K. K.; Megremis, P. T. Characterization of Albumin-Acacia Complex Coacervation. *J. Pharm. Pharmacol.* **1991**, *43* (4), 232–236 DOI: 10.1111/j.2042-7158.1991.tb06674.x.

(40) Girard, M.; Turgeon, S. L.; Paquin, P. Emulsifying Properties of Whey Protein-Carboxymethylcellulose Complexes. *Food Eng. Phys. Prop.* **2002**, *67* (1), 113–119 DOI: 10.1111/j.1365-2621.2002.tb11369.x.

(41) Kazmierski, M.; Wicker, L.; Corredig, M. Interactions of B-Lactoglobulin and High-Methoxyl Pectins in Acidified Systems. *J. Food Sci.* **2003**, *68* (5), 1673–1679 DOI: 10.1111/j.1365-2621.2003.tb12312.x.

(42) Laneuville, S.; Paquin, P.; Turgeon, S. Effect of Preparation Conditions on the Characteristics of Whey Protein—xanthan Gum Complexes. *Food Hydrocoll.* **2000**, *14* (4), 305–314 DOI: 10.1016/S0268-005X(00)00003-5.

(43) Weinbreck, F.; de Vries, R.; Schrooyen, P.; de Kruif, C. G. Complex Coacervation of Whey Proteins and Gum Arabic. *Biomacromolecules* **2003**, *4* (2), 293–303 DOI: 10.1021/bm025667n.

(44) Sanchez, C.; Mekhloufi, G.; Schmitt, C.; Renard, D.; Robert, P.; Lehr, C. M.; Lamprecht, A.; Hardy, J. Self-Assembly of β-Lactoglobulin and Acacia Gum in Aqueous Solvent: Structure and Phase-Ordering Kinetics. *Langmuir* **2002**, *18* (26), 10323–10333 DOI: 10.1021/la0262405.

(45) Schmitt, C.; Sanchez, C.; Thomas, F.; Hardy, J. Complex Coacervation between β-Lactoglobulin and Acacia Gum in Aqueous Medium. *Food Hydrocoll.* **1999**, *13* (6), 483–496 DOI: 10.1016/S0268-005X(99)00032-6.

(46) Weinbreck, F.; Nieuwenhuijse, H.; Robijn, G. W.; De Kruif, C. G. Complex Formation of Whey Proteins: Exocellular Polysaccharide EPS B40. *Langmuir* **2003**, *19* (22), 9404–9410 DOI: 10.1021/la0348214.

(47) Galazka, V. B.; Smith, D.; Ledward, D. A.; Dickinson, E. Complexes of Bovine Serum Albumin with Sulphated Polysaccharides: Effects of pH , Ionic Strength and High Pressure Treatment. *Food Chem.* **1999**, *64*, 303–310 DOI: 10.1016/S0308-8146(98)00104-6.

(48) Antonov, Y. A.; Gonçalves, M. P. Phase Separation in Aqueous Gelatin–κ-Carrageenan Systems. *Food Hydrocoll.* **1999**, *13* (6), 517–524 DOI: 10.1016/S0268-005X(99)00037-5.

(49) Gurova, A. N.; Gurova, N. V.; Leontiev, A. L.; Tolstoguzov, V. B. Equilibrium and Non-Equilibrium Complexes between Bovine Serum Albumin and Dextran sulfate—I. Complexing Conditions and Composition of Non-Equilibrium Complexes. *Food Hydrocoll.* **1988**, *2* (4), 267–283.

(50) Lane, D. D.; Kaur, S.; Weerasakare, G. M.; Stewart, R. J. Toughened Hydrogels Inspired by

Aquatic Caddisworm Silk. *Soft Matter* **2015**, *11*, 6981–6990 DOI: 10.1039/C5SM01297J.

(51) Seyrek, E.; Dubin, P. L.; Tribet, C.; Gamble, E. A. Ionic Strength Dependence of Protein-Polyelectrolyte Interactions. *Biomacromolecules* **2003**, *4* (2), 273–282 DOI: 10.1021/bm025664a.

(52) Grover, P. K.; Ryall, R. L. Critical Appraisal of Salting-out and Its Implications for Chemical and Biological Sciences. *Chem. Rev.* **2005**, *105* (1), 1–10 DOI: 10.1021/cr030454p.

(53) Watts, A. B.; McConville, J. T.; Williams, R. O. Current Therapies and Technological Advances in Aqueous Aerosol Drug Delivery. *Drug Dev. Ind. Pharm.* **2008**, *34* (9), 913–922 DOI: 10.1080/03639040802144211.

(54) Byrne, N. M.; Keavey, P. M.; Perry, J. D.; Gould, F. K.; Spencer, D. a. Comparison of Lung Deposition of Colomycin Using the HaloLite and the Pari LC Plus Nebulisers in Patients with Cystic Fibrosis. *Arch. Dis. Child.* **2003**, *88* (8), 715–718 DOI: 10.1136/adc.88.8.715.

(55) De Boer, A. H.; Hagedoorn, P.; Frijlink, H. W. The Choice of a Compressor for the Aerosolisation of Tobramycin (TOBI?? With the PARI LC PLUS?? Reusable Nebuliser. *Int. J. Pharm.* **2003**, *268* (1–2), 59–69 DOI: 10.1016/j.ijpharm.2003.09.004.

CHAPTER 6

CONCLUSION

6.1 Study discussion

The mechanical characterizations of polyphosphate and metal ion hydrogels has re-affirmed the importance of phosphate-metal complexes as a natural toughening mechanism. Simple inclusion of this feature into a synthetic polyphosphate hydrogel, as discussed in this dissertation, resulted in a replication of caddisfly silk mechanics including increased modulus with a defined pseudo-yield point. The yielding behavior has been conclusively linked to the presence of phosphate-metal complexes as the yield height can be modulated based on metal ion identity or eliminated after removal of metal ions with EDTA treatment. The serial regions of phosphate- Ca^{2+} in caddisfly silk, as well as the polyphosphate hydrogels, rupture following a critical stress resulting in large strain hysteresis and energy dissipation. The reversible Ca^{2+}-phosphate complexes are reformed during recoil and can completely recover the mechanical potential within 90 m for tensile tests or 30 m for compression. Furthermore, the strength and toughness of caddisfly inspired hydrogels compares favorably with other synthetic double network hydrogel discussed in chapter 2. The initial modulus of Ca^{2+} loaded gels were within the upper range of other DN hydrogels and Zn^{2+} loaded gels exceeded the stiffness of other compared hydrogels. Moreover, the toughness of polyphosphate-metal hydrogels was much greater than other hydrogels which derive toughness from great extensibility and not increased

modulus and yield behavior. As a result, the caddisfly inspired hydrogels are more suitable as mechanical replacements for soft structural tissues, which do not operate under such extreme strains.

Replacement of Ca^{2+} with tobramycin aminoglycosides resulted in a hydrogel densely crosslinked with tobramycin. Tobramycin loaded hydrogels in an *in vitro* solution with biologically relevant levels of Ca^{2+} and Mg^{2+} will gradually release tobramycin for up to 70 days. This *in vitro* release assay was further verified by placing tobramycin loaded hydrogels on a daily lawn of fresh *P. aeruginosa* where there was a measurable ZOI for 25 days. In addition to sustained ZOI formation tobramycin loaded hydrogels were used to totally eradicate P.aerugionsa biofilms within 48 h in a biomimetic flow cell. While tobramycin incorporation into the polyphosphate hydrogel had an impactful effect on bacterial eradication, tobramycin crosslinks were much weaker than the previous phosphate-metal complexes and as a result there was a related loss in hydrogel toughness. Since the polyphosphate hydrogels exhibited an ability to eradicate *P.aeruginosa* biofilms by releasing only 5% of the total tobramycin payload it was conceivable that combining metal ions with lower amounts of loaded tobramycin could eradicate biofilms while maintaining hydrogel toughness.

It is important to note that this dissertation explores an uncharted area of hydrogel design by incorporating both phosphate-metal complexes in combination with phosphate-tobramycin crosslinks for a dual mechanism for toughening and sustained aminoglycoside release. It was shown that inclusion of tobramycin crosslinking into a polyphosphate-Ca^{2+} hydrogel maintained the sustained release profile for up to 60 days. While there was a reduction in modulus (~0.4 MPa) and strength at 80% compression (0.8 MPa), the mechanical properties were sufficient for inclusion of the hydrogel as a cartilage replacement material or in total joint replacement surgery as a structural component or spacer.

Finally, the dissertation has presented a complex coacervate of polyphosphate polymer and tobramycin for use as a pulmonary delivery vehicle for sustained tobramycin release to combat chronic CF infection. This work may present the most impactful future application for these materials due to a lack of any current clinical options for total eradication of P.aerugionsa infection in CF patients. Furthermore, current efforts to improve delivery of tobramycin have centered on improvements to nebulization equipment. For example, some drugs, such as Aztrozeonam, are used with newer vibrating mesh nebulizers which dramatically increase efficiency and decrease treatment time. However, these newer devices require more frequent dosing and therefore an increased risk of poor compliance. There is an opportunity for a new delivery product that increases efficiency and increases compliance, and the tobramycin-polyphosphate coacervates fit this role.

6.2 Future work

6.2.1 Development of an antibiotic releasing, underwater, pressure sensitive tape

The works presented here have explored applications for the phosphate-metal complex toughening mechanism but have ignored the silk's underwater adhesive properties. The caddisfly silk is comprised of not only a viscoelastic, energy dissipating core but also an adhesive outer layer that has been thoroughly explored by Ching-Shuen Wang and Russel Stewart et. al.[1,2] Caddisfly silk has a fuzzy, adhesive peripheral layer that is present along the silk fiber, even inside the silk gland. The adhesive layer of the caddisfly silk is remarkably stable and, unlike terrestrial butterfly, moth or silk worm silk, is not easily stripped with detergents. Adhesion is proposed to occur in two steps. First, initial adhesion occurs from interactions between the peripheral glycoprotein layer and the surface. These initial interactions could be polymer-polymer entanglement or

physical crosslinking with surface absorbed macromolecules. Negative carbohydrate components could also interact with the surface electrostatically. Sugar –OH groups might also participate in surficial hydrogen bonding. Second, peroxinectin in the peripheral layer crosslinks tyrosine residues in the peripheral with phenolic groups absorbed on a surface. Such a complex form of adhesion may not be necessary as pPEMA-pAAm hydrogels could incorporate a surface layer of very low crosslinked hydrogel to provide an adhesive interface. It may also be possible to explore polyphosphate hydrogel adhesion to calcium rich bone matrix. Over time phosphates in the hydrogels could complex with calcium phosphates like hydroxyapatite in bone, leading to a stable adhesion.[3]

6.2.2 Hydrogels with dual delivery of drugs and synergistic molecules may improve clinical outcomes

A general principle in eradication of difficult infections is that the application of multiple antibiotics is more successful than single antibiotic use. Future work can include design of polyphosphate hydrogels that sustain the release of tobramycin in combination with other antimicrobials to produce a synergistic effect. Synergistic effects can be determined by isolating the CFU reduction from each single antimicrobial component and comparing with total CFU reduction from the combination. If the CFU reduction of the combination is greater than the sum of the individual components it would be considered a synergistic effect versus only additive.[4]

6.2.3 Delivery of copper-tobramycin complex to promote ROS or reduce inflammation

Copper has been identified as a cofactor to enhance the effectiveness of tobramycin although there is some disagreement as to the specific action of a copper-tobramycin complex.

Kozlowski et. al. claimed copper has been shown to complex at several binding sites on tobramycin and can accentuate its antimicrobial properties by promoting formation of free radicals or reactive oxygen species (ROS).[6] On the other hand, J.K. Shute et. al. have reported the Cu-Tobramycin complex as acting as an anti-inflammatory and antioxidant by removing ROS.[7] Future work may perhaps incorporate polyphosphate propensity for binding metal ions into a delivery device for copper-tobramycin, which may help shed light into the role this complex as an antimicrobial or as an anti-inflammatory agent.

6.2.4 Delivery of metabolites in combination with tobramycin to eliminate persister cells

Nutritional gradients across the biofilm results in starvation driven antibiotic tolerance, where cells at the surface consume the majority of resources while underlying cells become inactive and less susceptible.[8] Providing nutrients and metabolites to the population has been shown to accentuate the effectiveness of aminoglycosides. This could stem from cells reverting back to an aerobic form of metabolism or from contributions to the energy dependent step of aminoglycoside uptake. Metabolites such as glucose, fructose, mannitol and pyruvate might be delivered by passive diffusion from hydrogels or coacervate particles in accompaniment with tobramycin. [9] This approach has shown promise but is accompanied by increased risk to patient health. By increasing active bacterial cells there is increased risk of sepsis. Polyphosphate hydrogels have the potential to locally deliver a short burst of metabolites in combination with long term aminoglycoside release, which can kill bacterial cells as they become active and thereby reduce potential adverse effects to patient health.

6.2.5 Delivery of multiple antibiotic agents

Anti-pseudomonas penicillin's, such as piperacillin and carbenicillin, are recommended in combination with aminoglycosides, both to increase success of eradication and to prevent formation of drug resistant populations.[10] Anwar et. al. showed a synergistic effect of attacking mucosal pseudomonas with a 2:1 piperacillin to tobramycin ratio.[11] In the polyphosphate system, non-charged penicillin may diffuse from coacervates or gels in under a week, similar to the vancomycin release in chapter 4, followed by a prolonged release of tobramycin. Release of both drugs can be quantified using HPLC at various time points to determine a dual antibiotic release profile from the polyphosphate hydrogel or coacervate.

In addition to multiple antibiotic release, DNase drugs can also be included in a polyphosphate delivery system to aid in cleavage of DNA, an important contributor to mucosal viscosity. DNase drugs are frequently used to facilitate greater mucous clearance as well as supporting particle adhesion and penetration.[12] Furthermore, negatively charged regions in DNA are suspected of ensnaring positively charged aminoglycoside molecules thus preventing bacterial uptake.[13] The combination of a DNase such as dornase alfa and tobramycin could be tested for synergistic effects and may possibly be a less time consuming vehicle for delivering tobramycin in conjunction with mucolytics leading to improved patient compliance.

6.2.6 Using hydrogels to increase oxygen availability and increase ROS

Formation of free radicals is a shared effect of many antibiotics and has been shown to contribute to a common pathway of microbial death.[14–16] In benchtop experiments, increased availability of oxygen at the surface of a bacterial population is sufficient to enhance antibiotic effectiveness.[17] This suggests that an increase in ROS has meaningful effects on eradication that could be tested with a combination of tobramycin and hydrogen peroxide. Hydrogen peroxide

could be loaded into polyphosphate hydrogels or coacervates at 1 mM, which has been shown to be high enough to induce cell death.[18] Free radical concentration could be quantified using hydroxyphenyl fluorescein dye following published methods.[16,19] In this case, future efforts would also need to monitor the effects of 1 mM hydrogen peroxide on polyphosphate polymer by looking for changes in NMR and ATR-FTIR spectras that can indicate changes in structure including loss of phosphate groups.

6.3 References

(1) Wang, C.-S.; Ashton, N. N.; Weiss, R. B.; Stewart, R. J. Peroxinectin Catalyzed Dityrosine Crosslinking in the Adhesive Underwater Silk of a Casemaker Caddisfly Larvae, Hysperophylax Occidentalis. *Insect Biochem. Mol. Biol.* **2014**, *54*, 69–79 DOI: 10.1016/j.ibmb.2014.08.009.

(2) Wang, C.; Pan, H.; Weerasekare, G. M.; Stewart, R. J.; Stewart, R. J. Peroxidase-Catalysed Interfacial Adhesion of Aquatic Caddisworm Silk. *Interface* **2015**, *12*, 1–11.

(3) Silverthorn, D. U. *Human Physiology An Integrated Approach*, 5th ed.; Espinoza, D., Ed.; Pearson Education: San Francisco, 2010.

(4) Tallarida, R. J. An Overview of Drug Combination Analysis with Isobolograms. *J. Pharmacol. Exp. Ther.* **2006**, *319* (1), 1–7 DOI: 10.1124/jpet.106.104117.parture.

(5) Singh, P. K.; Tack, B. F.; McCray, P. B.; Welsh, M. J. Synergistic and Additive Killing by Antimicrobial Factors Found in Human Airway Surface Liquid. *Am. J. Physiol. Lung Cell. Mol. Physiol.* **2000**, *279* (5), L799–L805.

(6) Karaczyn, A.; Kozl, H. Copper (II) Binding to Tobramycin : Potentiometric and Spectroscopic Studies. *Carbohydr. Res.* **1998**, *313*, 265–269.

(7) Gziut, M.; Macgregor, H. J.; Nevell, T. G.; Mason, T.; Laight, D.; Shute, J. K. Anti-Inflammatory Effects of Tobramycin and a Copper – Tobramycin Complex with Superoxide Dismutase-like Activity. **2013** DOI: 10.1111/bph.12018.

(8) Nguyen, D.; Joshi-Datar, A.; Lepine, F.; Bauerle, E.; Olakanmi, O.; Beer, K.; McKay, G.; Siehnel, R.; Schafhauser, J.; Wang, Y.; Britigan, B. E.; Singh, P. K. Active Starvation Responses Mediate Antibiotic Tolerance in Biofilms and Nutrient-Limited Bacteria. *Science*. 2011, pp 982–986.

(9) Allison, K. R.; Brynildsen, M. P.; Collins, J. J. Metabolite-Enabled Eradication of Bacterial Persisters by Aminoglycosides. *Nature* **2011**, *473* (7346), 216–220 DOI: 10.1038/nature10069.

(10) Burke, C. M. *Antibiotic Essentials*, 12th ed.; Jones and Bartlett Learning: New York, 2013.

(11) Anwar, H.; Costerton, J. W. Enhanced Activity of Combination of Tobramycin and Piperacillin for Eradication of Sessile Biofilm Cells of Pseudomonas Aeruginosa. *Antimicrob. Agents Chemother.* **1990**, *34* (9), 1666–1671 DOI: 10.1128/AAC.34.9.1666.

(12) Deacon, J.; Abdelghany, S. M.; Quinn, D. J.; Schmid, D.; Megaw, J.; Donnelly, R. F.; Jones, D. S.; Kissenpfennig, A.; Elborn, J. S.; Gilmore, B. F.; Taggart, C. C.; Scott, C. J. Antimicrobial Efficacy of Tobramycin Polymeric Nanoparticles for Pseudomonas Aeruginosa Infections in Cystic Fibrosis : Formulation , Characterisation and Functionalisation with Dornase Alfa (DNase). *J. Control. Release* **2015**, *198*, 55–61 DOI: 10.1016/j.jconrel.2014.11.022.

(13) Dorrington, S. M.; Slack, M. P. E.; Walmsley, H. L. Inhibition of Tobramycin Diffusion by Binding to Alginate. *Antimicrob. Agents Chemother.* **1988**, *32* (4), 518–523.

(14) Wang, X.; Zhao, X. Contribution of Oxidative Damage to Antimicrobial Lethality. *Antimicrob. Agents Chemother.* **2009**, *53* (4), 1395–1402 DOI: 10.1128/AAC.01087-08.

(15) Wright, G. D. On the Road to Bacterial Cell Death. *Cell* **2007**, *130* (5), 781–783 DOI: 10.1016/j.cell.2007.08.023.

(16) Kohanski, M. a.; Dwyer, D. J.; Hayete, B.; Lawrence, C. a.; Collins, J. J. A Common Mechanism of Cellular Death Induced by Bactericidal Antibiotics. *Cell* **2007**, *130* (5), 797–810 DOI: 10.1016/j.cell.2007.06.049.

(17) Grant, S. S.; Kaufmann, B. B.; Chand, N. S.; Haseley, N.; Hung, D. T. Eradication of Bacterial Persisters with Antibiotic-Generated Hydroxyl Radicals. *Proc. Natl. Acad. Sci.* **2012**, *109* (30), 12147–12152 DOI: 10.1073/pnas.1203735109.

(18) Chupka, W. A.; Jivery, W. T.; Introduction, I. Toxic DNA Damage by Hydrogen Peroxide through the Fenton Reaction in Vivo and in Vitro. *Science (80-.).* **1975**, *240* (4852), 640–642.

(19) Setsukinai, K. ichi; Urano, Y.; Kakinuma, K.; Majima, H. J.; Nagano, T. Development of Novel Fluorescence Probes That Can Reliably Detect Reactive Oxygen Species and Distinguish Specific Species. *J. Biol. Chem.* **2003**, *278* (5), 3170–3175 DOI: 10.1074/jbc.M209264200.